Kyushu Institute of Technology

Measurement of Thermophysical Properties of Coatings by The Bi-directional 3ω Method

Submitted to Department of Mechanical Engineering

In Partial Fulfilment of the Requirements

for the Degree of Doctor of Engineering

by

Yihang JIAO

Advisor: Tomohide YABUKI

February 2023

Abstract

Printing technology enables the fabrication of large-area flexible sensors and electronic circuits at low cost and low environmental impact. Coatings are often used as components of various devices such as sensors, electronic devices, and energy conversion devices, and their thermophysical properties are an important factor in determining device performance. In thermoelectric (TE) conversion, where heat is converted to electricity and vice versa, printing technology can improve device scalability and production costs. High-throughput determination of thermal conductivity, one of the components of figure of merit ZT, will accelerate the development of printed thermoelectric materials. The 3-omega method and the thermoreflectance method have been representative methods for measuring the thermal conductivity of flat thin films deposited by physical or chemical vapor deposition. However, these methods require thin-film heaters or transducers deposited on the sample surface, and this is a barrier to the measurement for coated films, which are difficult to form the thin film. In this study, we developed new methods to measure the thermophysical properties of coatings based on the bi-directional 3-omega method.

This paper consists of five chapters. In Chapter 1, various thermophysical property measurement methods are reviewed, and their characteristics are described, indicating the necessity of developing a new method for thermophysical property measurement for coatings. In Chapter 2, the principle of the 3-omega method is described first, and then the developed measurement system for the 3-omega measurement of thermophysical properties, including home-built high-speed differential amplifiers with a cutoff

frequency of over 1 MHz, AC current source and lock-in amplifier is explained. In Chapter 3, the bi-directional differential 3-omega method was developed to measure the thermal conductivity of a thin material sandwiched between a thin film heater deposited on a substrate and a liquid with known thermal properties. To validate the proposed method, the thermal boundary resistance due to a thin air layer formed on a superhydrophobic surface underwater was measured, and the effective thickness of the air layer was calculated from the measured value. The obtained thermal boundary resistance was 7.5×10^{-6} [$(K\cdot m^2)/W$], and its equivalent air layer thickness was 0.2 μm and was consistent with the surface topology observed using an atomic force microscope. The decrease in air layer thickness due to degassing of the water was also successfully observed. In Chapter 4, I developed the dual-heater bi-directional 3-omega method, which can measure the thermophysical properties of printed films by using two different line width heaters with different sensitivities to thermal conductivity and volumetric specific heat. First, the thermal conductivity and thermal effusivity of glycerin droplet and SU-8 resin film were measured, and the results were in good agreement with the literature values, demonstrating the validity of the developed method and measurement system. Finally, the thermal conductivity of printed composite thermoelectric films composed of Bi2Te3-based thermoelectric material particles and polyimide, were measured. This method is expected to be useful for high-throughput measurement of thermophysical properties of various printed materials, not only thermoelectric printed films. Chapter 5 describes the main results obtained in this study and the prospects for future work.

Table of Contents

List of Figures

Abbreviations and Symbols

I_0	Amplitude of the input current [A]
ω	Angular frequency [rad/s]
R	Electrical resistance [Ω] (chapter 2)
T	Temperature [°C]
R_0	Electric resistance of heater without heating [Ω]
β	Temperature coefficient of resistance [-]
L	Length of heater [m]
P	Amplitude of sinusoidal Joule heating [W]
α	Thermal diffusivity [m^2/s]
η	Transformation variable of Fourier transform
b	Half-with of heater line [m]
λ	Thermal penetration depth [m]
γ	Euler-Mascheroni constant
Z	Thermal impedance [K/W]
R_f	Thermal resistance of the film [K/W]
V	Voltage [V]
Ra	Arithmetical mean roughness [m]
Rc	Ten-point mean roughness [m]
Rz	Maximum peak [m]
k	Thermal conductivity [W/(m·K)]
K	Attenuation ratio [-]
f	Frequency [Hz]
Φ	Phase [°]
δ	Thickness [nm]
x	x-axis
y	y-axis
z	z-axis
ρc	Volumetric heat capacity [$J/(K \cdot m^3)$]
E	Thermal effusivity [$J/(K \cdot m^2 \cdot s^{0.5})$]

Subscript

s	Substrate
samp.	Sample
air	Air
al	Air layer
b	Thermal boundary resistance
c	Coating
dry	Dry
eq	Equivalent
f	Film
h	Heating
i	Insulation layer (chapter 3)
w	Water
wet	Wetting
1-*sided*	One-sided
1ω	1ω component
2-*sided*	Two-sided
3ω	3ω component
↓	Bottom side
↑	Upper side
Gly.	Glycerin

Chapter 1

1. Introduction

1.1 Thermophysical properties in coated film applications

With the development of the industry, modern technology requires coated films for different applications [1-5]. And the thermophysical properties of various coatings have attracted more attention due to the demands for thermal management in the rapidly expanding microelectronic industries and the rise of thermoelectric technology [6, 7].

For instance, in microelectronic devices [8-15], a large heat generation density of chips causing a significant temperature rise to restrict the capability and reliability of chips. Even with the cooling system and heat sink, heat dissipation efficiency strongly depends on the thermophysical properties of the components. To improve the heat dissipation of electronic components to the heat sink, the dielectric and protective layers must have high thermal conductivity. A thermal interfacial materials (TIMs) coating between the chip and heat sink is typically applied [16-19] to reduce the contact thermal resistance. Thermal conductivity is one of the most important physical properties of TIMs. The measurement of the thermal conductivity of coated films is important for MEMS gas [12-14] sensors that measure temperature and heat or use temperature and heat measurement as a measuring principle. Morisaki et al. [20] developed a MEMS heat flux sensor to measure the local temperature and heat flux in the minichannel during flow boiling, and the thermal conductivity of the coated film between two RTDs has to be a known value. For

thermoelectric devices (TE), the popularity of thermoelectric materials has led to the development of thermoelectric devices and ways to improve their performance. The thermal conductivity was used to calculate the figure of merit, ZT, which was used to estimate the performance of TE devices [21-29].

For the superhydrophobic (SHB) surface [30,31], in Cassie-Baxter (CB), an air layer (plastron) is trapped between the superhydrophobic surface and liquid [32, 33]. This air layer caused a large thermal boundary resistance [34, 35] between the liquid and wall surface, which improved condensation heat transfer [30, 36] and anti-freezing capability [30, 35, 37].

1.2 Thermophysical properties of non-smooth coated films

Now, coatings are widely used in industry development. Thermophysical properties of the coatings are necessary to understand and design the thermal performance of the devices consisting of coated films. Conventionally, the surface of the coated film is thin and smooth, and the contact thermal resistance between the hot and cold surfaces is small. The existing thermophysical properties measurement methods are sufficient to measure (section 1.3). However, with the development of coated film diversification, such as printed thermoelectric devices, the surface of the coating is non-smooth (Fig. 1.1 (b)), or after coating the superhydrophobic films, the thermal boundary resistance caused by an air layer when the films immersed in water is large (Fig. 1.1 (a)), and the thermophysical properties of them have become a challenge to measure.

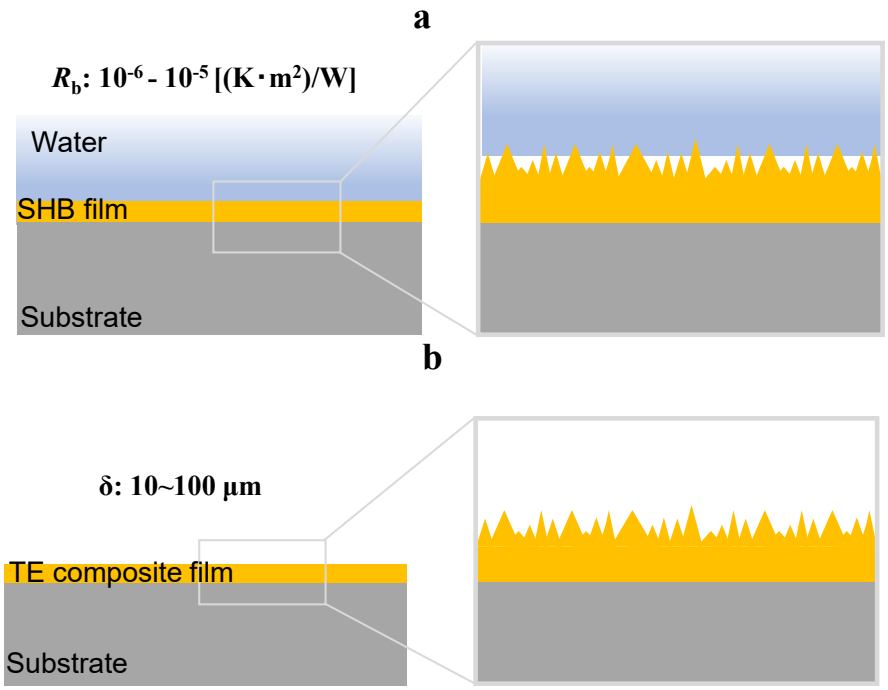

Fig. 1.1 The schematic diagram of (a) the air layer formed between the superhydrophobic surface and water, and (b) the rough coated TE composited films.

Fig. 1.2 is the SEM images of the surface of composite films of p-Bi_2Te_3 particles and polyimide made by Kato et al. We can see that the roughness of the surface is very large. Kato et al. measured the Seebeck coefficient and the thermal conductivity of the composite films, but the measured thermal conductivity using the differential 3-omega method is much smaller than the effective thermal conductivity. They considered that heat conduction can be suppressed due to strong phonon scattering at the interfaces between inorganic and organic materials [38]. For the superhydrophobic films, when immersed in the water, the trapped air layer between the liquid and the SHB surface will affect the wetting state and determine the performance of the SHB film [39], but it's difficult to measure the thickness of the trapped air layer directly. The thermal boundary resistance

due to the existence of air layers provides a viable way to determine the overall heat and mass transfer in phase-change phenomena on the superhydrophobic surface.

So, in this study, the first target is to measure the thermal boundary resistance (TBR) caused by the air layer between the superhydrophobic surface (SHB) and water. Our second target is to measure the thermal conductivity of the 10-100 μm thick printed TE composite film. Due to the large particle size, the film's surface is generally rough.

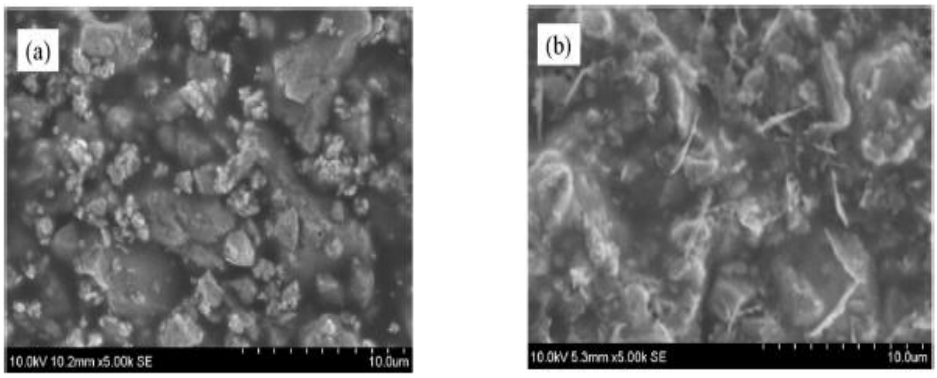

Fig. 1.2 SEM images of composite films of p-Bi_2Te_3 particles and polyimide [36].

1.3 Measurement methods of thermophysical properties for thin film

1.3.1 Steady-state methods

In the steady-state method, the heat flow through the sample and temperature is time-independent, so thermal conductivity can be determined using Fourier's law without considering heat capacity. This section will introduce the steady-state electrical heating method and the optothermal Raman method. The former is with a simple measurement principle, and the latter is the in situ and non-contact method that avoids the measurement error caused by the heat flow of contact in the traditional methods.

In 1989, Cahill et al. used the steady-state electrical heating method to determine the probability using a Monte Carlo calculation for a geometry representing the thermal conductivity sample [40]. Kurabayashi et al. used this method to measure the cross-plane thermal conductivity of the polymer film [41]. In both configurations, thin films with thickness d are grown or deposited onto a substrate with high thermal conductivity and slight surface roughness. A metallic strip with length L and width $2b$ ($L \gg 2b$) is then deposited onto the thin film whose thermal conductivity will be determined. The metallic strip should have a high-temperature coefficient of resistance (TCR), such as Cr/Au film. During the experiment, the metallic strip is heated by a direct current (DC) passing through it. The metallic strip serves as an electrical heater and a sensor to measure its temperature. The temperature of the metallic strip at the top/bottom surface of the thin film can be used to derive the thermal conductivity of the thin film according to Fourier's law.

A further extension of the above method is using a temperature sensor placed at a known distance away from the other heater to measure the temperature rise of the substrate right underneath it. Volklein et al. [42] and Asheghi et al. [43] employed this approach to measure the in-plane thermal conductivity of the thin film sample.

Another method is the optothermal Raman method [44], non-invasive measurements. For a suspended film, the increase in temperature can be obtained from either the redshift of the Raman G-band (2D-band) frequency or the anti-Stokes/Stokes ratio after heating by the laser, then calculate the thermal conductivity of the film. Hines et al. demonstrated the accuracy and precision (5% uncertainty) of particle-assisted Raman thermometry and electrical resistance thermometry using in-plane thermal conductivity measurements of anisotropic nanocrystalline diamond thin films[45]. Malekpour H et al. measured the

thermal conductivity of the 2D material, graphene using the Raman method [46].

The Raman method was also employed to measure the interfacial thermal resistance. Tang et al. used novel Raman-based dual thermal probing. They directly monitored the temperature drop across the 1.8 nm gap interface subjected to a laser-induced local heat flow. The thermal conductance for graphene/Si and graphene/SiO_2 interfaces is determined as 183 ± 10 and 266 ± 10 $W \cdot m^{-2} \cdot K^{-1}$ [47]. Yuan et al. investigated the interfacial thermal conductance between few to tens-layered mechanical exfoliated molybdenum disulfide (MoS_2) and crystalline silicon (c-Si) based on Raman spectroscopy and the thermal conductance in the range of 53-77 $MW \cdot m^{-2} \cdot K^{-1}$ [48].

Although measurement of the thermal conductivity and interfacial thermal resistance has been achieved using the steady-state method, the methods currently focus on the thin film sample with a smooth surface or the interfacial surface between two materials. However, for our targets, the above methods do not apply. The electrical heating methods can't deposit a thin film metallic strip heater on the non-smooth top surface of the coatings (Fig. 1.1(b) and Fig 1.3 (b)) and are also not suitable for measuring the thermophysical properties of the sample with the liquid component (Fig. 1.1(a)). Due to the rough surface of the coatings (Fig. 1.1(b)), a great degree of the possible induced noise in the Raman spectra will lead to the failure of our measurement, and the thermal boundary resistance caused by an air layer with a certain thickness between the SHB surface and the water (Fig. 1.1(a)) is also not suitable for optothermal Raman method.

1.3.2 Transient methods

For transient measurement methods, the heat flow through the sample is time-dependent, and thermophysical properties can be determined from the heat transfer in

response to a temperature change. In this section, the time-domain thermoreflectance (TDTR), frequency-domain thermoreflectance (FDTR), and 3-omega methods will be shown.

The method of the property of a surface to reflect light that changes as its temperature changes is called thermoreflectance. The optical pump-probe method is used in time-domain thermoreflectance (TDTR). The pump beam heats the surface of a sample. The probe beam measures the time-resolved thermoreflectance of bulk materials, nanostructures, and thin films. Various thermal properties, such as cross-plane thermal conductivity, in-plane thermal conductivity, interface thermal conductance, and heat capacity, can be determined by fitting the measured data to a thermal transport model, with unknown thermal properties as the fitting parameters.

In 1999, Capinski et al. measured the lattice thermal conductivity k normal to the interfaces of $(GaAs)_n$ /$(AlAs)_n$ superlattices with n between 1 and 40 monolayers using TDTR in the temperature range of 100 to 375 K [49]. In 2010, Zhu et al. measured the thermal conductivity of the 110 and 518 nm thick SiO_2 thin film using TDTR [50], demonstrating that the higher modulation frequency will give a high sensitivity to the thinner film. In 2010, Mak et al. measured the interfacial thermal conductance of single and multilayer graphene samples prepared on fused SiO_2 substrates using TDTR [51].

Time-domain thermoreflectance (TDTR) is an efficient method for determining the thermal characteristics of bulk materials and thin films. However, mechanical stage flaws can cause measurement inaccuracies, and ultrafast pulsed lasers are costly.

In frequency-domain thermoreflectance, also called FDTR, which is a variation of TDTR, the thermoreflectance signals are measured by changing the modulation frequency of the pump beam instead of the delay time between the pump beam and the

probe beam. This is in contrast to TDTR, in which the delay time varies between the pump beam and the probe beam. Because FDTR does not require a moving stage or an ultrafast pulsed laser, it can characterize the various thermal properties of bulk materials and thin films. As a result, TDTR's drawbacks are circumvented.

In 2011, Malen et al. presented the fiber-aligned frequency domain thermoreflectance (FAFDTR) and measured the thermal conductivity of bulk SiO_2 and thin film perylene and SiO_2. Instead of pricey lasers, FAFDTR uses cheap diode lasers. These lasers may be directly modified by their drive current, removing the need for extra modulators and enabling pump-probe alignment via a simple fiber coupler. The common mode rejection approach is presented to preserve accuracy despite diode laser noise [52]. Schmidt et al. measured the thermal conductivity of different thicknesses of thin gold and aluminum on the silica substrate using the FDTR [53]. Epstein et al. measured the thermal interfacial resistance of pentacene thin films deposited on silicon substrate under different temperatures using TDTR [54].

The degree to which the measurement signal is sensitive to the characteristics of the thermal environment is affected, in both TDTR and FDTR, by the modulation frequency. This sensitivity can be increased or decreased. When making measurements with a TDTR, the modulation frequency needs to be precisely chosen in accordance with the purpose of the research in order to attain a high level of precision. When making measurements with an FDTR, however, this is not an issue.

The 3-omega method has been used for measuring the thermal conductivities of bulk material (i.e., solid or liquid) or thin layers. In order to employ the technique to measure the thermal conductivity of bulk materials, we need to heat the sample using a thin film metal heater periodically. The temperature oscillation with respect to Joule heating at an

angular frequency of 2ω can be derived from the third harmonic voltage of the heating line. Because their behavior is dependent on frequency, it is possible to compute the thermal conductivity and thermal diffusivity of the sample.

For the smooth thin film, the differential 3-omega method was utilized to determine the thermal conductivity from the measured thermal resistance of the thin films. Cahill et al. proposed the differential 3-omega method for thermal conductivity of the 0.2-1.5 μm thick α-Si: H films [55]. Miyazaki et al. used the differential 3-omega method measuring the thermal interfacial resistance between Bi_2Te_3 and PEDOT: PSS to understand the low effective thermal conductivity of the printed thermoelectric composite [56]. To further understand the method, Dames carried out a systematic and detailed analysis of this method, considering the influence of each parameter on the measurement results [57].

The following problems arise when the 3-omega method and the thermoreflectance method, the representative methods for measuring the thermophysical properties of thin films introduced above, are used to measure the thermophysical properties of the coated films with rough surfaces (Fig. 1.1 (b)) and the thermal boundary resistance caused by the superhydrophobic surface when immersed in water (Fig. 1.1 (a)). Both methods require a thin metal film to be formed on the surface, a thin film heater in the 3-omega method and a transducer in the thermoreflectance method. However, it is difficult to deposit a thin film on a rough surface, and in the 3-Omega method, nonuniform heating of the heater film leads to errors (Fig. 1.3(b)), and in the thermoreflectance method, diffuse reflections on the transducer film surface reduce the sensitivity (Figs. 1.3(a) and (b)). Therefore, a new measurement method is required for the thermophysical properties measurement of the coated films with rough surfaces.

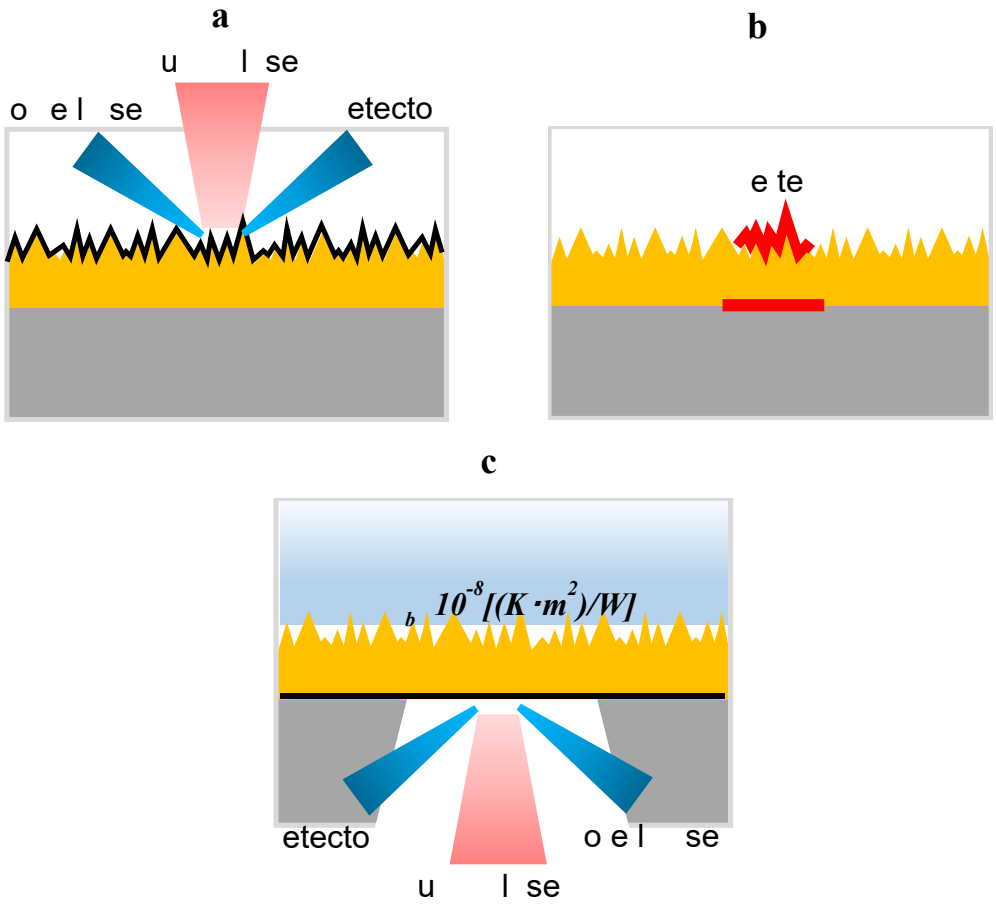

Fig. 1.3 The shortcomings of existing methods for thermophysical properties measurement. (a) the reflected light will be scattered on the non-smooth surface when using the thermoreflectance methods, (b) an even thin film metallic heater can't be deposited on the non-smooth surface, and uniform heating cannot be achieved, (c) the larger thermal boundary resistance caused by an air layer with a certain thickness is also not suitable to employ optothermal methods.

1.4 Bi-directional 3-omega method

To achieve our targets, the difficulty is that the surface of the coatings is non-smooth and the thermal boundary resistance caused by an air layer is large, and the above methods

can not achieve our targets. But, we found, as another extension of the 3-omega method, that the bi-directional 3-omega method has been utilized to measure the thermal conductivity of the samples above the heater. For example, Grosse et al. [58] measured the thermal conductivity of the small volume liquids, including pure water, glycerol, and 2-propanol, using the bi-directional 3-omega method. Lubner et al. [59] measured the thermal conductivity of the mouse liver at a temperature ranging from -69 ℃ to 33 ℃ for cryopreservation and cryosurgery. Park et al. [60, 61] made a nanoscale thermal sensor with a half-width of heater b = 200 nm to measure the thermal conductivity of a single biological cell to find the effect of disease progression on its thermal conductivity.

As we can see from the above examples, the bi-directional 3-omega method can be used to measure the thermal conductivity of liquids, biological cells, and biological tissues, and type, thickness, and the surface of the sample are no longer a problem as long as the measurement principle of this method is met. This supplies a direction for us to achieve our targets.

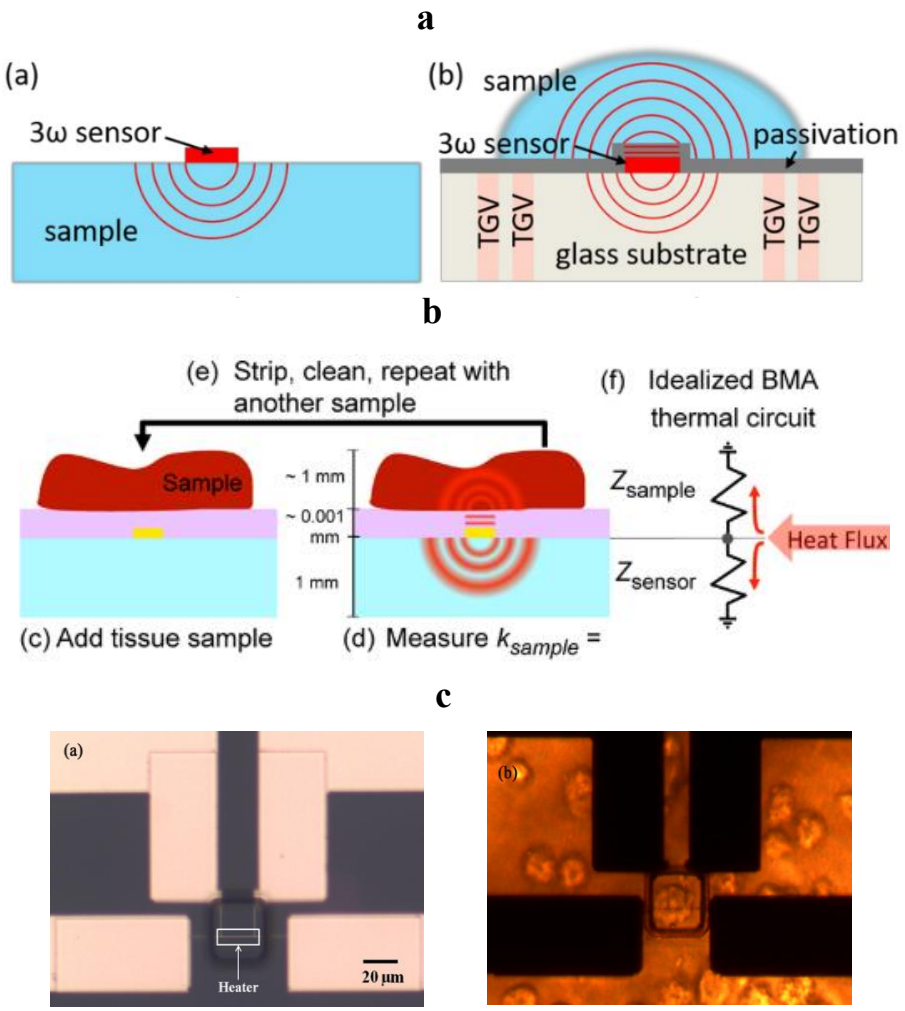

Fig. 1.4 The thermal conductivity measurement of the sample by the bidirectional 3-omega method: (a) the liquid sample [58], (b) the biological tissues [59], and (c) the single biological cell [60, 61].

1.5 Objective of the present study

The bi-directional 3-omega method can measure the thermal conductivity of a sample placed on the heater and thus can measure thermophysical properties independent of the roughness of the sample surface, as long as good thermal contact between the heater and the sample is ensured. The above advantage indicates the possibility of using the bi-

directional 3-omega method to measure the thermophysical properties of coated films with large roughness, as well as the large thermal resistance due to thin air layers between the superhydrophobic surface and water, which are our targets. Since previous studies have focused on relatively large samples, the objective of this study is to develop new methods based on the bi-directional 3-omega method that can measure the thermophysical properties of coated films.

In summary, in this study, we will further make innovative extensions to the bi-directional 3-omega method and use it to measure the thermal boundary resistance induced by the air layer between the SHB surface and water (Fig. 1. 5 (a)) and the thermal conductivity of the 10 - 100 μm thick coated film with non-smooth surfaces (Fig. 1. 5 (b)).

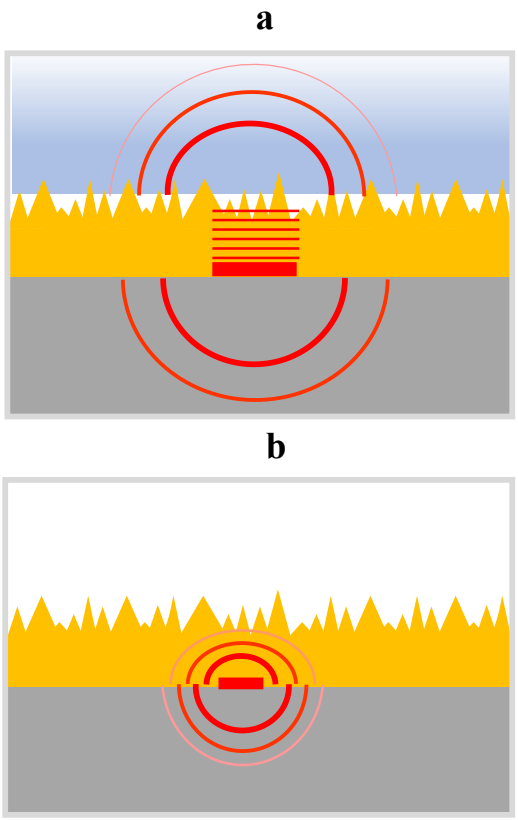

Fig. 1.5 Schematic of the objective of the present project using the bi-directional 3-omega

method: (a) the thermal boundary resistance caused by the air layer between the SHB surface and water, and (b) the thermal conductivity of the 10 - 100 μm thick coated films measurement.

1.6 Outline of this thesis

The thermophysical properties of the coatings are important for the thermal design of devices in industry development. The existing measurement techniques are basically sufficient for measuring the thermal properties of thin film samples, but they are not sufficient to achieve accurate measurements of the thermal conductivity of the coatings with rough surfaces and thermal boundary resistance caused by the superhydrophobic surface when immersed in water. In this study, based on the bi-directional 3-omega method, we will develop new methods to measure the thermophysical properties of the coatings.

In chapter 1, the background and literature survey of the research topic was done.

In chapter 2, the principle of the 3-omega methods containing the extensional methods was studied, and built a measurement system including the experimental circuit and LabVIEW program.

In chapter 3, the bi-directional differential 3-omega method was developed to measure the thermal boundary resistance induced by an air layer between the superhydrophobic surface and the water.

In chapter 4, the dual-heater bi-directional 3-omega method was developed to measure the thermophysical properties of the 10 - 100 μm thick printed films.

In chapter 5, a brief summary of the entire thesis was done.

References

[1] J.E. Greene, Review Article: Tracing the recorded history of thin-film sputter deposition: From the 1800s to 2017, J. Vac. Sci. Technol. A Vacuum, Surfaces, Film. 35 (2017).

[2] Mwema F M, Jen T C, Zhu L. Thin Film Coatings: Properties, Deposition, and Applications. CRC Press, 2022.

[3] A.D. Pogrebnjak, Advances in Thin Films, Nanostructured Materials, and Coatings, 2018.

[4] M.C. RAO, M.S. SHEKHAWAT, A Brief Survey on Basic Properties of Thin Films for Device Application, Int. J. Mod. Phys. Conf. Ser. 22 (2013) 576–582.

[5] Terry M. Tritt, Thermal Conductivity Theory: Theory, Properties, and Applications, 2013.

[6] J.C. Lambropoulos, S.S. Hwang, Thermal properties of thin films, Mater. Res. Soc. Symp. Proc. 284 (1993) 133–138.

[7] J. Epstein, W.L. Ong, C.J. Bettinger, J.A. Malen, Temperature Dependent Thermal Conductivity and Thermal Interface Resistance of Pentacene Thin Films with Varying Morphology, ACS Appl. Mater. Interfaces. 8 (2016) 19168–19174.

[8] D.G. Cahill, W.K. Ford, K.E. Goodson, G.D. Mahan, A. Majumdar, H.J. Maris, R. Merlin, S.R. Phillpot, Nanoscale thermal transport, J. Appl. Phys. 93 (2003) 793–818.

[9] D.G. Cahill, Thermal conductivity measurement from 30 to 750 K: The 3ω method, Rev. Sci. Instrum. 61 (1990) 802–808.

[10] D.G. Cahill, M. Katiyar, J.R. Abelson, Thermal conductivity of α-Si: H thin films,

Phys. Rev. B. 50 (1994) 6077–6082.

[11] Z.X. Zong, Z.J. Qiu, S.L. Zhang, R. Streiter, R. Liu, A generalized 3ω method for extraction of thermal conductivity in thin films, J. Appl. Phys. 109 (2011).

[12] van Zeijl H W. Thin film technologies for micro/nano systems; A review, ECS Transactions. (2014) 61(3): 191.

[13] Fine G F, Cavanagh L M, Afonja A, et al. Metal oxide semi-conductor gas sensors in environmental monitoring. sensors, (2010), 10(6): 5469-5502.

[14] Afridi M Y, Suehle J S, Zaghloul M E, et al. A monolithic CMOS microhotplate-based gas sensor system. IEEE Sensors Journal, (2002), 2(6): 644-655.

[15] S. Yamaguchi, T. Shiga, S. Ishioka, T. Saito, T. Kodama, J. Shiomi, Anisotropic thermal conductivity measurement of organic thin film with bidirectional 3ω method, Rev. Sci. Instrum. 92 (2021) 1–35.

[16] J.J. Park, M. Taya, Design of thermal interface material with high thermal conductivity and measurement apparatus, J. Electron. Packag. Trans. ASME. 128 (2006) 46–52.

[17] X. Xu, J. Chen, J. Zhou, B. Li, Thermal Conductivity of Polymers and Their Nanocomposites, Adv. Mater. 30 (2018) 1–10.

[18] Y. Zhou, S. Wu, Y. Long, P. Zhu, F. Wu, F. Liu, V. Murugadoss, W. Winchester, A. Nautiyal, Z. Wang, Z. Guo, Recent Advances in Thermal Interface Materials, ES Mater. Manuf. 7 (2020) 4–24.

[19] Q. Li, X. Tian, N. Wu, Y. Li, T. Pan, B. Zhang, Y. Duan, S. Wang, Y. Li, Enhanced thermal conductivity and isotropy of polymer composites by fabricating 3D network structure from carbon-based materials, J. Appl. Polym. Sci. 138 (2021) 1–11.

[20] Morisaki M, Minami S, Miyazaki K, et al. Direct local heat flux measurement during water flow boiling in a rectangular minichannel using a MEMS heat flux sensor. Experimental Thermal and Fluid Science, 2021, 121: 110285.

[21] G.J. Snyder, E.S. Toberer, Complex thermoelectric materials, Mater. Sustain. Energy A Collect. Peer-Reviewed Res. Rev. Artic. from Nat. Publ. Gr. 7 (2010) 101–110.

[22] J. Wei, L. Yang, Z. Ma, P. Song, M. Zhang, J. Ma, F. Yang, X. Wang, Review of current high-ZT thermoelectric materials, J. Mater. Sci. 55 (2020) 12642–12704.

[23] H. Mamur, M.R.A. Bhuiyan, F. Korkmaz, M. Nil, A review on bismuth telluride (Bi2Te3) nanostructure for thermoelectric applications, Renew. Sustain. Energy Rev. 82 (2018) 4159–4169.

[24] X.L. Shi, J. Zou, Z.G. Chen, Advanced thermoelectric design: From materials and structures to devices, Chem. Rev. 120 (2020) 7399–7515.

[25] S. Saini, A.K. Baranwal, T. Yabuki, S. Hayase, K. Miyazaki, Hybrid-Halide Perovskite Thin Film Growth for Thermoelectric Applications, J. Electron. Mater. (2020).

[26] P.A. Finn, C. Asker, K. Wan, E. Bilotti, O. Fenwick, C.B. Nielsen, Thermoelectric Materials: Current Status and Future Challenges, Front. Electron. Mater. 1 (2021) 1–13.

[27] P. Wu, Z. He, M. Yang, J. Xu, N. Li, Z. Wang, J. Li, T. Ma, X. Lu, H. Zhang, T. Zhang, A Review on Flexible Thermoelectric Technology: Material, Device, and Applications, 2021.

[28] K. Miyazaki, K. Kuriyama, T. Yabuki, Printable Thermoelectric Device, J. Phys. Conf. Ser. 1407 (2019).

[29] X. Chen, W. Dai, T. Wu, W. Luo, J. Yang, W. Jiang, L. Wang, Thin film thermoelectric materials: Classification, characterization, and potential for wearable applications, Coatings. 8 (2018).

[30] Zhang P, Lv F Y. A review of the recent advances in superhydrophobic surfaces and the emerging energy-related applications. Energy, 2015, 82: 1068-1087.

[31] P. Wagner, R. Fürstner, W. Barthlott, C. Neinhuis, Quantitative assessment to the structural basis of water repellency in natural and technical surfaces, J. Exp. Bot. 54 (2003) 1295–1303.

[32] Sheng X, Zhang J. Air layer on superhydrophobic surface underwater. Colloids and Surfaces A: Physicochemical and Engineering Aspects, 2011, 377(1-3): 374-378.

[33] Vakarelski I U, Chan D Y C, Marston J O, et al. Dynamic air layer on textured superhydrophobic surfaces. Langmuir, 2013, 29(35): 11074-11081.

[34] Moreira D I. Superhydrophobic Surfaces; Effects on Fluid, Thermal and Electrokinetic Transport. UC San Diego, 2016.

[35] Chavan S, Carpenter J, Nallapaneni M, et al. Bulk water freezing dynamics on superhydrophobic surfaces. Applied Physics Letters, 2017, 110(4): 041604.

[36] N. Miljkovic, R. Enright, Y. Nam, K. Lopez, N. Dou, J. Sack, E. N. Wang, Jumping-droplet-enhanced condensation on scalable superhydrophobic nanostructured surfaces, Nano letters 13(1) (2013) 179-187.

[37] L. Mishchenko, B. Hatton, V. Bahadur, J. A. Taylor, T. Krupenkin, J. Aizenberg, Design of ice-free nanostructured surfaces based on repulsion of impacting water droplets, ACS nano 4(12) (2010) 7699-7707.

[38] Kato K, Kuriyama K, Yabuki T, et al. Organic-inorganic thermoelectric material for a printed generator. Journal of Physics: Conference Series. IOP Publishing,

2018, 1052(1): 012008.

[39] Poetes R, Holtzmann K, Franze K, et al. Metastable underwater superhydrophobicity. Physical review letters, 2010, 105(16): 166104.

[40] Cahill D G, Fischer H E, Klitsner T, et al. Thermal conductivity of thin films: Measurements and understanding. Journal of Vacuum Science & Technology A: Vacuum, Surfaces, and Films, 1989, 7(3): 1259-1266.

[41] Kurabayashi K, Asheghi M, Touzelbaev M, et al. measurement of the thermal conductivity anisotropy in polyimide films. Journal of microelectromechanical systems, 1999, 8(2): 180-191.

[42] Völklein F. Thermal conductivity and diffusivity of a thin film SiO2/Si3N4 sandwich system. Thin Solid Films, 1990, 188(1): 27-33.

[43] Asheghi M, Kurabayashi K, Kasnavi R, et al. Thermal conduction in doped single-crystal silicon films. Journal of applied physics, 2002, 91(8): 5079-5088.

[44] Xian Y, Zhang P, Zhai S, et al. Experimental characterization methods for thermal contact resistance: A review. Applied Thermal Engineering, 2018, 130: 1530-1548.

[45] Hines N J, Yates L, Foley B M, et al. Steady-state methods for measuring in-plane thermal conductivity of thin films for heat spreading applications. Review of Scientific Instruments, 2021, 92(4): 044907.

[46] Malekpour H, Balandin A A. Raman-based technique for measuring thermal conductivity of graphene and related materials. Journal of Raman Spectroscopy, 2018, 49(1): 106-120.

[47] Tang X, Xu S, Zhang J, et al. Five orders of magnitude reduction in energy coupling across corrugated graphene/substrate interfaces. ACS applied materials & interfaces, 2014, 6(4): 2809-2818.

[48] Yuan P, Li C, Xu S, et al. Interfacial thermal conductance between few to tens of layered-MoS2 and c-Si: Effect of MoS2 thickness. Acta Materialia, (2017), 122: 152-165.

[49] Capinski W S, Maris H J, Ruf T, et al. Thermal-conductivity measurements of GaAs/AlAs superlattices using a picosecond optical pump-and-probe technique. Physical Review B, 1999, 59(12): 8105.

[50] Zhu J, Tang D, Wang W, et al. Ultrafast thermoreflectance techniques for measuring thermal conductivity and interface thermal conductance of thin films. Journal of Applied Physics, 2010, 108(9): 094315.

[51] Mak K F, Lui C H, Heinz T F. Measurement of the thermal conductance of the graphene/SiO 2 interface. Applied Physics Letters, 2010, 97(22): 221904.

[52] Malen J A, Baheti K, Tong T, et al. Optical measurement of thermal conductivity using fiber aligned frequency domain thermoreflectance. 2011.

[53] Schmidt A J, Collins K C, Minnich A J, et al. Thermal conductance and phonon transmissivity of metal–graphite interfaces. Journal of Applied Physics, 2010, 107(10): 104907.

[54] Epstein J, Ong W L, Bettinger C J, et al. Temperature dependent thermal conductivity and thermal interface resistance of pentacene thin films with varying morphology. ACS applied materials & interfaces, 2016, 8(29): 19168-19174.

[55] Cahill D G, Katiyar M, Abelson J R. Thermal conductivity of a-Si: H thin films. Physical review B, 1994, 50(9): 6077.

[56] Miyazaki K, Kuriyama K, Yabuki T. Printable Thermoelectric Device. Journal of Physics: Conference Series. IOP Publishing, 2019, 1407(1): 012057.

[57] Dames C. Measuring the thermal conductivity of thin films: 3 omega and related

electrothermal methods. Annual Review of Heat Transfer, 2013, 16.

[58] Grosse C, Ras M A, Varpula A, et al. Microfabricated sensor platform with through-glass vias for bidirectional 3-omega thermal characterization of solid and liquid samples. Sensors and Actuators A: Physical, 2018, 278: 33-42.

[59] Lubner S D, Choi J, Wehmeyer G, et al. Reusable bi-directional 3 ω sensor to measure thermal conductivity of 100-μ m thick biological tissues. Review of Scientific Instruments, 2015, 86(1): 014905.

[60] Kyoo Park B, Yi N, Park J, et al. Thermal conductivity of single biological cells and relation with cell viability[J]. Applied Physics Letters, 2013, 102(20): 203702.

[61] Park B K, Woo Y, Jeong D, et al. Thermal conductivity of biological cells at cellular level and correlation with disease state. Journal of Applied Physics, 2016, 119(22): 224701.

Chapter 2

2. Principle and measurement system of 3-omega method

2.1 Introduction

The 3-omega method has been widely used for measuring the thermal conductivity of a wide variety of materials, such as bulk materials [1, 2], thin films [3-9], liquid samples [10-14], and bio-samples [15-17]. Moreover, the 3-omega method was applied to measure the anisotropy of thermal conductivity and freestanding membranes [18-20]. Compared to the steady-state methods [21, 22] and optical pump-probe method (TDTR [23, 24] & FDTR [25]), the 3-omega method has the advantages listed as follows [7]:

1. The heat loss due to radiation and convection can be ignored, and it is easy to quantify the heat flux accurately. This results in high measurement accuracy.
2. The experimental setup is more straightforward than other methods, and the testing procedure is not complicated.
3. The temperature dependence of the electrical resistance of a strip heater is one or two orders of magnitude larger than the temperature dependence of the reflectance used in the thermoreflectance method, and the high accuracy of the temperature measurement leads to high accuracy in the resulting thermophysical property measurements.

2.2 Principle of 3-omega method

A thin film metal heating line was deposited on the substrate as the heater and resistance thermometer [1-3, 26]. A cosine AC was supplied to the heating line,

$$I = I_0 \cos(\omega t) \tag{2.1}$$

where I_0 is the amplitude of the input current, and ω is the angular frequency of the AC signal.

Joule heating rate P can be expressed as,

$$P(t) = I^2 R = \frac{1}{2} I_0^2 R\{1 + \cos(2\omega t)\} = P_{DC} + P_{2\omega} \cos(2\omega t) \tag{2.2}$$

where R is the resistance of the heater, from Eq. 2.2, the Joule heating power can be divided into the DC component and the AC component with an angular frequency of 2ω. AC Joule heating causes AC temperature change ΔT,

$$\Delta T(t) = \Delta T_{DC} + \Delta T_{2\omega} \cos(2\omega t) \tag{2.3}$$

where the $\Delta T_{2\omega}$ is the second harmonic temperature rise which is a function of the thermophysical properties of the samples, and this temperature fluctuation results in a change in the electrical resistance of the heater line.

$$R(t) = R_0(1 + \beta \Delta T) = R_0\{1 + \frac{1}{R_0}\frac{dR}{dT}(\Delta T_{DC} + \Delta T_{2\omega} \cos(2\omega t))\} \tag{2.4}$$

$$\beta = \frac{1}{R_0}\frac{dR}{dT} \tag{2.5}$$

where R_0 is the resistance of the heater without heating, and β is the temperature coefficient of resistance.

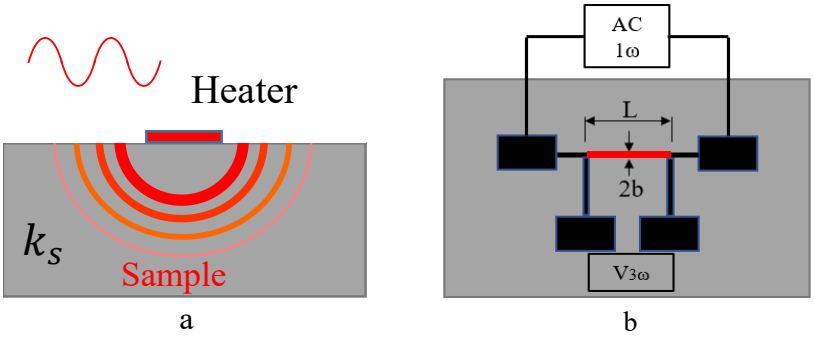

Fig. 2.1 The schematic of the 3-omega method.

According to Ohm's law, the voltage drop V(t) across the heating line can be obtained as follows.

$$V(t) = I_0 R_0 (1 + \frac{1}{R_0}\frac{dR}{dT}\Delta T_{DC})\cos(\omega t) + \frac{1}{2}\{I_0 R_0 \frac{1}{R_0}\frac{dR}{dT}\Delta T_{2\omega}\cos(\omega t)\} + \frac{1}{2}\{I_0 R_0 \frac{1}{R_0}\frac{dR}{dT}\Delta T_{2\omega}\cos(3\omega t)\} \quad (2.6)$$

The voltage drop contains the 1ω component (first and second terms) and 3ω component (third term). The temperature amplitude $\Delta T_{2\omega}$ to be measured contained the 1ω component and 3ω component, too. Since it is difficult to separate the 1ω component into ΔT_{DC} and $\Delta T_{2\omega}$, $\Delta T_{2\omega}$ is calculated from the amplitude of the 3ω component.

Next, the equation related to $\Delta T_{2\omega}$ and the $V_{3\omega}$ can be derived,

$$V_{3\omega} = \frac{1}{2} V_0 \beta \Delta T_{2\omega} \quad (2.7)$$

$$V_0 = I_0 R_0 \quad (2.8)$$

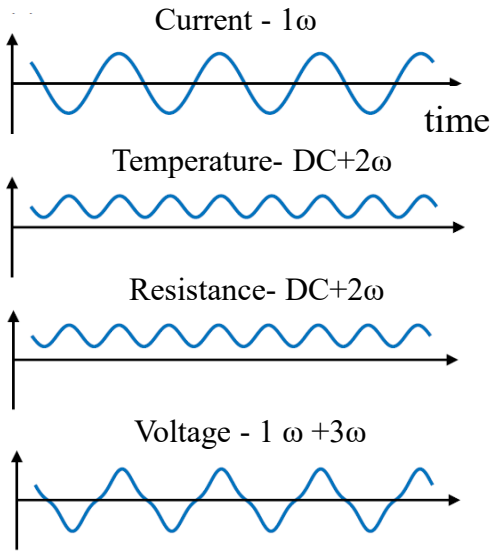

Fig. 2.2 The various resonance signal waveforms during the measurement.

To obtain an analytical solution for the average temperature of a thin wire heater with a width of 2*b*, we first obtain an analytical solution for the temperature response of an AC-heated wire heat source. Figure 2.3 is a cylindrical coordinate system with a linear heat source at the center. Since the length of the heat source is sufficiently long and the temperature distribution in the longitudinal direction is negligible, only radial heat conduction is considered. The radius *r* is the distance of the temperature oscillation away from the infinitely narrow heating line.

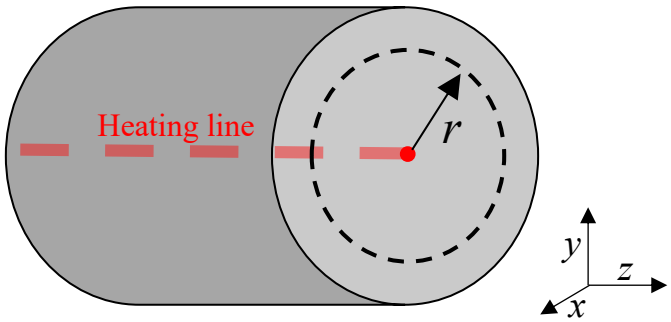

Fig. 2.3 One-dimensional heating line inside the cylinder sample.

The one-dimensional transient heat conduction equation to be solved is

$$\frac{\partial^2 T(r,t)}{\partial r^2}+\frac{1}{r}\frac{\partial T(r,t)}{\partial r}-\frac{1}{\alpha}\frac{\partial T(r,t)}{\partial t}=0 \tag{2.9}$$

The line heat source is AC heated, and the temperature oscillation $T(r, t)$ inside the sample is dependent both on the distance from the heating line and time and can be separated into time and spatially dependent parts [27],

$$T(r,t)=T_r \exp(i2\omega t) \tag{2.10}$$

Substituting Eq. 2.10 into Eq. 2.9,

$$\frac{d^2 T_r}{dr^2}+\frac{1}{r}\frac{dT_r}{dr}-i\frac{2\omega}{\alpha}T_r=0 \tag{2.10}$$

$$q=\sqrt{i\frac{2\omega}{\alpha}}=(1+i)\sqrt{\frac{\omega}{\alpha}}=\sqrt{\frac{2\omega}{\alpha}}\exp(\frac{i\pi}{4}) \tag{2.11}$$

where α is thermal diffusivity, and $1/q$ is the wavelength of the diffusive thermal wave or called thermal penetration depth [1, 2]. Changing the variable from r to $y = qr$,

$$y^2\frac{d^2 T(y)}{dy^2}+y\frac{dT(y)}{dy}-y^2 T(y)=0 \tag{2.12}$$

We can get a Bessel equation of the zeroth order. The solution is given by Carslaw and Jaeger [27]:

$$T_r = \frac{P_0}{2k\pi L} K_0(qr) \tag{2.13}$$

where P_0 is the amplitude of the input power, L is the length of the heating line, and K_0 is the zeroth-order modified Bessel function.

Substituting Eq. 2.13 into Eq. 2.10, temperature distribution can be expressed as,

$$T(r,t) = \frac{P_0}{2k\pi L} K_0(qr) \cdot \exp(i2\omega t) \tag{2.14}$$

If the system is infinite half-volume (Fig. 2.4) and the Joule heating rate is the same, the function of the temperature increase is doubled.

$$T(r,t) = \frac{P_0}{k\pi L} K_0(qr) \cdot \exp(i2\omega t) \tag{2.15}$$

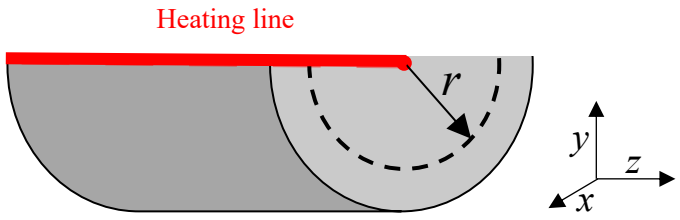

Fig. 2.4 One-dimensional heating line on the surface of the half-cylinder sample.

The above derivation is based on the infinitely narrow heater, but the heating line has a finite width in the actual process. Considering the width of the heating line, the Fourier transform of Eq. 2.15 with respect to the x-coordinate is done (Fig. 2.5). Note the temperature oscillation at the surface is important, so $y = 0$. Now using the Fourier cosine transform, the spatial temperature oscillation can be obtained [28],

$$T(\eta)=\int_0^{\infty}T(x)\cos(\eta x)dx=\frac{P}{\pi kL}\int_0^{\infty}K_0(qx)\cos(\eta x)dx=\frac{P}{2kL}\frac{1}{\sqrt{\eta^2+q^2}} \tag{2.16}$$

where η is the transformation variable.

To add the width of the heating line into Eq. 2.16, the rectangular function of the heating line from -*b* to *b* is multiplied by Eq. 2.16. According to the convolution theorem, the function in the *x*-space can be obtained,

$$T(\eta)=\frac{P}{2kL}\frac{1}{\sqrt{\eta^2+q^2}}\int_0^{\infty}\mathrm{rect}(x)\cos(\eta x)dx=\frac{P}{2kL}\frac{\sin(\eta b)}{\eta b\sqrt{\eta^2+q^2}} \tag{2.17}$$

The inversion formula is,

$$T(x)=\frac{P_0}{k\pi L}\int_0^{\infty}\frac{\sin(\eta b)\cos(\eta x)}{\eta b\sqrt{\eta^2+q^2}}d\eta \tag{2.18}$$

where *b* is the half width of the heater.

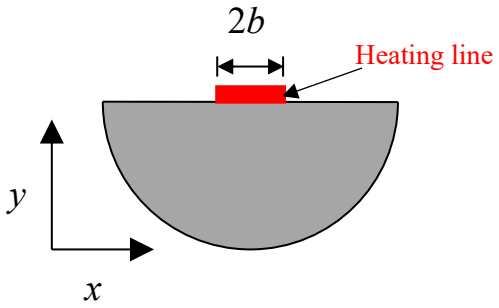

Fig. 2.5. Finite width heating line on the surface of the half-cylinder sample.

As a result of the fact that the thermometer and the heater are one in the same element, the temperature that is measured is some sort of average temperature across the length of the line. To obtain an average value for Eq. 2.18, integrate it with respect to *x* from 0 to *b* and then divide the result by *b*. This will give the temperature that was measured by the thermometer,

$$\Delta T_{avg.} = \frac{1}{b}\int_0^b T(x)dx = \frac{P_0}{\pi Lk}\int_0^\infty \frac{\sin^2(\eta b)}{(\eta b)^2\sqrt{\eta^2+q^2}}d\eta \qquad (2.19\ )$$

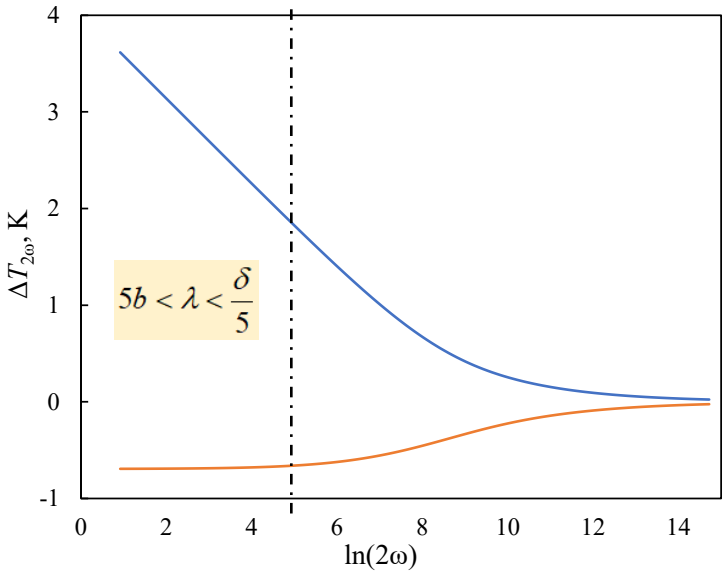

Fig. 2.6 Temperature oscillations vs. natural logarithm of the angular frequency.

2.2.1 Slope method for bulk sample

The slope method is mostly used the measurement mode of the 3-omega method for the thermal conductivity of the bulk samples. When the width $2b$ of the heating line is much smaller than the thermal penetration depth λ during the measurement by modulating the driving heating frequency, such that

$$\lim_{b\to 0}\frac{\sin(b\eta)}{b\eta} = 1 \qquad (2.20)$$

Now that the amplitude of the large wavenumber oscillations is relatively negligible and decays quickly, the integral is dominated by the wavenumber between $1/\lambda < \eta < 1/b$. This is because the amplitude of the large wavenumber oscillations has become comparatively insignificant. Substituting Eq. 2.20 into Eq. 2.19 and setting the upper limit of integration to $1/b$, the amplitude of the average temperature of the heater $\Delta T_{2\omega}$ can be

approximated as,

$$\Delta T_{2\omega} \approx \frac{P_0}{\pi L k}\int_0^{1/b}\frac{1}{\sqrt{\eta^2+q^2}}d\eta = \frac{P_0}{\pi L k}\{\ln 2 - \ln(qb)\} \tag{2.21}$$

Substituting Eq. 2.11 for Eq. 2.21,

$$\Delta T_{2\omega} = -\frac{P_0}{2\pi L k}\left[ln(2\omega)+ln\left(\frac{b^2}{\alpha}\right)-3+\gamma\right]-i\frac{P_0}{4Lk} \tag{2.22}$$

where γ is the Euler-Mascheroni constant. The thermal conductivity of the sample (k) can be derived from the slope of the real part of $\Delta T_{2\omega}$ against ln(2ω).

$$k = -\frac{P_0}{2\pi L\dfrac{\partial \mathrm{Re}(\Delta T_{2\omega})}{\partial ln(2\omega)}} \tag{2.23}$$

The temperature oscillation $\Delta T_{2\omega}$ can be obtained from $V_{3\omega}$ as shown in Eq. 2.7.

$$k = \frac{-I_0{}^3 R_0}{8\pi L\dfrac{\partial V_{3\omega}}{\partial \ln(2\omega)}}\frac{dR}{dT} \tag{2.24}$$

If we measure R_0 and dR/dT in advance, the thermal conductivity of the sample can be obtained through the measurement of $V_{3\omega}$.

2.2.2 Differential 3-omega method for the thin films

The differential 3-omega method for the thin films, which is an extension of the slope method, can measure the thermal conductivity of a thin film between the heater and substrate, as shown in Fig. 2.7.

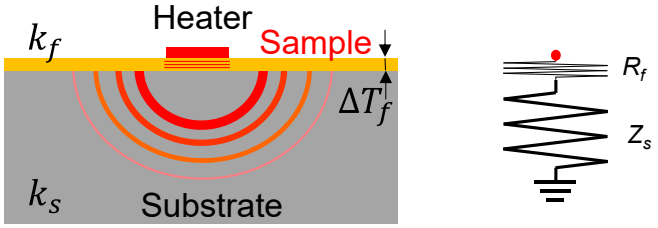

Fig. 2.7 The schematic diagram of the measurement of the thin film.

When the thermal penetration depth is much larger than the thickness of the thin film and the thermal conductivity of the thin film is smaller than the substrate, the thin film behaves as a constant thermal resistance independent of heating frequency. Dames [7] shows that the penetration depth should be 20 times larger than the line width $2b$ to obtain an uncertainty below 5%.

$$R_f = \frac{\Delta T_f}{P_0} = \frac{\delta}{2bk_f L} \tag{2.25}$$

where δ is the thickness of the thin film, R_f is the thermal resistance of the thin film. Due to the presence of the thin film, the total impedance Z during the measurement becomes to

$$\begin{aligned} Z = Z_s + R_f &= \frac{\Delta T_{2\omega\_s}}{P_0} + \frac{\Delta T_f}{P_0} \\ &= -\frac{1}{2\pi L k_s}\left[ln(2\omega) + ln\left(\frac{b^2}{\alpha}\right) - 3 + \gamma \right] - i\frac{1}{4Lk_s} + \frac{\delta}{2bk_f L} \end{aligned} \tag{2.26}$$

where the subscript s is the substrate, and f is the thin film. Note the power P should be the same with and without the thin film during the derivation. The total impedance Z is

$$Z = \frac{\Delta T_{2\omega\_total}}{P_0} = \frac{2V_{3\omega}}{V_0 \beta P_0} \tag{2.27}$$

where $\Delta T_{2\omega\_total}$ is the temperature oscillation with the thin film. The thermal conductivity of the thin film can be written as

$$k_f = \frac{P_0 \delta}{2bL(\Delta T_{2\omega\_total} - \Delta T_{2\omega\_s})} \tag{2.28}$$

Figure 2.8 shows the schematic of the temperature oscillation versus heating frequency for the cases with and without target thin film. From the temperature difference between

the two states, we can obtain the thermal conductivity of the sample.

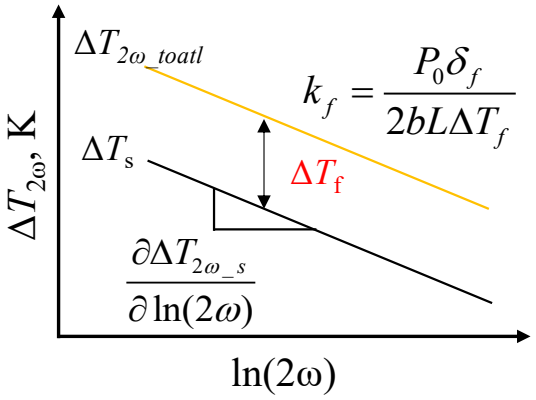

Fig. 2.8 Experiment plot of the thermal conductivity of the thin film measurement.

2.2.3 Bi-directional 3-omega method for the liquid/bio samples

The bi-directional 3-omega method has been employed to measure the thermal conductivity of liquid samples [10-14] and bio-samples [15-17] because they are easy to keep full contact with the heating line. When the sample is placed above the heater of the 3-omega method, the temperature oscillation $\Delta T_{2\omega}$ contains the information of the substrate and the sample, as shown in Fig. 2.9 where Z_s and Z_{samp} denote thermal impedance in the substrate side and sample side.

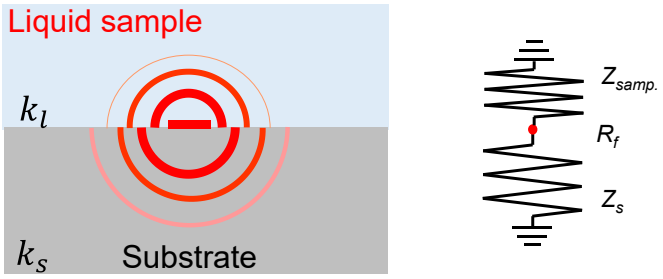

Fig. 2.9 The schematic diagram of the bi-directional 3-omega method.

In the bi-directional 3-omega method, Heat flows upward and downward from the heater. Assuming the boundary mismatch assumption (BMA) [17], which neglects the

heat transport between the sample above the heater and the substrate, the thermal impedance between the heater and the ambient can be expressed by the following equation.

$$Z^{-1} = Z_{samp.}^{-1} + Z_s^{-1} \tag{2.29}$$

In the low-frequency range where the slope method is applicable, the temperature oscillation $\Delta T_{2\omega\_total}$ can be written as

$$\Delta T_{2\omega\_total} = -\frac{P_0}{2\pi L(k_s + k_{samp.})}\left[ln(2\omega) + ln\left(\frac{b^2}{\alpha}\right) - 3 + \gamma\right] - i\frac{P_0}{4L(k_s + k_{samp.})} \tag{2.30}$$

$$\frac{\partial \Delta T_{2\omega\_total}}{\partial \ln(2\omega)} = \frac{-1}{2\pi L(k_s + k_{samp.})} \tag{2.31}$$

The slope of the temperature amplitude with respect to ln(2ω) gives the sum of the thermal conductivity of the sample and the substrate ($k_{samp.} + k_s$) as shown in Eq. 2.31. Thus the thermal conductivity of the sample $k_{samp.}$ can be determined by subtracting the k_s measured in advance from $k_{samp.} + k_s$.

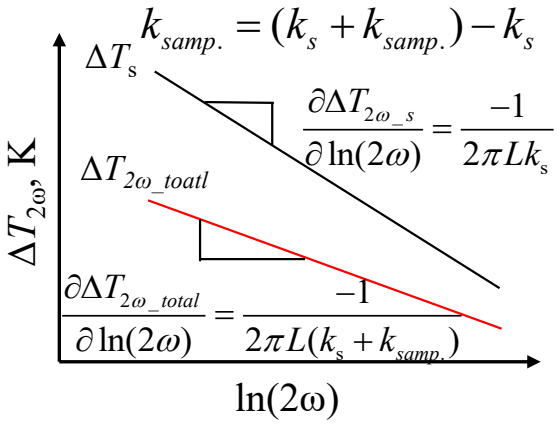

Fig. 2.10 Experiment plot of the thermal conductivity measurement of the samples using the bi-directional 3-omega method.

2.3 Measurement system of 3-omega method

The theory of the 3-omega was expressed in the above process, and we can use the 3-omega to measure the thermal conductivity of the bulk, thin films, liquid, and biosamples. To measure the thermal conductivity, we will design the experimental circuit and make the LabVIEW program.

2.3.1 Experimental circuit

To build the experimental circuit, first, there are several issues to be solved: (1) the constant and low noise AC supply to the heater, (2) the targeted signal capture, and the signal measurement method. After solving these issues, we can build the experimental circuit and make the LabVIEW program.

(1) Voltage to current converter

From the theory of the 3-omega method, the alternative current was input to the heater and measured the generated voltage. Generally, the function generator is a voltage source. To transduce the voltage to current, a converter is needed.

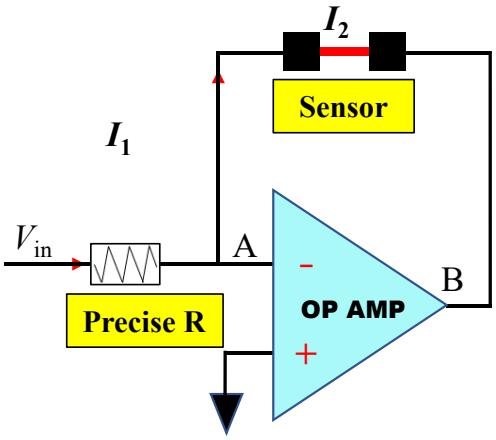

Fig. 2.11 voltage to current converter.

Here, we employed an inverting amplifier circuit. The advantages list as follows:

1. The output is going to be out of phase with the input. That helps to prevent oscillation

and instability.

2. Both inputs are within millivolts of the ground all the time, so you can forget about common-mode offsets and issues.
3. Both inputs have a low impedance to the ground, so capacitive coupling into the op-amp will be low.

The operational amplifier is OPA 551 (Fig. 2.12). It's unity-gain stable and features a high slew rate (15V/μs) and wide bandwidth (3MHz), and low noise (14nV/$\sqrt{\text{Hz}}$). OPA 551 is internally protected against overtemperature conditions and current overloads.

According to the rules for Op-Amps, the voltage of the '-' and '+' terminal is 0. They are both on the virtual ground. The current through the precise resistor is equal to the sensor but inverting.

$$I_1 = I_2 = \frac{V_{\text{in}}}{R_{\text{prec.}}} = \frac{-V_{\text{B}}}{R_{\text{sensor}}} \tag{2.31}$$

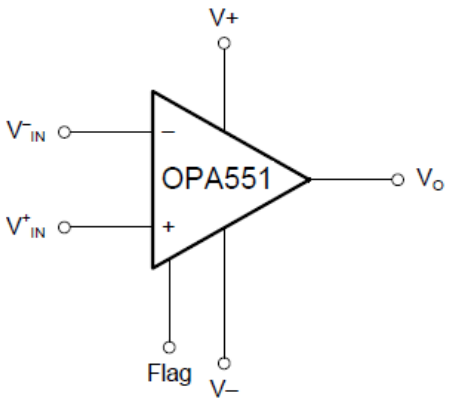

Fig. 2.12 Simplified functional diagram of OPA 551.

(2) Differential amplifier circuit

The differential amplifier is a voltage subtractor circuit that produces an output voltage proportional to the voltage difference of two input signals applied to the inputs of the inverting and non-inverting terminals of an operational amplifier. By using the differential

amplifier, we can measure the voltage drop across the resistor.

In this study, we made two differential amplifier circuits. The first circuit used the amplifier INA 111 (Fig. 2.13). The INA111 is a high-speed, FET-input instrumentation amplifier offering excellent performance. The INA111 uses a current-feedback topology providing extended bandwidth (2MHz at G = 10) and fast settling time (4ms to 0.01% at G = 100). A single external resistor sets any gain from 1 to over 1000. Offset voltage and drift are laser trimmed for excellent DC accuracy. The INA111's FET inputs reduce input bias current to under 20pA, simplifying input filtering and limiting circuitry. The second circuit used the amplifier ADA4817-1 (Fig. 2.14). The ADA4817-1 (single) FastFET™ amplifiers are unity-gain stable, ultrahigh-speed, voltage feedback amplifiers with FET inputs. These amplifiers were developed with the Analog Devices, Inc. proprietary extra fast complementary bipolar (XFCB) process, which allows the amplifiers to achieve ultralow noise (4 nV/√Hz; 2.5 fA/√Hz) as well as very high input impedance. With 1.3 pF of input capacitance, low noise (4 nV/√Hz), low offset voltage (2 mV maximum), and 1050 MHz−3 dB bandwidth, the ADA4817-1 is ideal for data acquisition front ends as well as wideband transimpedance applications, such as photodiode preamps. Depending on the bandwidth of the two types of differential amplifiers, one circuit for low-frequency range measurement and one circuit for high-frequency measurement were built for the research study shown in chapter 3 and chapter 4, respectively.

In the 3-omega method, the voltage drops across the heater contain 1ω and 3ω signals, and the amplitude of $V_{1\omega}$ is almost 1000 times larger than the $V_{3\omega}$. To enhance the measurement resolution, the $V_{1\omega}$ of the heater should be removed. From the V-I converter circuit, we found that the voltage drop across the precise resistor only contains the 1ω signal because the precise resistor has a very low tolerance value (closely near its nominal

value). We can remove the 1ω signal component of the heater by subtracting the 1ω voltage of the precise resistor. However, the resistance of the heater and precise resistor is not the same, and when the amplitude of the input current is the same, their amplitudes of the 1ω voltage are different. To obtain a similar amplitude of the precise resistor and the heater, we used a variable resistor as the voltage divider to change the amplitude of the $V_{1\omega}$ of the precise resistor, as shown in Fig. 2.15.

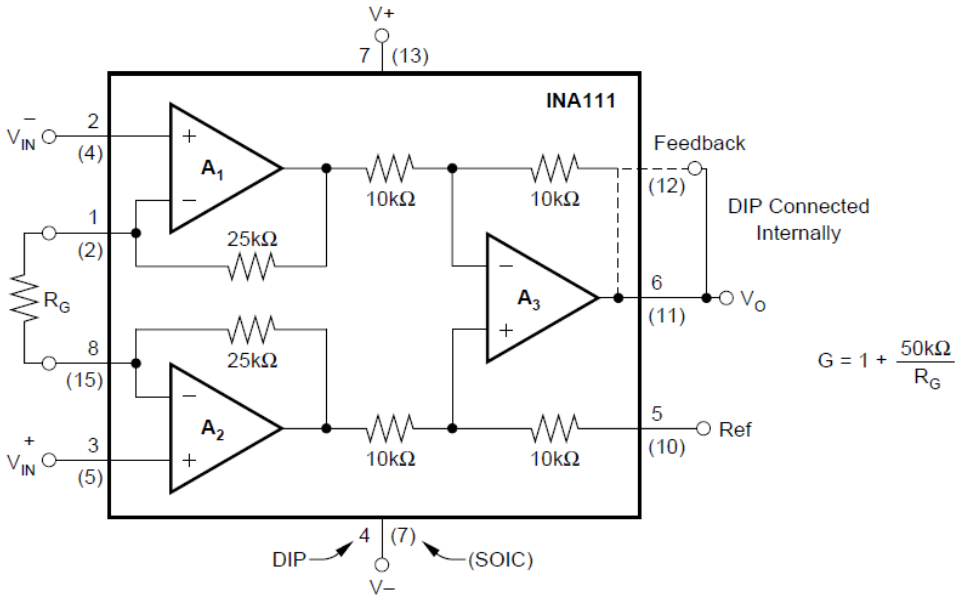

Fig. 2.13 Simplified functional diagram of INA 111.

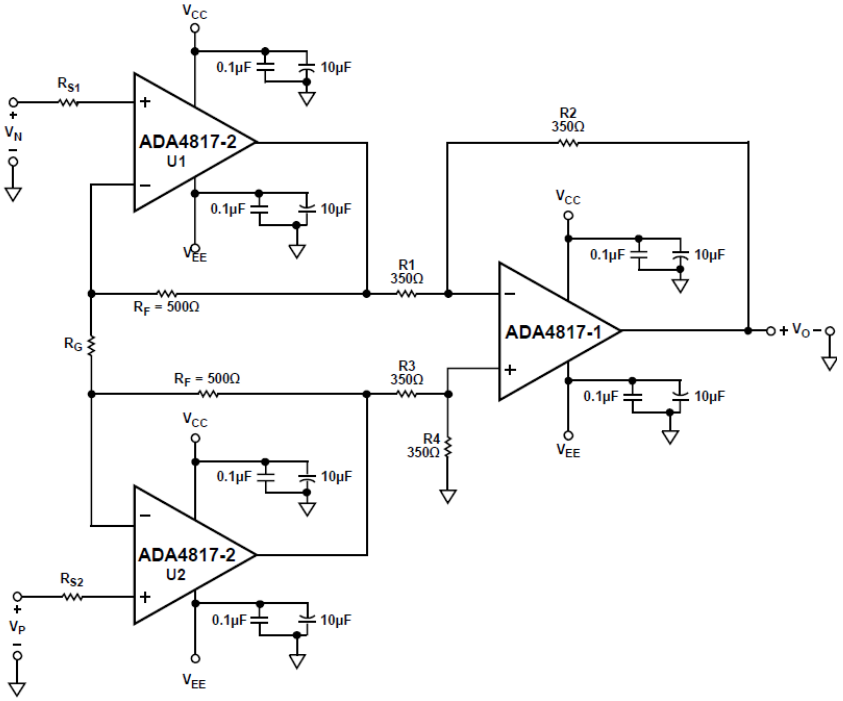

Fig. 2.14 Simplified functional diagram of ADA4817-1.

The two unity-gain differential amplifiers were employed to measure the voltage of the precise resistor and the heater, and the 51 times gain was employed to enlarge the amplitude of $V_{3\omega}$ for high-resolution measurement.

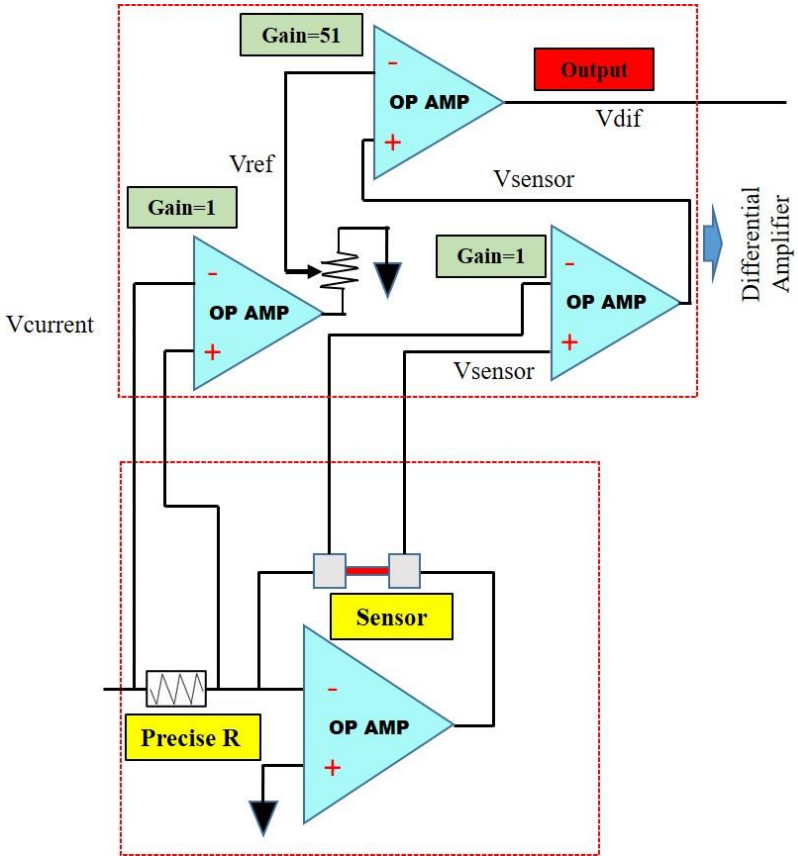

Fig. 2.15 The differential amplifier circuit for $V_{1\omega}$ of the heater.

Note when we used the differential amplifier, the capacitors used to reduce the noise should be close to the body of the differential amplifier. The performance of the differential amplifier circuit will be tested in chapter 2.6.

(3) Dual-phase lock-in amplifier

The lock-in amplifier is based on correlation detection technology. The frequency of the reference signal is related to the frequency of the measured signal but not to the frequency of the noise. It is a gadget that separates the valuable signal from the background noise (Fig. 2.16). It is one of the most efficient methods for detecting a weak signal.

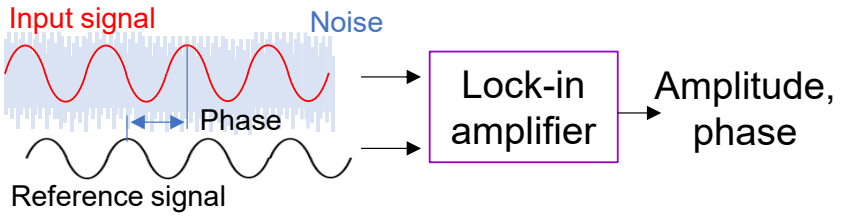

Fig. 2.16 The schematic of the lock-in amplifier operation.

The conventional lock-in amplifier consists solely of analog components. It has a short lifespan and is slow. It ages easily and will produce additional noise. In addition, it has issues such as low precision, zero drift, etc. Popular in recent years is the construction of digital lock-in amplifiers. It offers several advantages over the analog lock-in amplifier, including high speed, great real-time performance, high precision, and the ability to easily record data, debug, enhance, update, and transplant. In addition, dual-phase lock-in amplifiers eliminate the inaccuracy caused by the phase shift circuit employed by single-phase lock-in amplifiers, thereby significantly enhancing the detection accuracy.

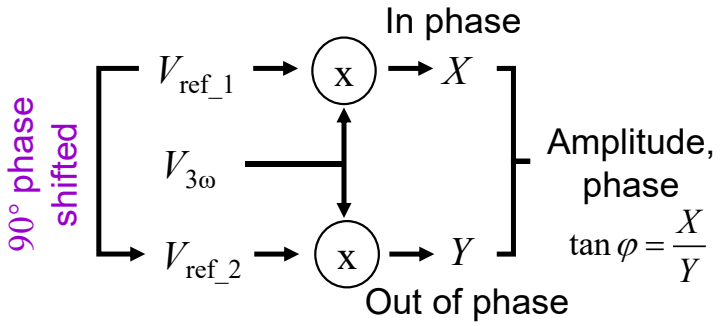

Fig. 2.17 The schematic of the dual-phase lock-in amplifier operation.

Figure 2.17 depicts the dual-phase lock-in amplifier's operating concept. The dual-phase lock-in amplifier consists of two phases, 0 degrees and 90 degrees, and two reference signals. The frequency of the reference signal is always the same as the frequency of the measured signal. The amplitude and phase of the observed signal can

then be obtained precisely by multiplying the measured signal by two phase-orthogonal reference signals.

Then the in-phase value *X*, out-of-phase value *Y*, and the phase between the in-phase and out-of-phase values can be obtained.

$$V_{ref\_1} = A \times \sin(\omega t) \tag{2.32}$$

$$V_{ref\_2} = A \times \sin(\omega t + \frac{\pi}{2}) \tag{2.33}$$

$$X = \frac{1}{2} V_{3\omega} A \cos\phi \tag{2.34}$$

$$Y = \frac{1}{2} V_{3\omega} A \sin\phi \tag{2.35}$$

$$\tan\phi = \frac{X}{Y} \tag{2.36}$$

$$R = \frac{2}{A}\sqrt{(X^2 + Y^2)} \tag{2.37}$$

where A is the amplitude of the reference signal, Φ is the phase between the in-phase and out-of-phase value, and R is the amplitude of the measurement signal. To simplify the calculation process, the amplitude A of the reference signals was usually set to 1 V.

In this study, the function of the dual-phase lock-in amplifier was realized using the LabVIEW program made by ourselves. In the program, the phase-locked loop (PLL) was employed to generate the 3ω reference signal to lock in the $V_{3\omega}$. It is a control system that produces an output signal whose phase is proportional to the phase of an input signal. There are numerous types, with the simplest consisting of an oscillator with variable frequency and a phase detector in a feedback loop. The frequency and phase of the oscillator are proportionally regulated by an applied voltage, hence the phrase voltage-controlled oscillator (VCO). The oscillator produces a periodic signal with a certain frequency, and the phase detector compares the phase of that signal to the phase of the

periodic input signal in order to regulate the oscillator such that the phases remain matched. Maintaining lockstep between the input and output phases also necessitates matching the input and output frequencies. A phase-locked loop can therefore follow an input frequency or generate a frequency that is a multiple of the input frequency in addition to synchronizing signals. These features are utilized for the synchronization of computer clocks, demodulation, and frequency synthesis.

(4) Voltage follower

An op-amp circuit known as a voltage follower has an output voltage that is identical to the input voltage (it "follows" the input voltage). Other names for this type of amplifier are buffer amplifier, unity-gain amplifier, and isolation amplifier. As a result, a voltage follower op-amp has a gain of 1 and does not amplify the input signal.

The main component of the voltage follower is the operational amplifier with a high impedance, generally from 1 MΩ to 10 TΩ, leading to a very small input current. But if the circuit with a low impedance load, what's going to happen? As shown in Fig. 2.18, the current will become high. Hence the circuit takes a large amount of power from the power source, resulting in high source disturbances.

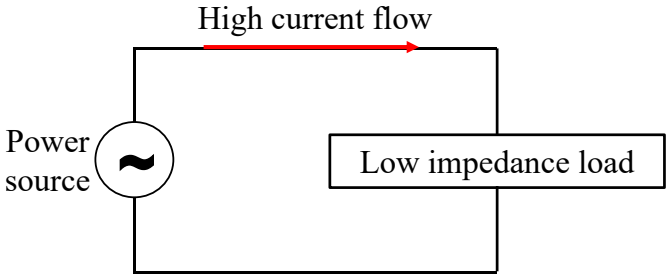

Fig. 2.18 The circuit with a low impedance load.

Using the voltage follower (Fig. 2.19), the op-Amp just adjusts its output voltage equal

to the input voltage. The input side with a high impedance caused a small current flow, and the output side with a small impedance caused a high current flow. The op-amp drives the load as if it were a perfect voltage source due to its extremely low output impedance. Bridge connections are used for both the input and output of the buffer. This leads to less source power being consumed and less distortion due to overload.

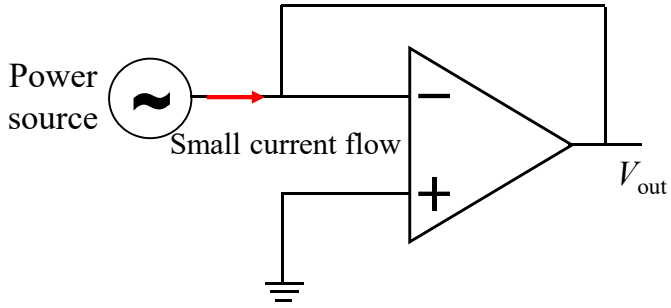

Fig. 2.19 The schematic of the voltage follower: the circuit with a high impedance using the op-Amp.

(5) 4-probe measurement method

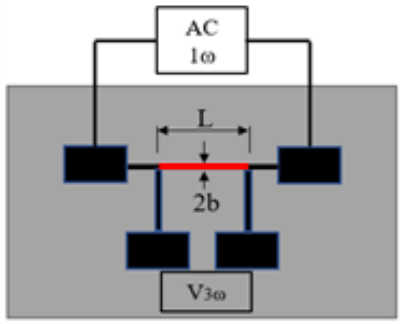

Fig. 2.20 The schematic of the 4-probe measurement method.

The 4-probe method is used to measure the electrical resistance of the thin films. When we measured the resistance of the thin film heater, the contact resistance would appear at the position between the electrode and the film. So, there generates a voltage drop across the contact resistance. Using the 4-probe method, the important thing is the input

impedance of the measuring instrument is huge, and almost no current flow through the electrode. The effect of the contact resistance can be neglected, which enhanced the measurement accuracy compared to the 2-probe method.

The major problems in the aforementioned study have been resolved. The entire experimental circuit was created by combining the voltage-to-current converter, the differential amplifier circuit, and the voltage buffer. The data acquisition device, a laptop with the self-made LabVIEW program, was also added (Fig. 2.21). The data acquisition device we used was the NI PXIe-4303. The NI PXIe-4302/4303 provides 32 simultaneously sampled filtered analog input channels. The NI PXIe-4302 can operate at sample rates up to 5 kS/s/ch, and the NI PXIe-4303 can operate at sample rates up to 51.2 kS/s/ch. These modules can measure an analog voltage of up to 10 V when using the TB - 4302 and can measure 20 mA current signals when using the TB-4302C. Each channel has a 24-bit ADC and selectable digital filters to reject out-of-band noise.

The experimental circuit's schematic diagram is shown in Fig. 2.21, and the experimental circuit's design for the 3-omega approach is shown in Fig. 2.22. The wires used in the experimental circuit should cover the shield or twist to reduce the electrostatic noise.

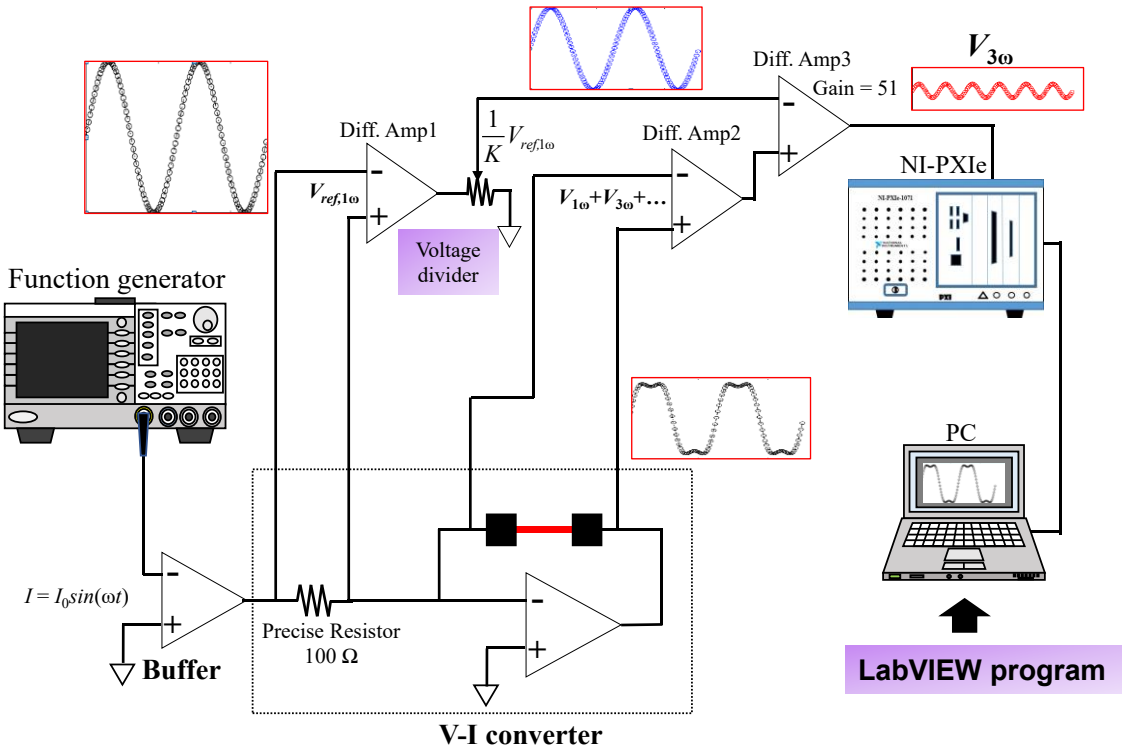

Fig. 2.21 The schematic of the experimental circuit for the 3-omega method.

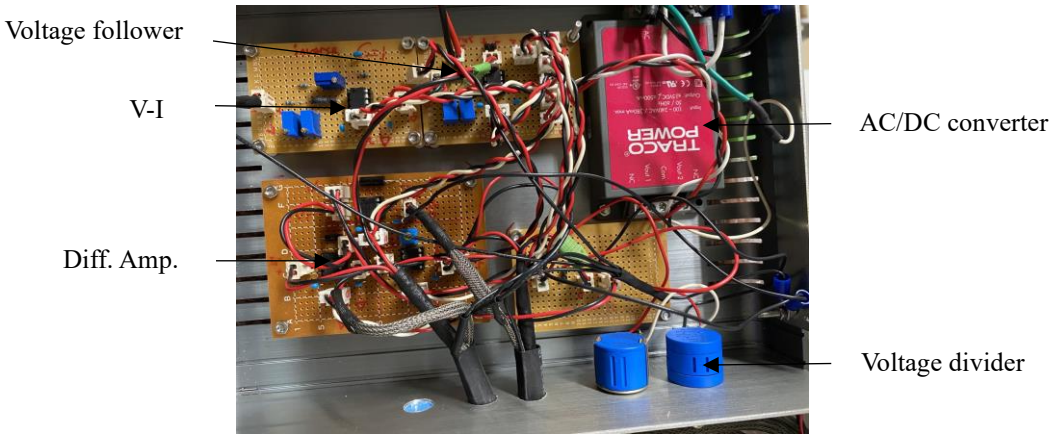

Fig. 2.22 Experimental circuit made according to the schematic.

2.3.2 LabVIEW program

LabVIEW has been widely employed for the measurement of various signals because of its ability to quickly facilitate taking measurements. In comparison to traditional programming environments, LabVIEW is easier to automate the capture, validation, and taking of measurements. Of course, you can use different lab tools to record signals and do tests (scopes, analyzers, multimeters). Using LabVIEW, all that is required is the placement of a front panel object for a graph or chart and the connecting of the desired data to the indication.

In this study, by using LabVIEW, we built one fundamental lock-in program to capture all the raw data of the measurement., and one advanced dual-phase lock-in program to measure the in-phase, out-of-phase, and phase of the $V_{3\omega}$.

(1) Lock-in program

The lock-in program is mainly used to capture the amplitude of raw signals during the experimental measurement. The measured signals include experimental temperature T, $V_{1\omega}$ of the precise resistor, $V_{3\omega}$ of the sensor, $V_{1\omega}$ of the voltage divider, and 1ω reference signal, as shown in Fig. 2.23. The lock-in process is implemented through the Extract Single Tone Information VI in LabVIEW (Fig. 2.24).

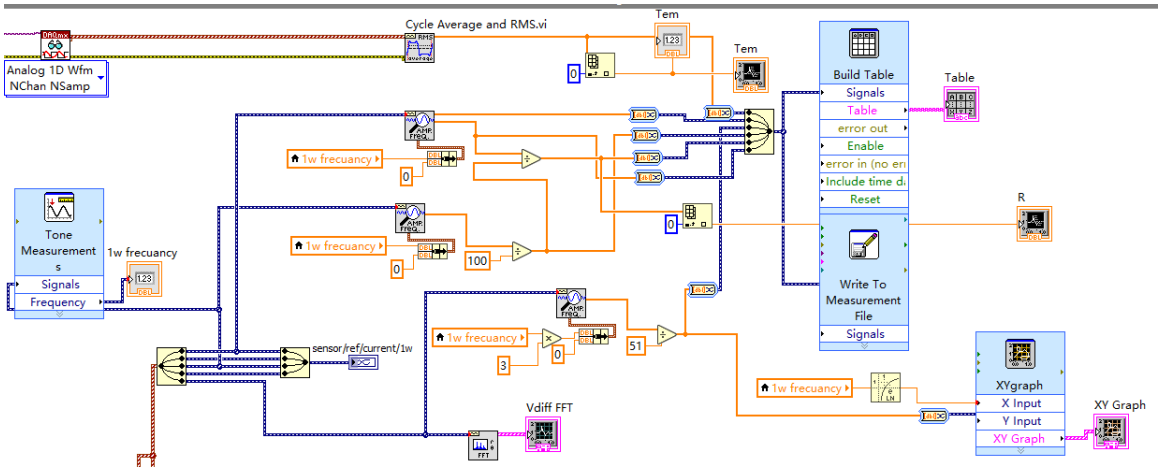

Fig. 2.23 The LabVIEW program for raw data measurement of the 3-omega method.

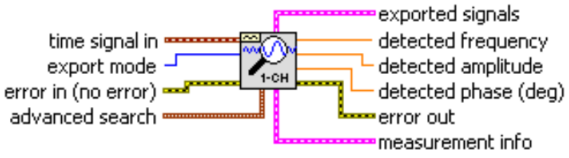

Fig. 2.24 Extract Single Tone Information VI.

The fundamental lock-in program can also determine the $V_{3\omega}$ of the sensor, but the accuracy is lower than the used dual-phase lock-in program and can't get the in-phase and out-of-phase value of the $V_{3\omega}$. On the other hand, by using a lock-in program, we can measure the temperature coefficient of resistance (TCR). The fast Fourier transform function (FFT) was used to check the amplitude of the 1ω and 3ω components of the sensor after modifying the resistance of the voltage divider for the high measurement resolution.

(2) Dual-phase lock-in program

Fig. 2.25 is the dual-phase lock-in program. By using PLL, we accurately capture the $V_{3\omega}$ of the sensor. By dual-phase lock-in process, we determined the in-phase, out-of-phase, and the phase of $V_{3\omega}$ of the sensor.

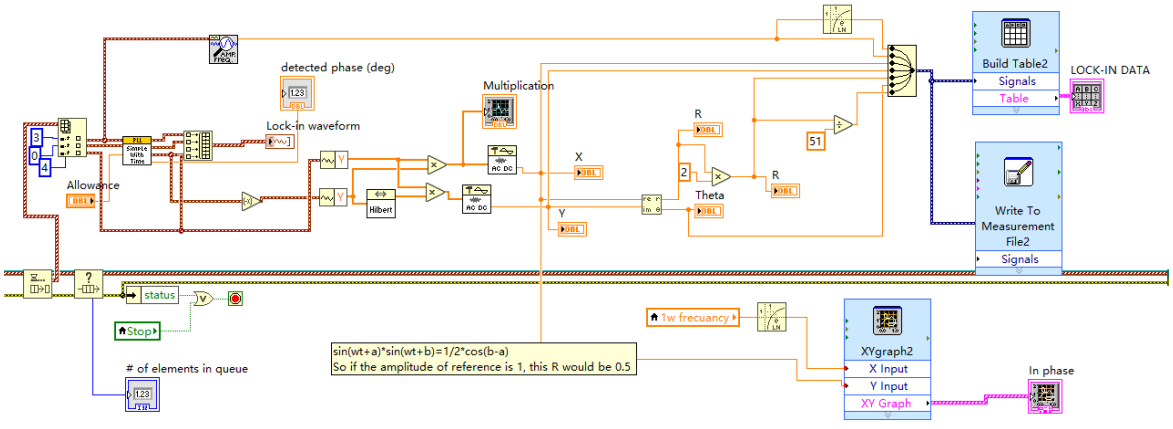

Fig. 2.25 The dual-phase lock-in amplifier LabVIEW program.

(3) Front panel

Fig. 2.26 is the front panel of the 3-omega measurement program. From the front panel, we can see that the program contains three sections: (1) the measurement conditions: the sample rates (Hz), number of samples per channel, minimum/maximum value, and error display, (2) the display for the lock-in program measurement, (3) the display for the dual-phase lock-in program.

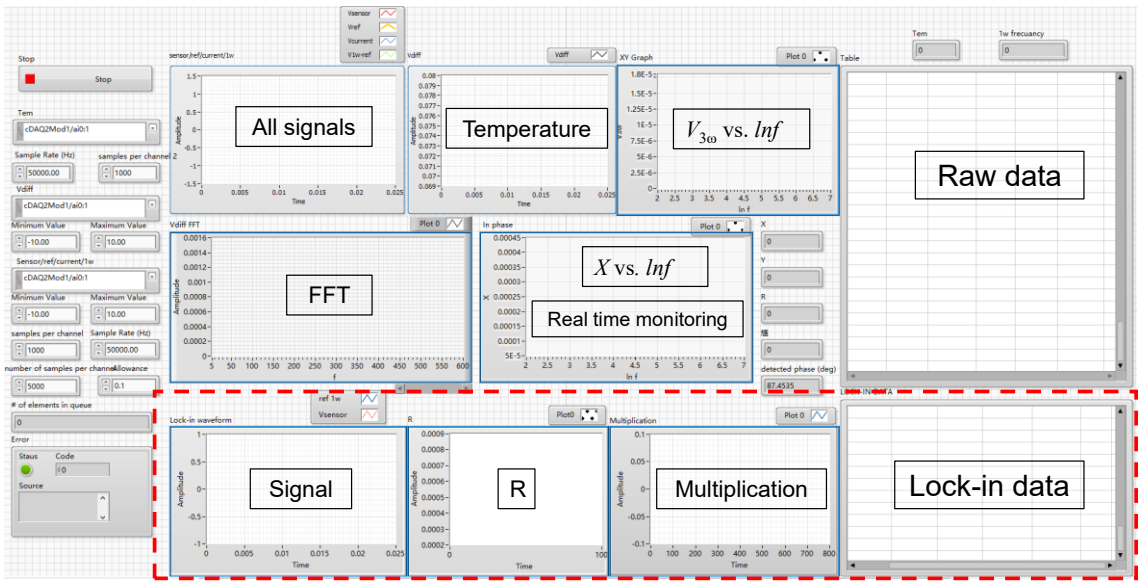

Fig. 2.26 The front panel of the whole LabVIEW program.

From the front panel, we can monitor the experimental process in real-time.

2.4 Measurement system testing

Depending on the purpose of the experiment, the performance requirement of the experimental circuit is different. Generally, the low-frequency measurement range is sufficient for the thermal conductivity of the large-size samples, and the high-frequency measurement range is required for the small-size sample to keep the thermal penetration depth within the samples. On the other hand, the amplitude of $V_{3\omega}$ of the sensor is small, and the V_{noise} should be much smaller than the $V_{3\omega}$ of the sensor.

The cutoff frequency and noise level during the experiment were used to test the performance of the measurement system.

2.4.1 Cutoff frequency

The cutoff frequency or corner frequency is the frequency either above or below which the power output of a circuit. Most frequently, this proportion is one-half the passband power, also referred to as the 3 dB point, since a fall of 3 dB corresponds to approximately half power. As a voltage ratio, this is a fall to $\sqrt{1/2} = 0.707$ of the passband voltage.

(1) Cutoff frequency of the experimental circuit with the voltage divider

Fig. 2.28 and Fig. 2.29 are variations of the phase and amplitude of the last differential amplifier (Diff.Amp3) with the heating frequency increasing compared to the $V_{1\omega}$ of the precise resistor, respectively, when the experimental circuit contains the voltage divider. In this circuit, the cutoff frequency is around 100 kHz. However, when the heating frequency is over 20 kHz, the phase shift of the output signal becomes large. To accurately determine the in-phase and out-of-phase values, the phase should keep constant in this

test. As a result, this circuit will be employed to measure the thermal conductivity of the large-size samples using the slope method.

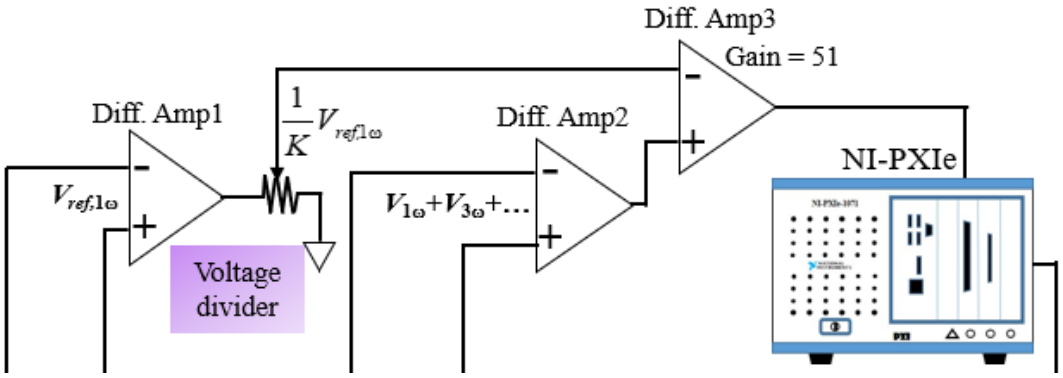

Fig. 2.27 The experimental circuit with the voltage divider.

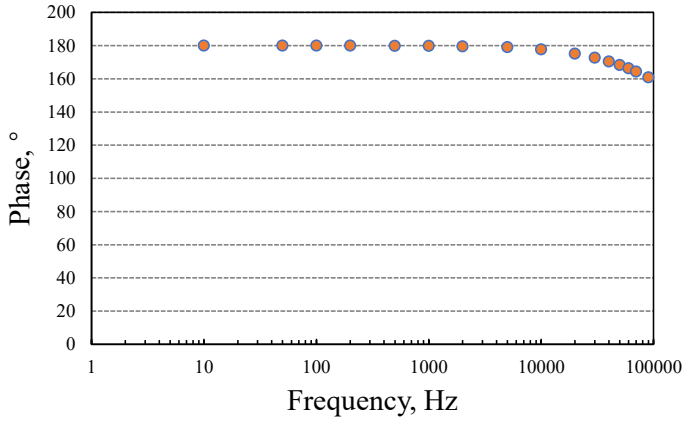

Fig. 2.28 The phase change during measurement with the voltage divider.

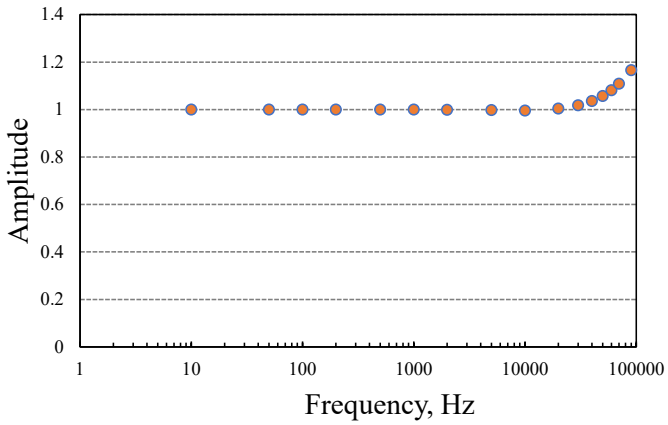

Fig. 2.29 The amplitude change during measurement with the voltage divider.

(2) Cutoff frequency of the experimental circuit without voltage divider

The measurement frequency range of the above experimental circuit is insufficient for the small size sample which the thickness is at the ten-micro meter scale, such as coated films, single cell, and bio tissues. With a thorough check of the experimental circuit, we found that the voltage divider will generate a big phase delay with the heating frequency increasing. Fig. 2.30 is the experimental circuit without the voltage divider. From Fig. 2.31 and 2.32, it's shown that the cutoff frequency of the new experimental circuit is over 1 MHz and the phase without phase delay. As a result, we can use this circuit to measure the thermal conductivity of the small-size samples.

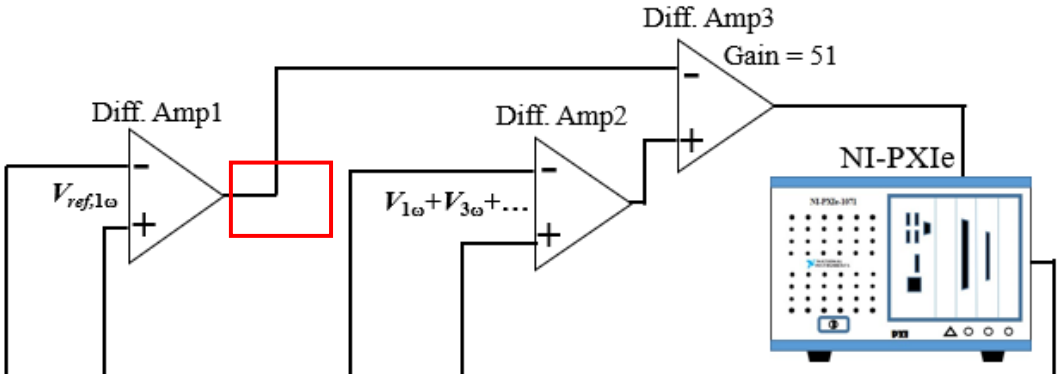

Fig. 2.30 The experimental circuit without voltage divider.

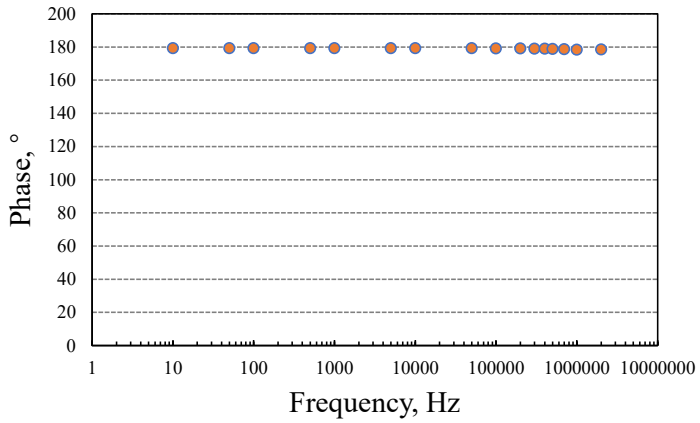

Fig. 2.31 The phase change during measurement without voltage divider.

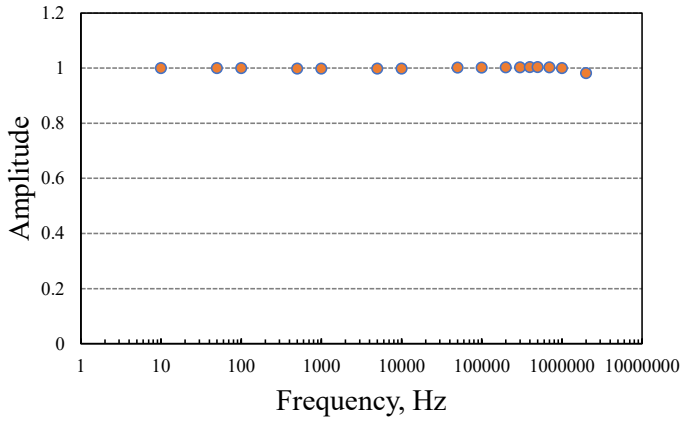

Fig. 2.32 The amplitude change during measurement without the voltage divider.

2.4.2 Noise level

The noise level was measured using the multi-functional and high-resolution digital lock-in amplifier (MFLI 500 kHz/5MHz, Zurich Instrument). Fig. 2.33 shows the amplitude of $V_{1\omega}$, $V_{2\omega}$, and $V_{3\omega}$ of the sensor measured by the built-in measurement program FFT analyzer. The V_{noise} at the 300 nV scale is much smaller than the amplitude of the $V_{3\omega}$, without effect on our measurement.

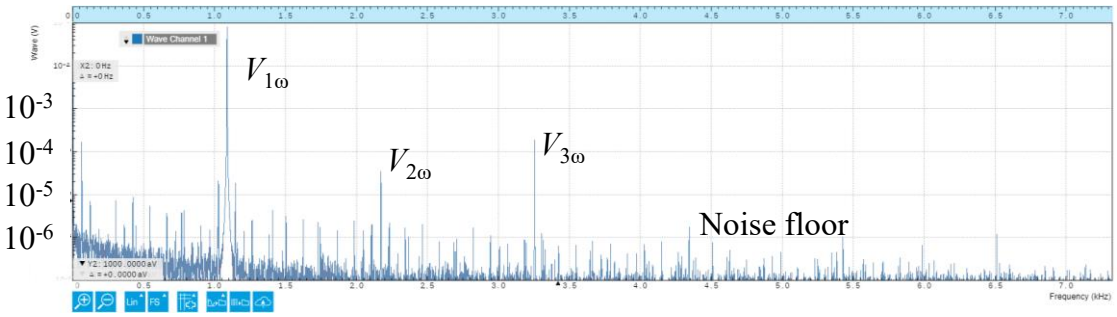

Fig. 2.33 The measurement amplitude of target signals and noise by FFT.

Figure 2.34 shows the temperature fluctuation during the experimental measurement. From this graph, we can see under the different heating frequencies, the temperature

fluctuation is below 0.5 mK during the measurement, which can be ignored compared to the amplitude of the $\Delta T_{2\omega}$.

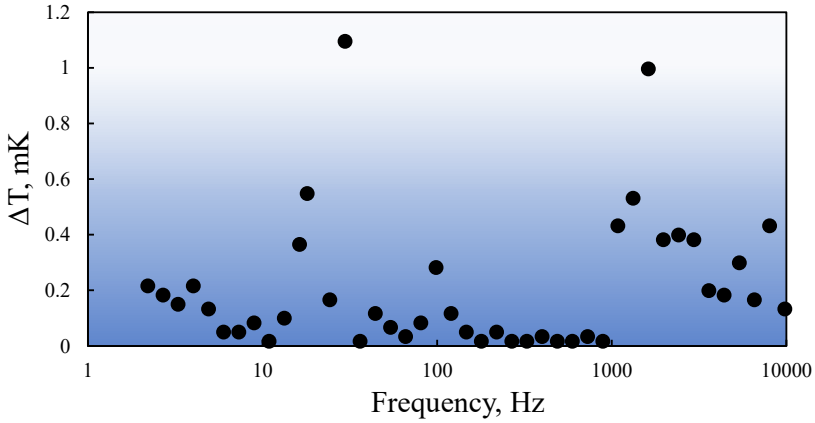

Fig. 2.34 The temperature fluctuation during the experimental measurement.

From Fig. 2.33 and 2.34, we proved the performance of our measurement systems to be very superior.

2.5 TCR measurement

The temperature coefficient of resistance (TCR), $\beta = \frac{dR}{R_0 dT}$, is a key parameter of the 3-omega measurement, which is directly related to the amplitude of the $V_{3\omega}$ of the sensor. To measure the TCR of the heater, we should measure the dR/dT. First, put the sensor into the Oven, and set the temperature. Next, wait for the temperature inside Oven to become stable, and measure the resistance of the heater using the experiment circuit at the 1000 Hz sample rate. For AC signal measurement, the voltage noise density over 1000 Hz becomes minimum, as shown in Fig. 2.35. Finally, change the temperature of the Oven and repeat the previous measurement step. The relation between the resistance and temperature of the heater can be obtained, as shown in Fig. 2.36. The slope of the plot is

the dR/dT.

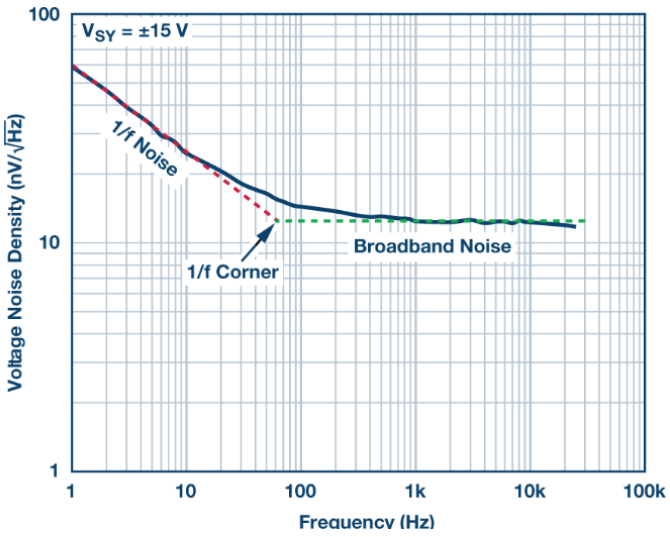

Fig. 2.35 The voltage noise spectral density. (https://www.analog.com)

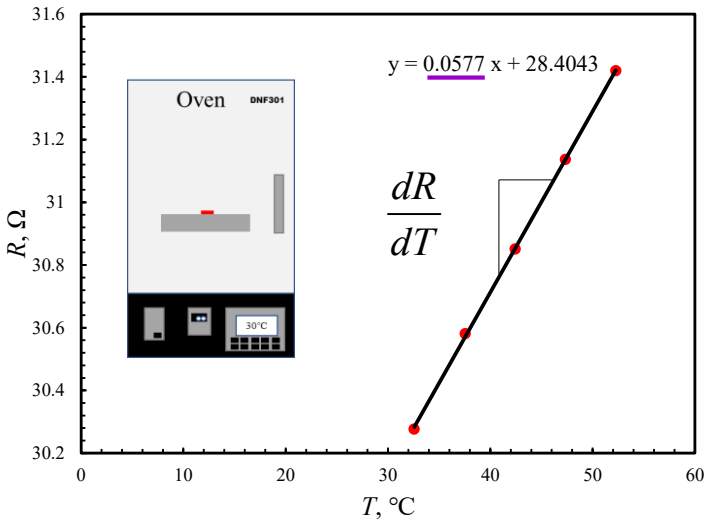

Fig. 2.36 The plot for TCR determination of heater.

After measuring the dR/dT, the nominal resistance of the heater without heating, R_0, should be measured. During the thermal conductivity measurement process, change the input amplitude of the alternative input current and measure the $V_{1\omega}$ of the heater, the relation between the heating power and resistance can be obtained, as shown in Fig. 2.37.

The intercept of the plot is R_0.

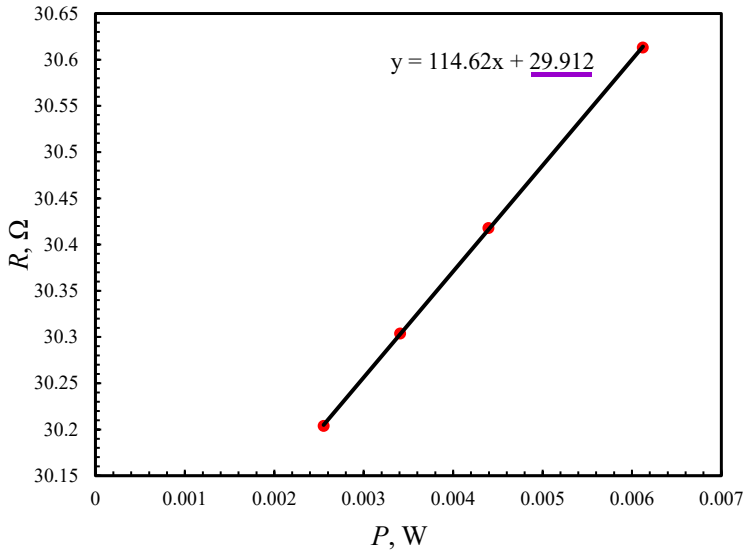

Fig. 2.37 The plot of R_0 determination.

2.6 Summary

In this chapter, we expressed the theory of the 3-omega method, and the extensional methods according to the traditional 3-omega method for the different applications. To measure the thermal conductivity of the sample, we built the experimental circuit and the LabVIEW program. Because the cutoff frequency with and without the voltage divider is different, the two types of circuits will be employed to the measured thermal conductivity of the different size samples, respectively. The noise level of the built experimental circuit is much lower than the amplitude of the $V_{3\omega}$ of the heater.

Next, we will use both experiment circuits to measure the thermal boundary resistance between the superhydrophobic film and the water, as well as the thermal physical properties of the coatings, using the bi-directional 3-omega method.

References

[1] David G. Cahill and, Thermal conductivity of amorphous solids above the plateau, Phys. Rev. B. 34 (1987) 5684–5690.

[2] D.G. Cahill, Thermal conductivity measurement from 30 to 750 K: The 3ω method, Rev. Sci. Instrum. 61 (1990) 802–808.

[3] D.G. Cahill, M. Katiyar, J.R. Abelson, Thermal conductivity of alpha-Si thin films, Phys. Rev. B. 50 (1994) 6077–6082.

[4] J.H. Kim, A. Feldman, D. Novotny, Application of the three omega thermal conductivity measurement method to a film on a substrate of finite thickness, J. Appl. Phys. 86 (1999) 3959–3963.

[5] T. Borca-Tasciuc, A.R. Kumar, G. Chen, Data reduction in 3ω method for thin-film thermal conductivity determination, Rev. Sci. Instrum. 72 (2001) 2139–2147.

[6] S. Ahmed, R. Liske, T. Wunderer, M. Leonhardt, R. Ziervogel, C. Fansler, T. Grotjohn, J. Asmussen, T. Schuelke, Extending the 3ω-method to the MHz range for thermal conductivity measurements of diamond thin films, Diam. Relat. Mater. 15 (2006) 389–393.

[7] C. Dames, Measuring the Thermal Conductivity of Thin Films: 3 Omega and Related Electrothermal Methods, Annu. Rev. Heat Transf. 16 (2013) 7–49.

[8] M. Bogner, A. Hofer, G. Benstetter, H. Gruber, R.Y.Q. Fu, Differential 3ω method for measuring thermal conductivity of AIN and Si3N4 thin films, Thin Solid Films. 591 (2015) 267–270.

[9] D. Zhao, X. Qian, X. Gu, S.A. Jajja, R. Yang, Measurement Techniques for Thermal Conductivity and Interfacial Thermal Conductance of Bulk and Thin Film

Materials, J. Electron. Packag. 138 (2016) 040802.

[10] S.R. Choi, J. Kim, D. Kim, 3Ω Method To Measure Thermal Properties of Electrically Conducting Small-Volume Liquid, Rev. Sci. Instrum. 78 (2007).

[11] B.K. Park, N. Yi, J. Park, D. Kim, Note: Development of a microfabricated sensor to measure thermal conductivity of picoliter scale liquid samples, Rev. Sci. Instrum. 83 (2012) 2012–2015.

[12] S. Roy-Panzer, T. Kodama, S. Lingamneni, M.A. Panzer, M. Asheghi, K.E. Goodson, Thermal characterization and analysis of microliter liquid volumes using the three-omega method, Rev. Sci. Instrum. 86 (2015) 1–11.

[13] A. Varpula, B. Wunderle, M. Abo Ras, S. Gomès, K. Grigoras, C. Grosse, M. Prunnila, D. May, P.-O. Chapuis, Microfabricated sensor platform with through-glass vias for bidirectional 3-omega thermal characterization of solid and liquid samples, Sensors Actuators A Phys. 278 (2018) 33–42.

[14] I.K. Moon, Y.H. Jeong, S.I. Kwun, The 3ω technique for measuring dynamic specific heat and thermal conductivity of a liquid or solid, Rev. Sci. Instrum. 67 (1996) 29–35.

[15] B. Kyoo Park, N. Yi, J. Park, D. Kim, Thermal conductivity of single biological cells and relation with cell viability, Appl. Phys. Lett. 102 (2013) 1–6.

[16] B.K. Park, Y. Woo, D. Jeong, J. Park, T.Y. Choi, D.P. Simmons, J. Ha, D. Kim, Thermal conductivity of biological cells at cellular level and correlation with disease state, J. Appl. Phys. 119 (2016).

[17] S.D. Lubner, J. Choi, G. Wehmeyer, B. Waag, V. Mishra, H. Natesan, J.C. Bischof, C. Dames, Reusable bi-directional 3ω sensor to measure thermal conductivity of 100-μ m thick biological tissues, Rev. Sci. Instrum. 86 (2015) 1–13.

[18] S. Yamaguchi, T. Shiga, S. Ishioka, T. Saito, T. Kodama, J. Shiomi, Anisotropic thermal conductivity measurement of organic thin film with bidirectional 3ω method, Rev. Sci. Instrum. 92 (2021) 1–35.

[19] B.W. Olson, S. Graham, K. Chen, A practical extension of the 3ω method to multilayer structures, Rev. Sci. Instrum. 76 (2005).

[20] L.N. Acquaroli, 3-Omega Method for Thermal Properties of Thin Film Multilayers, (2018) 1–8.

[21] K. Kurabayashi, M. Asheghi, M. Touzelbaev, K.E. Goodson, Measurement of the thermal conductivity anisotropy in polyimide films, J. Microelectromechanical Syst. 8 (1999) 180–191.

[22] D.G. Cahill, H.E. Fischer, T. Klitsner, E.T. Swartz, R.O. Pohl, Thermal conductivity of thin films: Measurements and understanding, J. Vac. Sci. Technol. A Vacuum, Surfaces, Film. 7 (1989) 1259–1266.

[23] D.S. Katzer, M. Cardona, Thermal-conductivity measurements of GaAs/AlAs superlattices using a picosecond optical pump-and-probe technique, Phys. Rev. B - Condens. Matter Mater. Phys. 59 (1999) 8105–8113.

[24] J. Zhu, D. Tang, W. Wang, J. Liu, K.W. Holub, R. Yang, Ultrafast thermoreflectance techniques for measuring thermal conductivity and interface thermal conductance of thin films, J. Appl. Phys. 108 (2010).

[25] J.A. Malen, K. Baheti, T. Tong, Y. Zhao, J.A. Hudgings, A. Majumdar, Optical measurement of thermal conductivity using fiber aligned frequency domain thermoreflectance, J. Heat Transfer. 133 (2011) 1–7.

[26] T. Hänninen, Implementing the 3-Omega Technique for Thermal Conductivity Measurements, Dissertation. (2013).

[27] Jaeger J C, Carslaw H S. Conduction of heat in solids. Oxford, United Kingdom:: Clarendon P, 1959.

[28] Erdélyi A, Magnus W, Oberhettinger F, et al. Tables of integral transforms. 1954.

Chapter 3

3. Measurement of thermal boundary resistance between water and superhydrophobic surface

3.1 Introduction

Superhydrophobic surfaces have unique properties useful for a wide variety of industries, such as self-cleaning, waterproofing, anti-icing, and fluid drag reduction [1]. In heat transfer applications, the superhydrophobicity of the wall surface, which affects nucleation, wetting dynamics, and interphase heat transfer, results in interesting/useful properties in phase change heat transfer. Tiny superhydrophobic spots on the wall acting as artificial nucleation sites are useful to enhance boiling bubble nucleation [2]. The superbiphilic heat transfer surfaces strongly enhance boiling heat transfer[3]. Condensate droplets jump off the superhydrophobic heat transfer surface after the coalescence of droplets, and this droplet jumping phenomenon results in the enhancement of the condensation heat transfer [4]. Superhydrophobic surfaces show excellent anti-freezing capability due to the anti-wetting surface property and the large thermal boundary resistance between the liquid and wall surface [5]. In phase-change heat transfer phenomena on superhydrophobic surfaces, the thermal boundary resistance, due to the thin air layer on the surface, is an important factor that determines the overall heat and

mass transfer. Because of slip flow on the superhydrophobic surface, the superhydrophobicity results in a reduction of pressure drop in liquid flow in a small channel [6-8]. Determination of the thermal boundary resistance between the surface and the liquid is important for the optimum design of the microchannel heat exchanger with superhydrophobic inner surfaces, which effectively reduces pressure loss while suppressing heat transfer degradation [9, 10].

The thermal boundary resistance between two solids can be measured by the cut-bar method, the 3-omega method, the laser flash method, and the thermoreflectance method [11]. However, there are still difficulties in the measurements of thermal boundary resistance between the solid-liquid interface, considering the fluidity, vaporability, and low thermal conductivity of the liquid. Yuan et al. [12] used the cut-bar method to measure the thermal boundary resistance between fluids(silicon oil and thermal grease) and an aluminum wall surface with a submicron roughness. However, this method is difficult to apply to fluids such as water, having higher fluidity and vapor pressure than the fluids they used. The time-domain thermoreflectance (TDTR) is a powerful method to explore the nanoscale heat conduction mechanisms across the solid-liquid interface [13]. Some groups have discussed the relationship between interfacial resistance and surface wettability (contact angle) [14, 15]. The TDTR with a large periodic-laser heating frequency has a high sensitivity for small thermal boundary resistance in the order of around 10^{-8} [(K・m^2)/W] [16, 17] and is considered to be not suitable for the measurement of thermal boundary resistance due to the air layer on the superhydrophobic surface, which has value in the order of 10^{-6} - 10^{-5} [(K・m^2)/W]. Thus, there is no direct method for measuring the thermal boundary resistance due to the air layer between solid and

liquid.

Based on the bi-directional and differential 3-omega method, we propose a simple method for calculating the thermal boundary resistance at the solid-liquid interface when an air layer is present. When measuring the thermophysical characteristics of solids, the general one-sided 3-omega method is utilized [18, 19]. The differential 3-omega method is utilized in order to evaluate the thermal conductivity of a thin film on the substrate while the film is being heated by a thin film heater line [20, 21]. The thermophysical properties of the sample are measured using the bi-directional method while the sample is placed above the heater line on the substrate. This method was used for fluid [22-24] and bio [25-28] samples. In this chapter, we developed differential bi-directional 3 omega method, which is a combination of the differential and bi-directional methods, to measure the thermal boundary resistance between the solid and the liquid.

3.2 Principle of thermal boundary resistance measurement

In the 3-omega method, a sinusoidal current with an angular frequency of 1ω and an amplitude of I_0 was supplied to a thin film-heater line periodically. Due to Joule heating at an angular frequency of 2ω, the amplitude of the in-phase temperature oscillation with respect to the Joule heating ($\Delta T_{2\omega}$) can be obtained from the third harmonic voltage ($V_{3\omega}$) included in the voltage drop across the heater.

$$\Delta T_{2\omega} = \frac{2V_{3\omega}}{I_0 R_0 \beta} \tag{3.1}$$

where R_0 is the electrical resistance of the heater without heating, and β is the temperature coefficient of resistance (TCR) of the heater. When the heating frequency is small, and the thermal penetration depth $\lambda = (\alpha/2\omega)^{1/2}$ is larger than the five times half-width of the heater (b), the thermal resistance ($R_{1\text{-}sided}$), which is the real part of the complex thermal

transfer function [26] is expressed as

$$R_{1-sided} = \frac{\Delta T_{2\omega}}{P} = -\frac{1}{2\pi L k_1}\left[\ln(2\omega) + \ln\left(\frac{b^2}{\alpha_1}\right) + \frac{3}{2} - \gamma\right] \tag{3.2}$$

where P is the amplitude of the Joule heating, L is the length of the heater, k_1 is the thermal conductivity of the substrate material, α_1 is the thermal diffusivity of the substrate material, and γ is the Euler-Mascheroni constant. The thermal conductivity of the substrate k_1 can be determined from the slope of the real component of $\Delta T_{2\omega}$ plotted against $\ln(2\omega)$ at a certain P.

$$k_1 = -\frac{1}{2\pi L \dfrac{\partial R}{\partial \ln(2\omega)}} = -\frac{1}{2\pi L \dfrac{\partial(\Delta T_{2\omega}/P)}{\partial \ln(2\omega)}} \tag{3.3}$$

The thermal resistance R_f of a thin film target with a known thickness δ_f ($<< \lambda$) inserted between the heater line and the substrate can be determined by measuring the increase in $\Delta T_{2\omega}$ caused by the addition of the target ΔT_f at a certain power P. The thin film's thermal conductivity k_f can be calculated from the measured thermal resistance R_f. This method is known as the differential 3-omega method.

$$R_f = \frac{\Delta T_f}{P} = \frac{\delta_f}{2bLk_f} \tag{3.4}$$

In the general one-sided 3-omega method explained above (Fig. 3.1(a)), the heat flow is in one direction toward the substrate. However, in the bi-directional 3-omega method, there are two heat paths in the upper and lower directions of the heater. Based on the boundary mismatch assumption [26], the measured thermal resistance ($R_{2\text{-}sided}$) (Fig. 3.1 (b)-(d)) can be expressed as the total resistance of two parallel resistances (upper side $R_{\uparrow}$ and bottom side $R_{\downarrow}$), implying that the total thermal conductance equals the sum of two conductance on both sides. Consequently, a straightforward sum of the thermal

conductivities of the materials on the upper and bottom sides ($k_1 + k_2$) can be obtained from the slope of the total thermal resistance to $\ln(2\omega)$ at a certain P.

$$\frac{1}{R_{2-sided}} = \frac{1}{R_{\downarrow}} + \frac{1}{R_{\uparrow}} \tag{3.5}$$

$$\frac{\partial R_{2-sided}}{\partial \ln(2\omega)} = \frac{\partial(\Delta T_{2\omega}/P)}{\partial \ln(2\omega)} = -\frac{1}{2\pi L(k_1 + k_2)} \tag{3.6}$$

The thermal conductivity of the target over the heater conductivity k_2 can be obtained from the difference between $k_1 + k_2$ and k_1 by measuring the thermal conductivity of the substrate k_1 using the one-sided 3-omega method in advance (Fig. 3.1 (a)).

We combined the differential 3-omega method and bi-directional 3-omega method to determine the thermal boundary resistance between the water and superhydrophobic coating with an air layer in between. First, the thermal resistance of the substrate (bottom side) R_{dry} is measured in the dry-state by the one-sided 3-omega method (Fig. 3.1 (a)).

$$\frac{1}{R_{dry}} = \frac{1}{\frac{\Delta T_{2\omega\_dry}}{P}} = \frac{1}{R_{\downarrow}} \tag{3.7}$$

As shown in Fig. 3.1 (b), the water is poured into the small chamber while a thin air layer forms on the superhydrophobic substrate. The total thermal resistance measured in this step (R_{al}) is comprised of thermal resistances of the bottom side ($R_{\downarrow}$) and upper side ($R_{\uparrow}$), which are connected in parallel. In addition, the thermal resistance of the upper side corresponds to the sum of thermal resistances of the water (R_w), the SiO_2 insulation layer (R_i), and the superhydrophobic coating (R_c), as well as the thermal boundary resistance (R_b) (Figs. 3.1 (b) and (c))

$$\frac{1}{R_{al}} = \frac{1}{\frac{\Delta T_{2\omega\_al}}{P}} = \frac{1}{R_{\downarrow}} + \frac{1}{R_{\uparrow}} = \frac{1}{R_{dry}} + \frac{1}{R_w + R_b + R_i + R_c} \tag{3.8}$$

To extract the thermal boundary resistance (R_b) following the idea of the differential

method, we should hydrophilize the surface to obtain the reference state without the air layer (thermal boundary resistance), as shown in Fig. 3.1 (d). To achieve the reference state, the wettability of the surface was altered using plasma treatment. The thermal boundary resistance (R_b) is defined as the additional thermal resistance due to the superhydrophobicity. If it is necessary to measure the overall thermal resistance of a film layer consisting of both an air layer and a solid superhydrophobic coating, the thermal resistance obtained prior to applying the superhydrophobic coating can be used as a reference.

$$\frac{1}{R_{wet}} = \frac{1}{\frac{\Delta T_{2\omega\_wet}}{P}} = \frac{1}{R_{\downarrow}} + \frac{1}{R'_{\uparrow}} = \frac{1}{R_{dry}} + \frac{1}{R_w + R_i + R_c} \tag{3.9}$$

By following the above three steps, we can obtain the thermal boundary resistance (R_b). Thermal resistances required to derive the thermal boundary resistance can be obtained from the temperature increase against a power $\Delta T_{2\omega} / P$ as in Eqs. (3.7)-(3.9). If the temperature increase is small, the thermal resistance is unaffected by the Joule heating rate P. At selected heating frequencies, the amplitude of the temperature oscillation $\Delta T_{2\omega}$ is measured by varying the supplied power P, and the thermal resistance can be derived from the slope of the approximate straight lines of plots $\partial \Delta T_{2\omega} / \partial P$ to obtain higher reliability, as shown in Fig. 3.1 (f).

$$R_b = \frac{1}{\frac{1}{R_{al}} - \frac{1}{R_{dry}}} - \frac{1}{\frac{1}{R_{wet}} - \frac{1}{R_{dry}}} \tag{3.10}$$

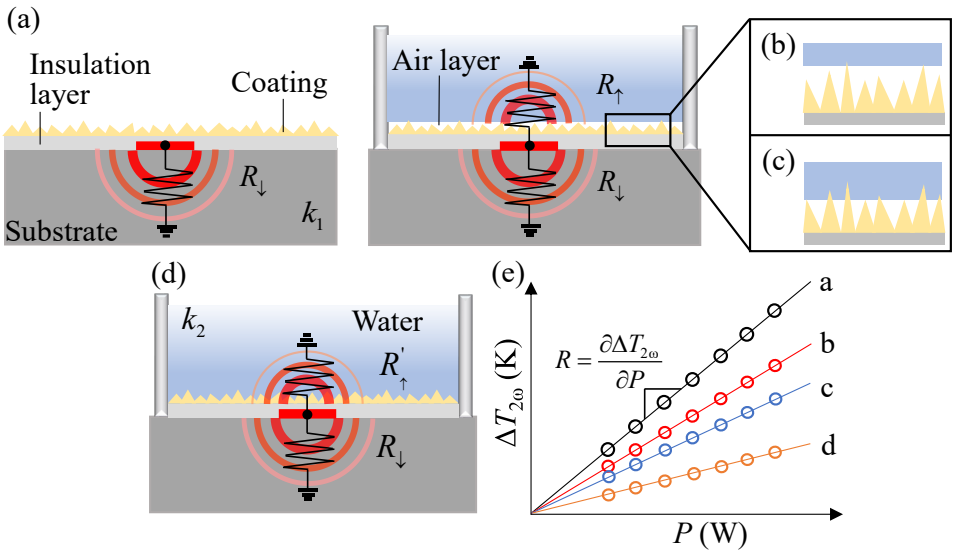

Fig. 3.1. The measurement of the thermal boundary layer on the superhydrophobic surface using the bi-directional differential 3-omega. (a) Dry-state measurement of the thermal resistance on the substrate side. Bi-directional measurement underwater (b) before and (c) after the air layer thickness reduction. (d) After the plasma treatment, measurement in the reference state without air layer. (f) Thermal resistances are derived from the slope of the $\Delta T_{2\omega}$ against Joule heating P.

3.3 Experimental setup and procedure

Fig. 3.2 depicts the sputtered aluminum heater line with dimensions of 160 nm in thickness, 30 μm in width, and 6 mm in length on the 3.3 mm thick borosilicate glass substrate. On the heater, the SiO_2 insulating layer about 200 nm thick was sputtered. The superhydrophobic structure was formed by spin-coating the commercially available coating agent (Glaco Mirror Coat Zero, Soft 99) on the insulating layer, followed by 20 minutes of hotplate heating at 150 °C. The Glaco is a well-known superhydrophobic coating that has been utilized in various research fields [29-31]. Fig. 3.3 shows the surface

topology of the formed Glaco coating observed by an atomic force microscope (AFM). The scanning region was 50 μm × 50 μm. The arithmetic mean roughness (*Ra*), the ten-point mean roughness (*Rc*), and the maximum peak (*Rz*) were, respectively, 48 nm, 201 nm, and 385 nm. The Glaco coating and insulation layer are much thinner than the width of the heater, and consequently, the edge effects [21] that cause the underestimating of thermal resistances are negligible. The temperature-dependent electrical resistance of the heater is calibrated in order to determine the TCR of the heater inside the convection oven with a constant temperature. As shown in Fig. 3.4, a small test chamber was created by sandwiching a glass cell with a 10 mm square cross-section between the glass substrate mounted on the jig and the flat plate on the top. A thin silicone rubber sheet was installed between the glass cell and the glass substrate to prevent water leakage. The four-probe connection was employed to lower the effect of electrical resistance of contact between metal probes and pads.

Fig. 3.4 depicts a typical analog electrical circuit used to drive the heater and condition the signals in the 3-omega measurements. Using the voltage-to-current converter, the sinusoidal voltage output from a function generator is converted into a sinusoidal current, which is then supplied to the heater line. The current was measured from the voltage drop across the 100 Ω high-precision resistor connected in series with the heater line. The amplitude of 1ω component contained in the signal of the heater line was reduced to the same level as that of the 3ω components using the last differential amplifier. This reduced 1ω component allows for a narrower voltage measuring range (higher resolution). In the tested heating frequency range, the phase delay and frequency dependence of the attenuation ratio (*K*) of the resistive voltage divider utilized to condition the voltage drop across the high-precision resistor is negligible. The signal output from the differential

amplifier is measured using a data acquisition device (PXIe-4303, National Instruments) at a sampling frequency of 50kHz. The lock-in measurement of the amplitude of the 3ω component ($V_{3\omega}$) was conducted on the self-made LabVIEW program.

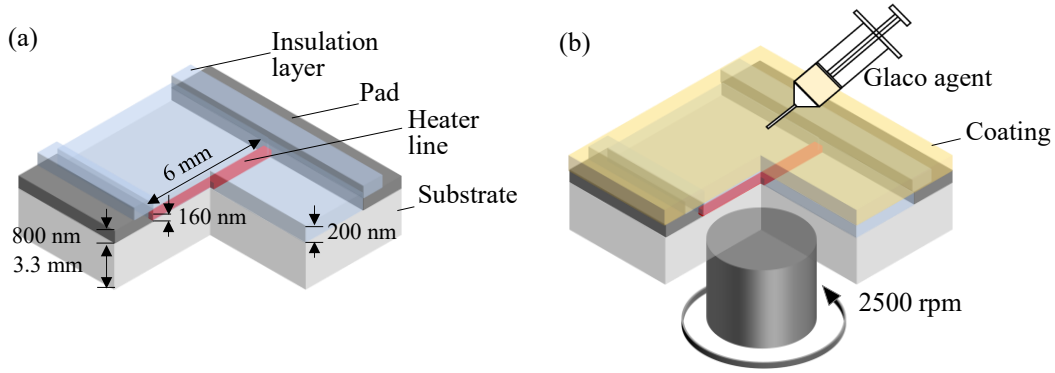

Fig. 3.2. (a) The sputtered aluminum microheater on the borosilicate glass substrate for the 3ω measurement, and (b) spin-coating of Glaco agent on the substrate.

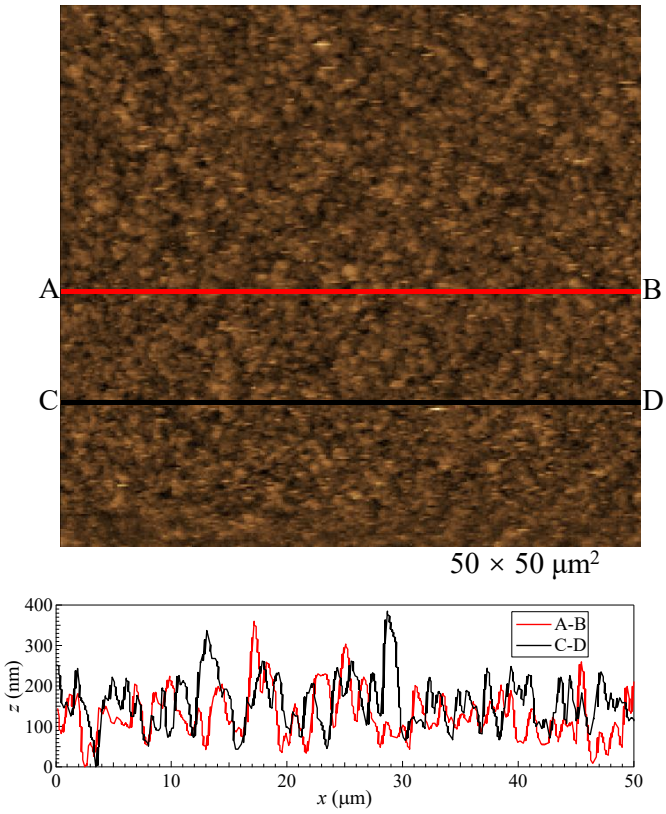

Fig. 3.3. The surface topographic image of coated Glaco film was observed using AFM.

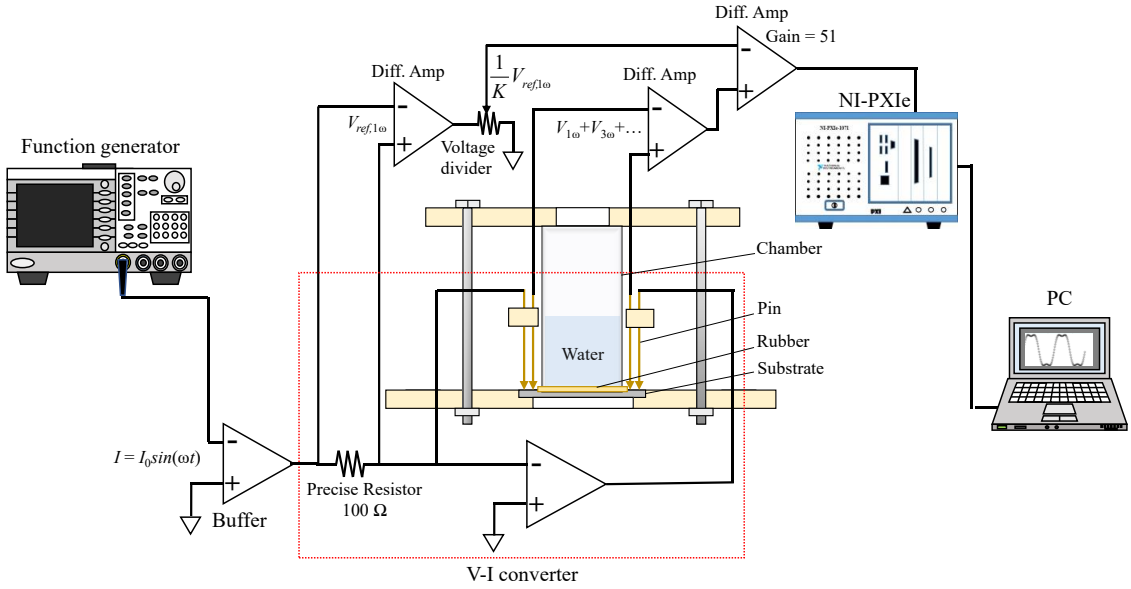

Fig. 3.4. The electrical circuit with the test cell.

Here is the experimental procedure. First, (1) the superhydrophobic film was formed by spin-coating Glaco solution on the borosilicate glass substrate. (2) the thermal resistance of the substrate side (R_{dry}) was measured at each heating frequency (Fig. 3.1 (a) and Eq. (3.7)) in the dry-state. (3) water was poured into the small test chamber to get an air layer on the superhydrophobic surface, and the uniform metallic luster that indicates the formation of an air layer formation appears on the surface underwater. The overall thermal resistance (R_{al}), containing the thermal boundary resistance, was measured in this step (Fig. 3.1 (b) and Eq. (3.8)). (4) by the process of degassing water in a vacuum chamber, the thickness of the air layer was reduced to determine the air layer thickness-dependent thermal boundary resistance. The small test chamber containing the water was put inside a vacuum chamber after the measurement of step (3), and the water was degassed for approximately one minute at a pressure of about 10^2 Pa. As shown in Fig. 3.5, film boiling occurred on the superhydrophobic surface by water evaporation during the degassing process, and a portion of the air in the air layer was removed during the

cyclic detachment of large bubbles from the wall. Even after the degassing treatment, the surface maintained its metallic luster, indicating that an air layer covered the surface, as shown in Fig. 3.5 (right). (5) the thermal resistance was determined with the reducing air layer thickness (Fig. 3.1 (c)). (6) the water was drained from the test chamber, and the surface wettability was changed from superhydrophobic to superhydrophilic through the plasma treatment in the vacuum, which is a known approach for changing the wettability of Glaco coating without change in surface morphology [29]. This wettability change by plasma treatment is applicable to a variety of micro/nanostructured superhydrophobic surfaces. After pouring the water into the chamber, the surface loses its metallic luster, which is evidence of solid-liquid contact on the Glaco coating, and the measured static contact angle was less than 10°. Finally, the thermal resistance under the condition of full solid-liquid contact, (R_{wet}), was measured (Fig. 3.1 (d) and Eq. (3.9)).

In the thermal resistance measurement processes, the Rayleigh number [23] was less than 1, preventing natural convection. The surface wettability of the substrate under the different conditions is shown in Fig. 6. The heating frequency range was varied from 0.4Hz to 2.98Hz to ensure that the thermal penetration depth was smaller than the substrate thickness and larger than the heater line width [21].

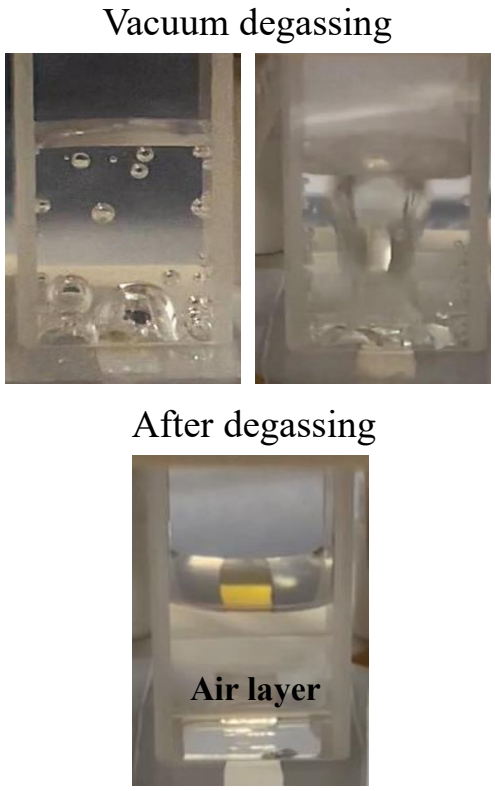

Fig. 3.5. Reduction of air layer thickness through the water degassing under vacuum. Air bubbles appear on the walls (left). Large bubbles detach from the superhydrophobic surface as in the case of film boiling (center). Even after the degassing process, the surface still retains metallic luster, which means there exists an air layer on the superhydrophobic surface (right).

3.4 Results and discussion

Fig. 3.6 shows the results of the 3-omega measurements, where the measured thermal resistance $\Delta T_{2\omega}/P$ is plotted against ln(2ω) for four cases. First is the dry-state (a), the second is with the air layer underwater (b), the third is with an air layer underwater after reducing air layer thickness (c), and the fourth is the fully wetting state after plasma treatment (d). The amplitude of sinusoidal Joule heating rate P was 3.8 milliwatts, which

is small to inhibit natural convection. The measured dry-state thermal conductivity of the borosilicate glass substrate was 1.22 [W/(m·K)] (a). Data for three underwater conditions (b)-(d) parallel aligns, and the shifts of (b) and (c) from (d) are due to the thermal boundary resistance (air layer) between the water and the wall surface. Underwater, the sum of the thermal conductivities of water and substrate can be determined using the slope in Eq. (3.6), and the thermal conductivity of water can be calculated by subtracting the substrate thermal conductivity measured in advance from the summation value. The relatively straight lines for three underwater conditions are nearly parallel, and the obtained thermal conductivities were (b) 0.61, (c) 0.60, and (d) 0.60 [W/(m·K)], which are in good agreement with the reference value of 0.60 [W/(m·K)] at 23 °C [32]. Since the thermal conductivity of water could be measured even with the air layer on the surface, it can be concluded that the thermal boundary resistance due to the air layer has no effect on the measurement of the thermal resistance of the water in the tested frequency range. The input power was constant in this measurement, and next, the temperature oscillation ($\Delta T_{2\omega}$) was measured by changing the heating power P at a certain frequency, as shown in Fig. 3.1 (f), to measure thermal resistances precisely.

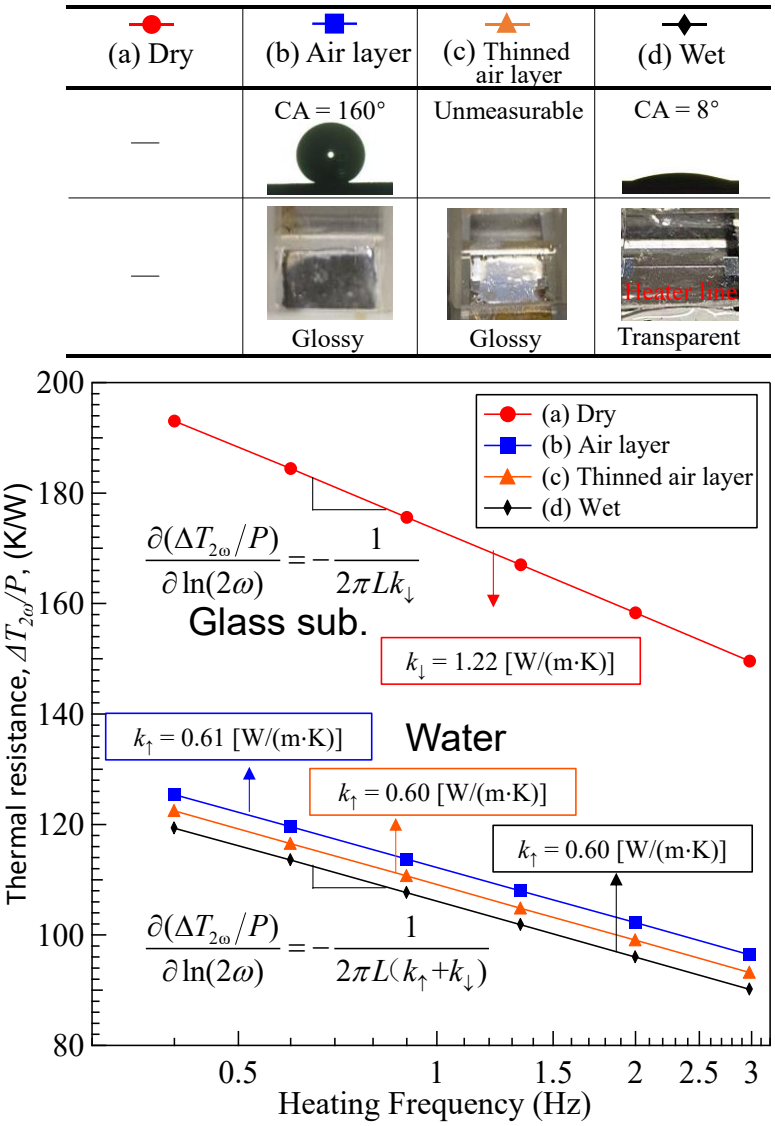

Fig. 3.6. Measured thermal resistances required for the derivation of the thermal boundary resistance.

Fig. 3.7 shows the relationship between the amplitude of the temperature oscillation ($\Delta T_{2\omega}$) and the amplitude of the sinusoidal Joule heating rate P for four conditions: (a) - (d). The data for three heating frequencies of 0.40Hz, 1.34Hz, and 2.98Hz are shown in this figure. The data are linear with respect to the power and toward the origin, indicating that the thermal resistance can be determined from the slope. Condition (a), where the

heat is transferred unidirectionally toward the substrate, shows the largest total thermal resistance (slope). The thermal boundary resistance between water and solid was created by the air layer. Consequently, conditions (b) and (c) with an air layer show large total thermal resistance compared to the condition (d) without an air layer (wetting condition). The thermal penetration depth increases with decreasing heating frequency, and therefore, the data at the lower frequency shows a larger slope (thermal resistance). The measurement of thermal resistances in various conditions (R_{dry}, R_{al}, R_{wet}) required to derive the thermal boundary resistance (R_b) using Eq. (3.10) has been done.

The thermal boundary resistance shown in Fig. 3.8 was calculated by substituting thermal resistances, R_{dry}, R_{al}, and R_{wet}, into Eq. (3.10). By multiplying the results by the area of the heater top surface $2bL$, and the resultant thermal resistance was converted into the thermal resistance per unit area, also known as thermal resistivity. The penetration depth in water shown in the top horizontal axis corresponds to the heating frequency in the lower horizontal axis. The thermal boundary resistances are 7.5×10^{-6}, and 3.5×10^{-6} [$(K \cdot m^2)/W$] before and after degassing, respectively, and are independent of the penetration depth in water (heating frequency). The degassing of water reduced the thickness of the air layer, and therefore the thermal resistance is decreased by half after degassing operation. In order to analyze the relation between the thermal boundary resistance and surface structure, the thermal boundary resistances were subsequently converted to the equivalent thickness of air layer δ_{eq}. The partial pressure of the water vapor is small (about 1/35 of the total pressure inside the air layer at 23ºC). Therefore, the effective thermal conductivity of the air layer can be regarded as the thermal conductivity of air k_{air}.

$$\delta_{eq} = R_b \times 2bLk_{air} \tag{3.11}$$

The calculated equivalent air layer thickness was 0.20 μm and 0.09 μm before and after degassing, respectively. Following the observations of Poetes et al. [33], who examined the wetting states between the surface and liquid at varied air layer thicknesses using a confocal microscope, the liquid-gas structure on the wall during thermal resistance measurements is explored. As shown in Fig. 3.8 (Right), the air layer structures expected from measurement results in which the gas-liquid interface was drawn by hand on the surface topology obtained by AFM. The equivalent thickness of 0.20 μm is near the difference between the maximum height and average height (centerline) in the surface topology, indicating that the air layer uniformly covered the wall surface and the only sparse high surface protrusions touch the water, as shown in Fig. 3.8. After the degassing of water in the vacuum, the drop in the thickness of the air layer acting as the thermal insulator led to the decrease in thermal boundary resistance. In both cases (before and after air layer thickness reduction), the air layer covered an area that was larger than the water on the wall surface, and the air layer was found to interfere with the heat transfer between the solid and the water. The resolution of boundary resistance measurement in our experimental setup was evaluated to be approximately 1×10^{-7} [(K・m^2)/W] based on the standard deviation of measurement results. Therefore, this method can be used to measure thermal boundary resistance that is at least an order of magnitude smaller than the sample in this study. This study demonstrated that this method gives the thermal boundary resistance on the superhydrophobic surface, which is an important parameter in the heat transfer prediction models for a variety of heat transfer phenomena on superhydrophobic surfaces.

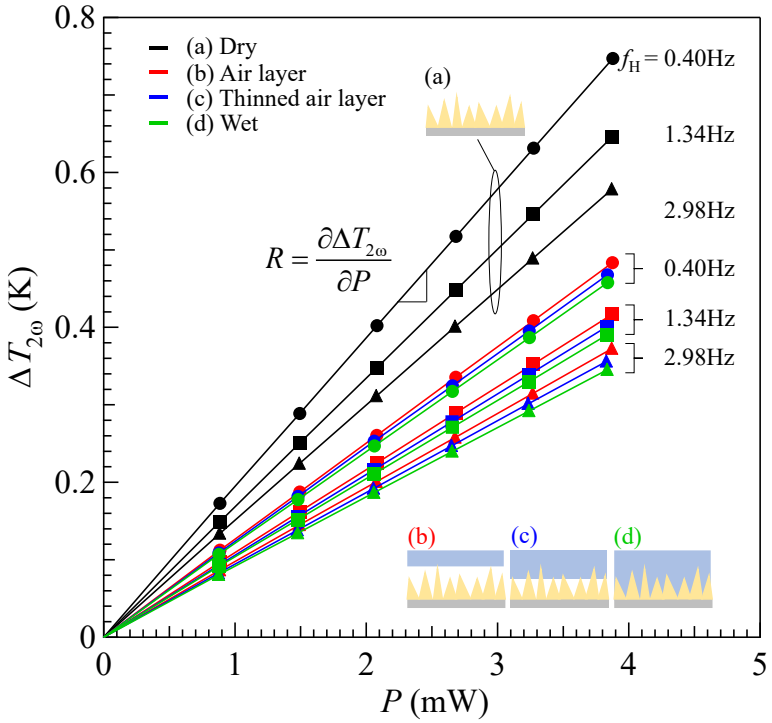

Fig. 3.7. Temperature rise plotted against heating power. The slopes correspond to the thermal resistances.

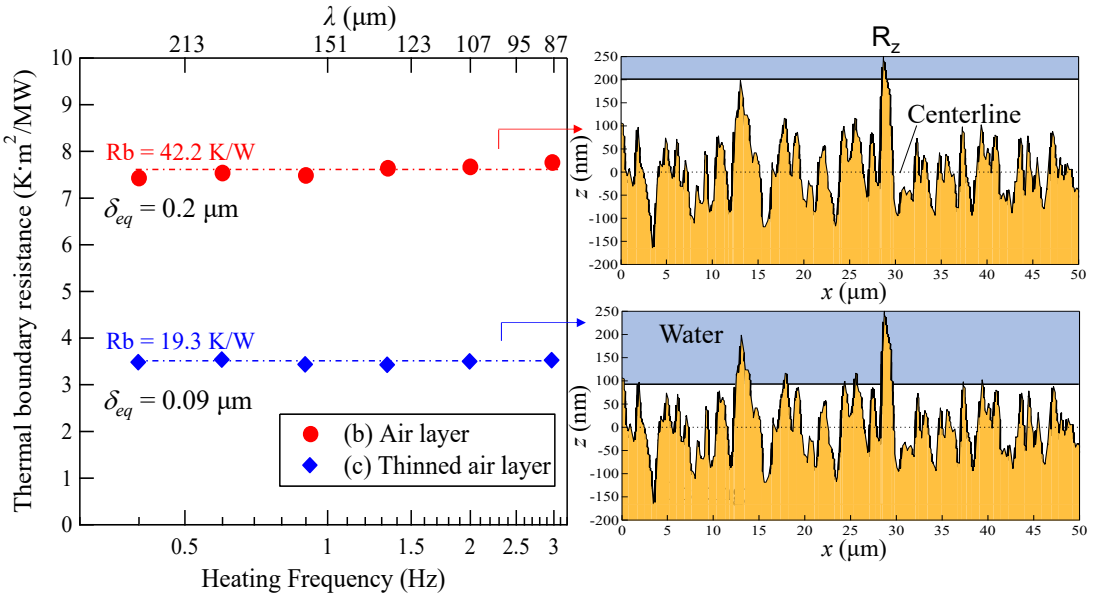

Fig. 3.8. The thermal boundary resistances between water and superhydrophobic surfaces

before and after the reduction of the air layer thickness (left). The schematic drawing of the gas-liquid structure on the Glaco coating in which the surface shape of the coating is an actual surface topographic image obtained using the AFM (right).

3.5 Conclusions

Using the bi-directional differential 3-omega method, we demonstrated the first direct measurement of thermal boundary resistance between water and micro/nanostructured superhydrophobic surfaces with a thin air layer in between. In this study, the superhydrophobic structure was composed of Glaco coating, a commercial coating agent utilized in a variety of research domains. The plasma treatment was utilized to obtain the reference state without the thermal boundary resistance due to the air layer, which is required for the differential 3-omega measurements. The measured thermal boundary resistance was 7.5×10^{-6} [$(K\cdot m^2)/W$], and the equivalent air layer thickness was 0.2 μm. The equivalent thickness was consistent with the surface structure of the prepared Glaco coating observed by AFM, indicating that the air layer covered a large area of the wall surface and dominated the thermal boundary resistance. The reduction of the thermal boundary resistance following the reduction of the air layer thickness by the vacuum degassing treatment was also observed. This study's method for measuring the thermal boundary resistance of a superhydrophobic structure is useful for the thermal design of various thermal devices with a superhydrophobic surface.

References

[1] P. Zhang, F. Y. Lv, A review of the recent advances in superhydrophobic surfaces

and the emerging energy-related applications, Energy 82 (2015) 1068-1087.

[2] H. He, K. Furusato, M. Yamada, B. Shen, S. Hidaka, M. Kohno, K. Takahashi, Y. Takata, Efficiency enhancement of a loop thermosyphon on a mixed-wettability evaporator surface, Applied Thermal Engineering 123 (2017) 1245-1254.

[3] A. R. Betz, J. Jenkins, D. Attinger, Boiling heat transfer on superhydrophilic, superhydrophobic, and superbiphilic surfaces, International Journal of Heat and Mass Transfer 57(2) (2013) 733-741.

[4] N. Miljkovic, R. Enright, Y. Nam, K. Lopez, N. Dou, J. Sack, E. N. Wang, Jumping-droplet-enhanced condensation on scalable superhydrophobic nanostructured surfaces, Nano letters 13(1) (2013) 179-187.

[5] L. Mishchenko, B. Hatton, V. Bahadur, J. A. Taylor, T. Krupenkin, J. Aizenberg, Design of ice-free nanostructured surfaces based on repulsion of impacting water droplets, ACS nano 4(12) (2010) 7699-7707.

[6] R. Truesdell, A. Mammoli, P. Vorobieff, F. van Swol, C. J. Brinker, Drag reduction on a patterned superhydrophobic surface, Physical review letters 97(4) (2006) 044504.

[7] R. J. Daniello, N. E. Waterhouse, J. P. Rothstein, Drag reduction in turbulent flows over superhydrophobic surfaces, Physics of Fluids 21(8) (2009) 085103.

[8] G. Nagayama, P. Cheng, Effects of interface wettability on microscale flow by molecular dynamics simulation, International Journal of Heat and Mass Transfer 47(3) (2004) 501-513.

[9] H. Ermagan, R. Rafee, Effect of pumping power on the thermal design of converging microchannels with superhydrophobic walls, International Journal of Thermal Sciences 132 (2018) 104-116.

[10] H. Ermagan, R. Rafee, Geometric optimization of an enhanced microchannel heat sink with superhydrophobic walls, Applied Thermal Engineering 130 (2018) 384-394.

[11] Y. Xian, P. Zhang, S. Zhai, P. Yuan, D. Yang, Experimental characterization methods for thermal contact resistance: A review, Applied Thermal Engineering 130 (2018) 1530-1548.

[12] C. Yuan, B. Duan, L. Li, B. Shang, X. Luo, An improved model for predicting thermal contact resistance at liquid–solid interface, International Journal of Heat and Mass Transfer 80 (2015) 398-406.

[13] H. Harikrishna, W. A. Ducker, S. T. Huxtable, The influence of interface bonding on thermal transport through solid–liquid interfaces, Applied Physics Letters 102(25) (2013) 251606.

[14] Z. Ge, D. G. Cahill, P. V. Braun, Thermal conductance of hydrophilic and hydrophobic interfaces, Physical review letters 96(18) (2006) 186101.

[15] J. A. Tomko, D. H. Olson, A. Giri, J. T. Gaskins, B. F. Donovan, S. M. O'Malley, P. E. Hopkins, Nanoscale wetting and energy transmission at solid/liquid interfaces, Langmuir 35(6) (2019) 2106-2114.

[16] P. E. Hopkins, M. Baraket, E. V. Barnat, T. E. Beechem, S. P. Kearney, J. C. Duda, S. G. Walton, Manipulating thermal conductance at metal–graphene contacts via chemical functionalization, Nano letters 12(2) (2012) 590-595.

[17] Y. K. Koh, M. H. Bae, D. G. Cahill, E. Pop, Heat conduction across monolayer and few-layer graphenes, Nano letters 10(11) (2010) 4363-4368.

[18] D. G. Cahill, Thermal conductivity measurement from 30 to 750 K: the 3ω method, Review of scientific instruments 61(2) (1990) 802-808.

[19] C. Dames, G. Chen, 1ω, 2ω, and 3ω methods for measurements of thermal properties, Review of Scientific Instruments 76(12) (2005) 124902.

[20] D. G. Cahill, M. Katiyar, J. R. Abelson, Thermal conductivity of α-Si: H thin films, Physical Review B 50(9) (1994) 6077.

[21] C. Dames, Measuring the thermal conductivity of thin films: 3 omega and related electrothermal methods, Annual Review of Heat Transfer 16 2013.

[22] I. K. Moon, Y. H. Jeong, S. I. Kwun, The 3ω technique for measuring dynamic specific heat and thermal conductivity of a liquid or solid, Review of scientific instruments 67(1) (1996) 29-35.

[23] S. R. Choi, J. Kim, D. Kim, 3ω method to measure thermal properties of electrically conducting small-volume liquid, Review of scientific instruments 78(8) (2007) 084902.

[24] D. W. Oh, A. Jain, J. K. Eaton, K. E. Goodson, J. S. Lee, Thermal conductivity measurement and sedimentation detection of aluminum oxide nanofluids by using the 3ω method, International Journal of Heat and Fluid Flow 29(5) (2008) 1456-1461.

[25] B. Kyoo Park, N. Yi, J. Park, D. Kim, Thermal conductivity of single biological cells and relation with cell viability, Applied Physics Letters 102(20) (2013) 203702.

[26] S. D. Lubner, J. Choi, G. Wehmeyer, B. Waag, V. Mishra, H. Natesan, C. Dames, Reusable bi-directional 3ω sensor to measure thermal conductivity of 100-μm thick biological tissues, Review of Scientific Instruments 86(1) (2015) 014905.

[27] B. K. Park, Y. Woo, D. Jeong, J. Park, T. Y. Choi, D. P. Simmons, D. Kim, Thermal conductivity of biological cells at cellular level and correlation with disease state,

Journal of Applied Physics 119(22) (2016) 224701.

[28] L. Tian, Y. Li, R. C. Webb, S. Krishnan, Z. Bian, J. Song, J. A. Rogers, Flexible and stretchable 3ω sensors for thermal characterization of human skin, Advanced Functional Materials 27(26) (2017) 1701282.

[29] I. U. Vakarelski, N. A. Patankar, J. O. Marston, D. Y. Chan, S. T. Thoroddsen, Stabilization of Leidenfrost vapor layer by textured superhydrophobic surfaces, Nature 489(7415) (2012) 274-277.

[30] F. Villa, Effect of Wettability on Phase Change Phenomena, Ph.D. thesis, University of Bergamo, Italy, 2017.

[31] C. Lv, P. Hao, Z. Yao, F. Niu, Departure of condensation droplets on superhydrophobic surfaces, Langmuir 31(8) (2015) 2414-2420.

[32] M. L. Ramires, C. A. Nieto de Castro, Y. Nagasaka, A. Nagashima, M. J. Assael, W. A. Wakeham, Standard reference data for the thermal conductivity of water, Journal of Physical and Chemical Reference Data 24(3) (1995) 1377-1381.

[33] R. Poetes, K. Holtzmann, K. Franze, U. Steiner, Metastable underwater superhydrophobicity, Physical review letters 105(16) (2010) 166104.

Chapter 4

4. Thermal conductivity measurement of the printed thermoelectric materials

4.1 Introduction

Microfabrication technology based on photolithography and vapor deposition makes it difficult to produce flexible sensors and electronics over large areas at a low cost [1, 2]. However, printing technology enables the fabrication of flexible sensors and electronics at low cost over large areas, and in thermoelectric (TE) conversion, where heat is transferred to electricity and vice versa, printing technology can enhance the scalability and production costs of devices [3]. As one of the components of the figure of merit *ZT*, the high-throughput measurement of thermal conductivity will accelerate material development and thermal design of printed thermoelectric devices. Printed thermoelectric films are typically composed of organic-inorganic composites of polymer binder and thermoelectric material particles (e.g., Bi_2Te_3-based compounds and polyimide [4] or PEDOT: PSS [5], Sb_2Te_3 based compounds and PEDOT: PSS [6]). The surface roughness of the films is comparable to the TE particle size [4-7]. This surface roughness makes it difficult to apply the differential 3-omega method [8, 9] and thermoreflectance method [10-12], which are typical methods of measurement for thin films deposited by, e.g., physical and chemical vapor deposition (PVD and CVD), for thermal conductivity

measurement.

The bi-directional 3-omega method, on the other hand, which can measure the thermophysical properties of a target placed on a thin-film heater formed on a substrate, can be employed independently of the surface roughness of the sample. This method has been demonstrated to be effective for determining the thermophysical properties of liquids [13-16] and bio-materials [17-20]. If the sample is sufficiently thicker than the heater line width, the thermal conductivity can be easily determined from the slope of the temperature amplitude with respect to the heating frequency. This method is referred to as the slope method [14, 15, 17-20]. However, it is challenging to fabricate a heater with a sufficiently narrow line width for a thin coated film and with adequate durability for printing and subsequent heat treatment using laboratory-level microfabrication techniques. Consequently, the thermophysical property measurement based on the bi-directional 3-omega method for a relatively thin printed film is still difficult.

In this study, we present a new method based on the bi-directional 3-omega method that can measure the thermophysical properties of printed films, not only thermoelectric materials, by employing two different line width heaters with different sensitivities to thermal conductivity and volumetric specific heat. In this method, the thermal effusivity of a sample is first obtained using a wider heater. Next, the thermal conductivity is determined by fitting the analytical solution with the thermal effusivity measured in advance to the temperature oscillation obtained with a narrow heater. For the measurement samples, first, the thermal conductivity and thermal effusivity of glycerin and SU-8 resin, for which thermophysical properties have been reported, were measured to verify the validity of the method. Then, the thermal conductivity of printed composite TE material composed of Bi_2Te_3-based thermoelectric material and polyimide coated

composites, was measured.

4.2 Measurement principle

In the bi-directional 3-omega method, the temperature oscillation of the heater $\Delta T_{2\omega}$ considering the known thermal resistance of the insulation layer on the heater, $R_{\text{insl.}}$, is calculated by Equation (4.1) below

$$\Delta T_{2\omega} = -\frac{P_0}{\pi L}\int_0^{\infty}\frac{\sin^2(\eta b)}{(\eta b)^2}\frac{1+R_{\text{insl.}}k_{\uparrow}\sqrt{\eta^2+q_{\uparrow}^2}}{k_{\downarrow}\sqrt{\eta^2+q_{\downarrow}^2}+k_{\uparrow}\sqrt{\eta^2+q_{\uparrow}^2}+R_{\text{insl.}}k_{\downarrow}k_{\uparrow}\sqrt{\eta^2+q_{\downarrow}^2}\sqrt{\eta^2+q_{\uparrow}^2}}d\eta \tag{4.1}$$

$$q_j = \sqrt{\frac{i2\omega}{\alpha_j}} = \sqrt{\frac{i2\omega(\rho c)_j}{k_j}} = \sqrt{\frac{i2\omega E_j^2}{k_j^2}} \tag{4.2}$$

where P_0 is the RMS AC power, L is the length of the heater, b is half width of the heater, k is the thermal conductivity of the substrate, η is the Fourier transform variable, q is the wavenumber of the thermal wave, α is the thermal diffusivity of the substrate, ω is the angular frequency, ρc is the volumetric heat capacity, $E = \sqrt{\rho c k}$ is the thermal effusivity, and the subscript, ↓ and ↑, represents the substrate and sample, respectively. If the thermal penetration depth within the insulation layer is much larger than its thickness, then the insulation layer can be assumed as a contact thermal resistance, $R_{\text{insl.}} = \delta_{\text{insl.}}/k_{\text{insl.}}$, where $\delta_{\text{insl.}}$ is the thickness of the insulation layer, and $k_{\text{insl.}}$ is the thermal conductivity of the insulation layer [19, 21].

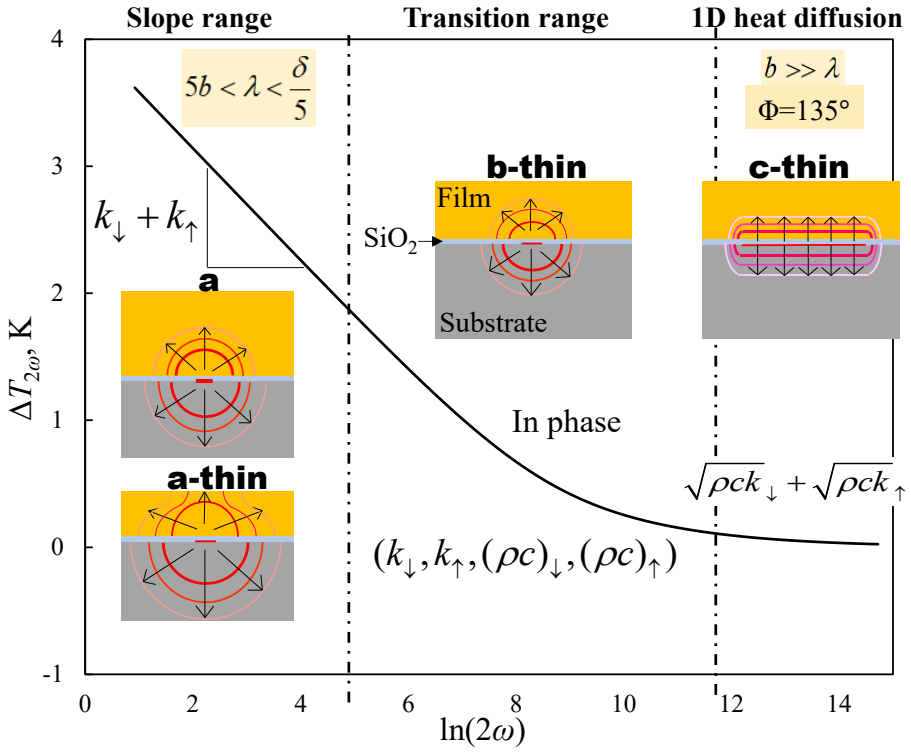

Fig. 4.1 The schematic of the division of the employing range for the bi-directional 3-omega method: (a) heat transfer model when the sample is thick and meets the rule of slope method, (a-thin) heat transfer model when the sample is thin, and the thermal penetration depth is over the thickness of the sample, (b-thin) heat transfer model when the sample is thin, and the thermal penetration depth is smaller than the thickness of the sample, and (c-thin) heat transfer model when the sample is thin, and thermal conduction becomes one-dimensional in the vertical direction of the substrate.

In the low-frequency range (Fig. 4.1(a)), where the temperature penetration depth is sufficiently larger than the sensor width and much smaller than the substrate and sample thickness ($5b < \lambda < \delta/5$) [14, 15, 17-20], Equation (4.3) is a good approximation of the temperature amplitude.

$$\Delta T_{2\omega} = -\frac{P_0}{2\pi L(k_{\downarrow} + k_{\uparrow})}\left[ln(2\omega) + \xi + i\frac{\pi}{2} \right] \tag{4.3}$$

where ξ is the real function related to the physical properties of the material, and is independent of ω [19]. In this frequency range, the sum of the thermal conductivity of the substrate and the thermal conductivity of the sample can be obtained from the slope of the temperature amplitude with respect to ln(2ω), which is independent of density and specific heat. This is called the slope method. The thermal conductivity of the sample above the heater can be obtained by subtracting the previously measured thermal conductivity of the substrate from Equation (4.3). When measuring relatively thin samples, which is the subject of this study, it is difficult to apply the slope method because the temperature penetration depth is limited by the film thickness of the sample (Fig. 4.1(a-thin)). On the other hand, in the high-frequency region where the temperature penetration depth is sufficiently smaller than the line width (λ << b, Fig. 4.1(c-thin)), thermal conduction becomes one-dimensional in the vertical direction of the substrate, and the amplitude of temperature oscillation of Equation (4.1) can be approximated by Equation (4.4), from which the thermal effusivities of substrate and sample can be determined.

$$\Delta T_{2\omega} = \frac{P_0 / 2Lb}{(\sqrt{2\omega(\rho c)_{\downarrow} k_{\downarrow}}\, e^{i\pi/4} + \dfrac{1}{\dfrac{1}{\sqrt{2\omega(\rho c)_{\uparrow} k_{\uparrow}}\, e^{i\pi/4}} + R_{insl.}})} \tag{4.4}$$

Equations (4.1) - (4.4) correspond to the temperature amplitude in the usual one-sided 3-omega method when the thermal conductivity of the sample, $k_{\uparrow}$, and the thermal resistance of the insulation layer, $R_{\mathrm{insl.}}$, are set to zero.

Figure 4.2(a) shows the sensitivities to thermal conductivity and thermal effusivity for each heater width obtained from Eq. (4.1) plotted against the heating frequency, where

the substrate is assumed to be glass, and the sample is a thermoelectric thin film. Regardless of the properties of the substrate or sample, the 3-omega method has a high sensitivity to thermal conductivity in the low-frequency range and high sensitivity to thermal effusivity in the high-frequency range. The wider the heater width, the greater the sensitivity to thermal effusivity, and the narrower the heater width, the greater the sensitivity to thermal conductivity. The frequency range where the sensitivity to thermal effusivity keeps constant is the one-dimensional heat conduction region where the temperature amplitude is expressed by Equation (4.4).

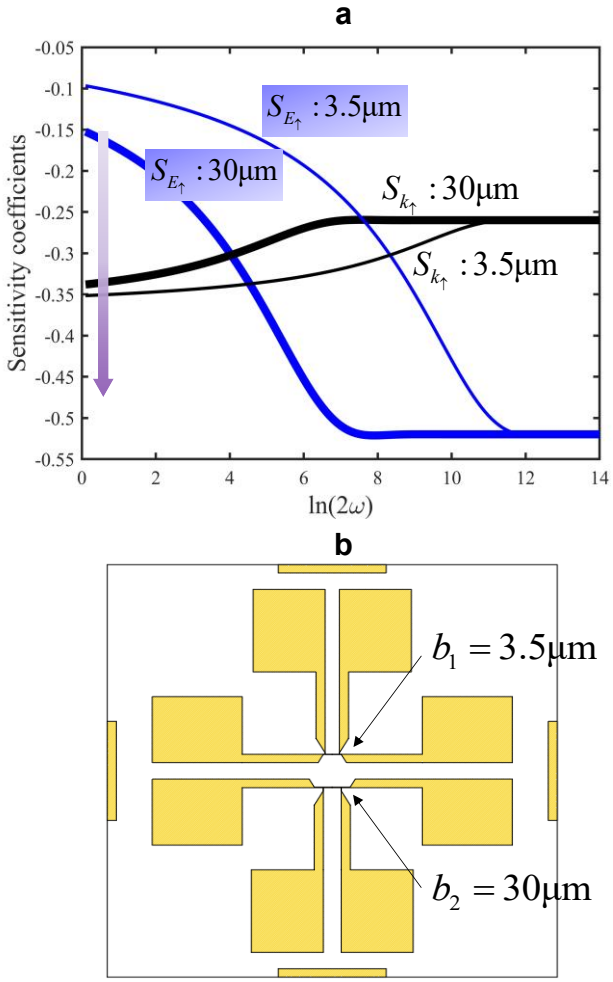

Fig. 4.2 Relative sensitivity analysis and the pattern of the dual-heater design: (a) the sensitivity of the thermal conductivity and thermal effusivity of different widths heaters,

and (b) the 4-probe pattern of the dual-heater sensor used in this paper.

This paper targets the measurement of the thermophysical properties of printed films with thicknesses from 10 microns to 100 microns order. If a relatively wide heater with a width similar to or larger than the sample thickness is used for the three-omega measurement, sufficient sensitivity for thermal conductivity measurement cannot be achieved because the temperature penetration depth is limited by the sample thickness, which prevents measurement in the low-frequency range. On the other hand, if a nano-heater with a submicron order width significantly thinner than the sample thickness is used, the thermal conductivity can be measured directly and easily using the slope method. However, there are potential problems in using the nano-heater: the heater fabrication cost is high due to the need for electron beam lithography, and the heater is easily damaged during the coating and subsequent heat-treatment process. To solve these problems, we propose a method to measure the thermal conductivity and thermal effusivity of a film with a thickness of 10 to 100 microns using two different line width heaters with different sensitivities (Fig. 4.2(b)).

In order to obtain the thermal conductivity of the sample by fitting the analytical solution (Eq. 4.1) to the measured temperature oscillation $\Delta T_{2\omega}$, it is necessary to measure three thermophysical properties in advance: the thermal conductivity and the volumetric specific heat of the substrate and the volumetric specific heat of the sample. Since the 3-omega method cannot determine the volumetric specific heat independently from the thermal conductivity, the thermal effusivity, which is a function of the volumetric specific heat and the thermal conductivity, was measured in the one-dimensional heat conduction domain instead of the volumetric specific heat in this study. The measurement procedure

is as follows (Fig. 4.3).

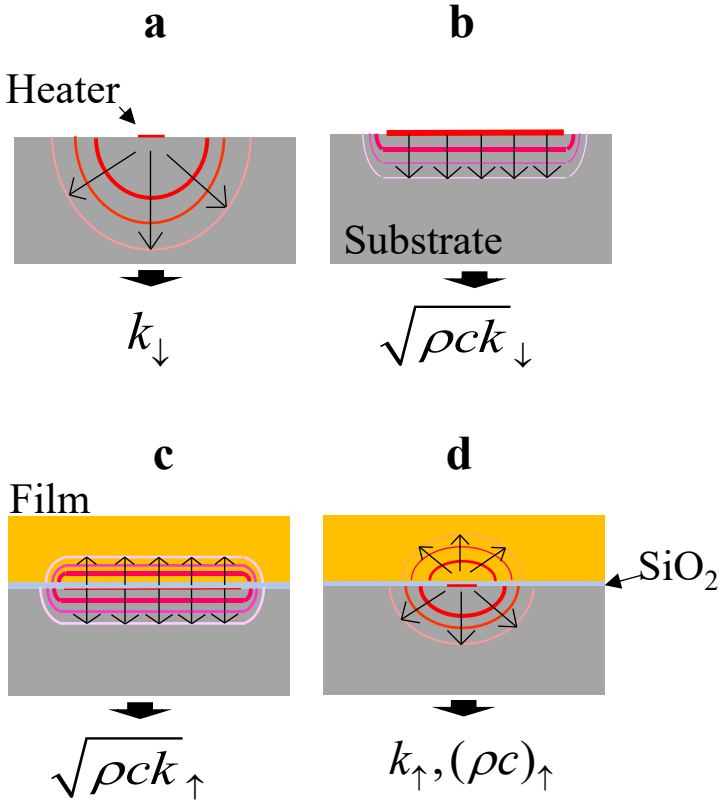

Fig. 4.3 The schematic of the experimental procedure. ((a) and (d) use the narrow heater, and (b) and (c) use the wide heater).

First, the thermophysical properties of the substrate are determined based on Eq. 4.3 and Eq. 4.4 with zero for thermal conductivity of the upper side. (a) The thermal conductivity of the substrate is determined by the slope method (Eq. 4.3). (b) The thermal effusivity of the substrate is determined using a wide heater that can easily achieve one-dimensional heat conduction at a relatively low frequency (Eq. 4.4). The sample is then placed on the heater. (c) The thermal effusivity of the sample is determined by fitting Eq. 4.4 with the thermal effusivity of the substrate measured in the previous step (b) to the heating frequency dependence of the temperature amplitude measured with the wide

heater. Finally, (d) the thermal conductivity of the sample is obtained by fitting the analytical solution (Eq. 4.1) to the temperature amplitude measured with the narrow heater, which has a higher sensitivity to thermal conductivity, with the thermal effusivity measured in the previous step (c) given as a fixed value and the thermal conductivity varied parametrically.

4.3 Experimental setup and procedure

4.3.1 Dual-heater sensor fabrication

The dual-heater sensor was fabricated on the 1.0 mm thick soda-lime glass substrate by photolithography and sputtering. Two heaters with different line widths were deposited on the same substrate: the narrow heater is ~200 nm thick, 8-9 μm wide, and 0.80 mm long, and the wide heater is ~200 nm thick, 60 μm wide, and 1.0 mm long. For the narrower heaters, it is difficult to measure line width at a spatial resolution of 0.1 micron using a typical optical microscope. Therefore, in this study, the value of the 0.1 micron digit of the heater width was determined through thermal conductivity measurement with respect to pure water showing stable thermophysical properties. The sensor width was determined by measuring the heating frequency dependence of the temperature amplitude for water and fitting the analytical solution obtained by substituting the literature values of the thermophysical properties of water and the line width as the parameter to the measured temperature oscillation. This process can be skipped if the line width can be accurately determined by AFM or SEM. Since the thermoelectric coating film as the measurement target is electrically conductive, a 250 nm SiO_2 insulating layer is sputtered on the surface of the wires. The thermal conductivity required to calculate the thermal

resistance of the SiO_2 insulating layer for fitting with the analytical solution was measured in advance using the general one-sided differential 3-omega method [8]. The thermal conductivity of the SiO_2 thin film sputtered on an alumina substrate was measured to be 1.3 W/(m·K).

4.3.2 Experimental circuit

The temperature oscillation $\Delta T_{2\omega}$ can be obtained from the amplitude of the 3ω component of the heater line signal $V_{3\omega}$.

$$\Delta T_{2\omega} = \frac{2V_{3\omega}}{I_0 R_0 \frac{1}{R_0}\frac{dR}{dT}} \tag{4.5}$$

where I_0 is the amplitude of alternative current, R_0 is the resistance of the heater line without joule heating, $\frac{dR}{R_0 dT}$ is the temperature coefficient of resistance of heater line.

Figure 4.4 shows the used electrical circuit for the 3-omega measurement. In the experiment, a heater line and a reference resistor (high-precision constant resistor) with a similar resistance to the heater line are connected in series, and an AC current of angular frequency 1ω is supplied to the circuit by a low-noise current source (155 AC/DC, Lake Shore) to sinusoidally heat the heater line at the angular frequency 2ω. The voltage drop across the heater includes a 3ω component originating from the temperature oscillation and a 1ω component three orders of magnitude larger than the 3ω component. The 1ω component contained in the heater line signal was reduced to the same level as that of the 3ω component using the self-built differential amplifiers. This allows the measurement range of the lock-in amplifier to be selected according to the magnitude of the 3ω component to realize an appropriate voltage measurement resolution of the lock-in

amplifier (MFLI 5M, Zurich Instrument). The homemade amplifiers have a cutoff frequency over 2 MHz, confirming that there is no concern about a delay or gain degradation in the measurement frequency range of this study (Fig. 4.5).

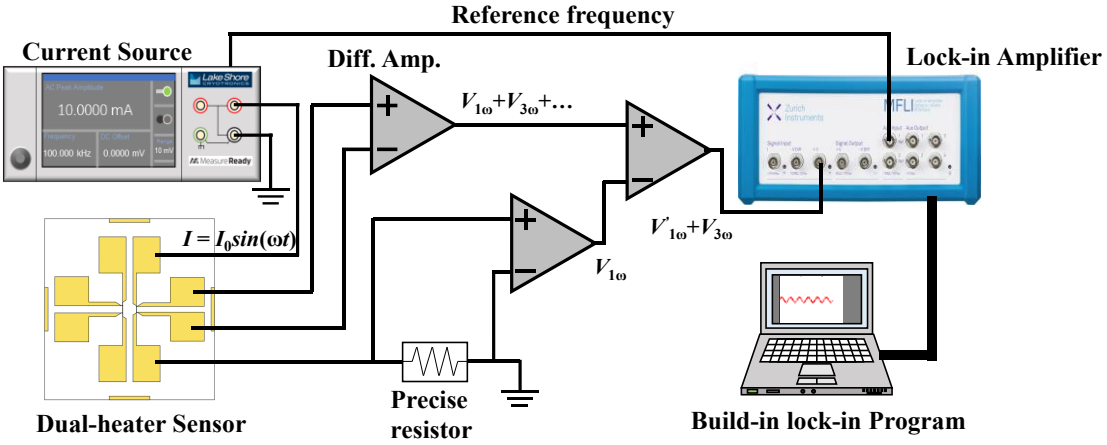

Fig. 4.4 The schematic of the experimental circuit.

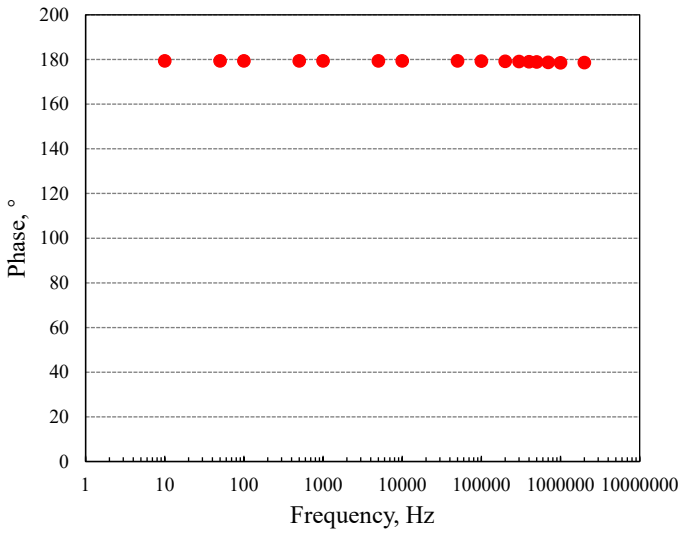

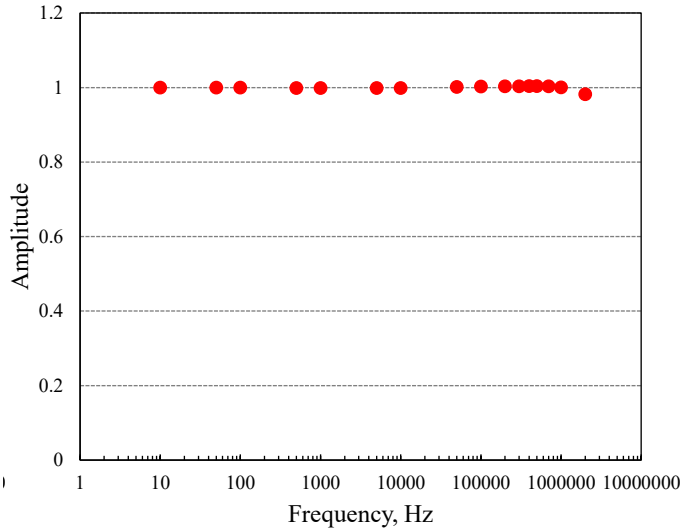

Fig. 4.5 The phase and amplitude variation during cut-off frequency determination.

4.4 Results and discussion

4.4.1 Validation

In this section, we measured the thermal conductivity and volumetric heat capacity of the glycerin and SU-8 film to verify the validity of the method. Before successfully measuring the thermal conductivity of the thermoelectric composite films, the thermal conductivity and volumetric heat capacity of the pure water with the SiO_2 insulation were measured: (a) to check the validity of the method, and (b) to ensure the size of the heaters. The thermophysical properties of pure water are known. By fitting the experimental data, we can calibrate the width of heaters, thermal conductivity $k_{\downarrow}$, and volumetric heat capacity $(\rho c)_{\downarrow}$ of the soda-lime glass substrate for the film samples measurement.

4.4.2 Measurement for glycerin droplet

First, we measured the thermophysical properties of glycerin droplets, which have

well-known thermophysical properties, to verify the proposed method. Glycerin droplets of about 2 mm in height were placed on the wall covering two thin wire heaters. After measuring the thermophysical properties of the substrate by one-sided 3-omega measurement, a wide sensor was used to measure the temperature oscillation in the one-dimensional heat conduction domain at high frequencies, and the thermal effusivity was obtained by fitting Equation 4 to the temperature oscillation. As shown in Fig. 4.6(c), it can be seen that the analytical solution fits the experimental results well. The measured thermal effusivity is 9.37×10^2 J/(K·m^2·s$^{0.5}$), which is in good agreement with the literature value 9.39×10 J/(K·m^2·s$^{0.5}$) [22]. The thermal conductivity was obtained by finding the one that can best fit the experimental results measured with the narrower heater by the analytical solution with $k_{\downarrow}$, $\sqrt{(\rho c)_{\downarrow} k_{\downarrow}}$, and $\sqrt{(\rho c)_{\uparrow} k_{\uparrow}}$ measured in advance. The frequency range was determined so that the temperature penetration depth falls within 20 microns, which is sufficiently small for measurements on samples smaller than 100 microns. The thermal conductivity obtained was 0.298 W/(m·K), in good agreement with the literature value of 0.290 W/(m·K) [22]. Since the droplet is sufficiently larger than the width of the heater line, the thermal conductivity can also be measured by the slope method for high-precision measurement (Fig. 4.6(e)). The thermal conductivity obtained by the slope method using the narrow heater, which is close to the literature value.

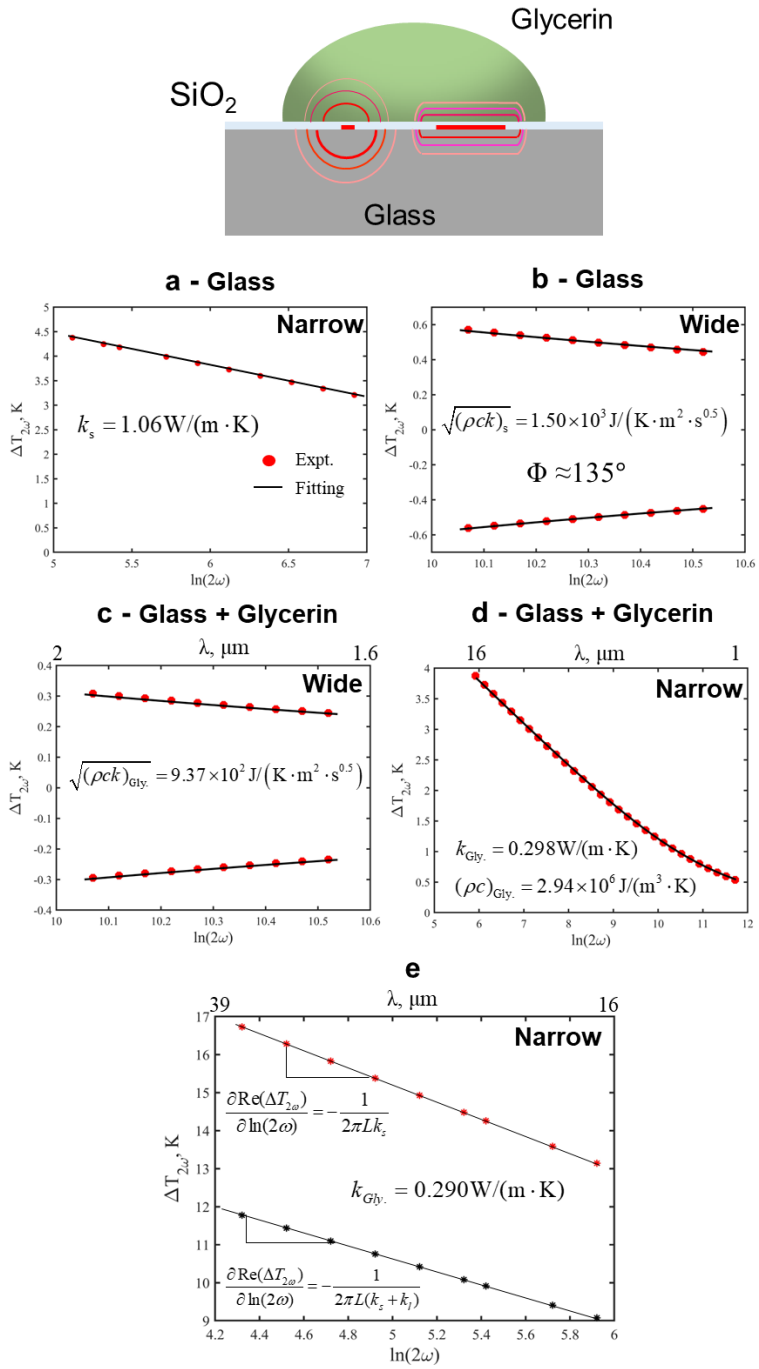

Fig. 4.6 (a - d) the thermal conductivity of the glycerin measurement procedure using the new approach of the bi-directional 3-omega method. (e) The thermal conductivity of the glycerin measurement using the traditional bi-directional 3-omega method. (The value at the top coordinate axis is the thermal penetration depth inside glycerin at the corresponding modulated angular frequency.)

4.4.3 Measurement for epoxy resin SU-8 3025

Next, to confirm the applicability of the proposed method to thin solid coatings, we measured the thermal conductivity and effusivity of a commercially available epoxy resin SU-8 3025, which is widely used as a component of MEMS because of its high mechanical, chemical, and thermal stability. The SU-8 is applied by spin-coating on a sensor substrate with a SiO2 insulation layer. The spin-coated SU-8 was cured by heat treatment and UV exposure. The thickness of the prepared SU-8 was 20 μm.

Figure 4.6 shows the measurement results for SU-8 using the same procedure as in the glycerin case described above. First, we can confirm that all experimental data are in good agreement with the fitted analytical solutions. The obtained thermal effusivity and thermal conductivity are 6.17×10^{2} J/(K·m^{2}·s$^{0.5}$) and 0.206 W/(m·K), respectively, and the thermal diffusivity obtained from them is 1.11×10^{-7} m^{2}/s. Although it is difficult to simply compare the thermophysical properties of resin materials because they depend on the processing procedures, it can be said that the results obtained by this method are reasonable.

It can be clearly seen in Fig. 4.7 (narrow heater) that the experimental results deviate from the analytical solution because the thermal penetration depth is close to or exceeds the film thickness in the region where the frequency is smaller than about 1000 Hz in the case of a narrow heater. The thermal penetration depth calculated from the measured thermal diffusivity is shown on the upper horizontal axis, indicating that the method is appropriate for thermal penetration depths shorter than about 1/2 of the film thickness.

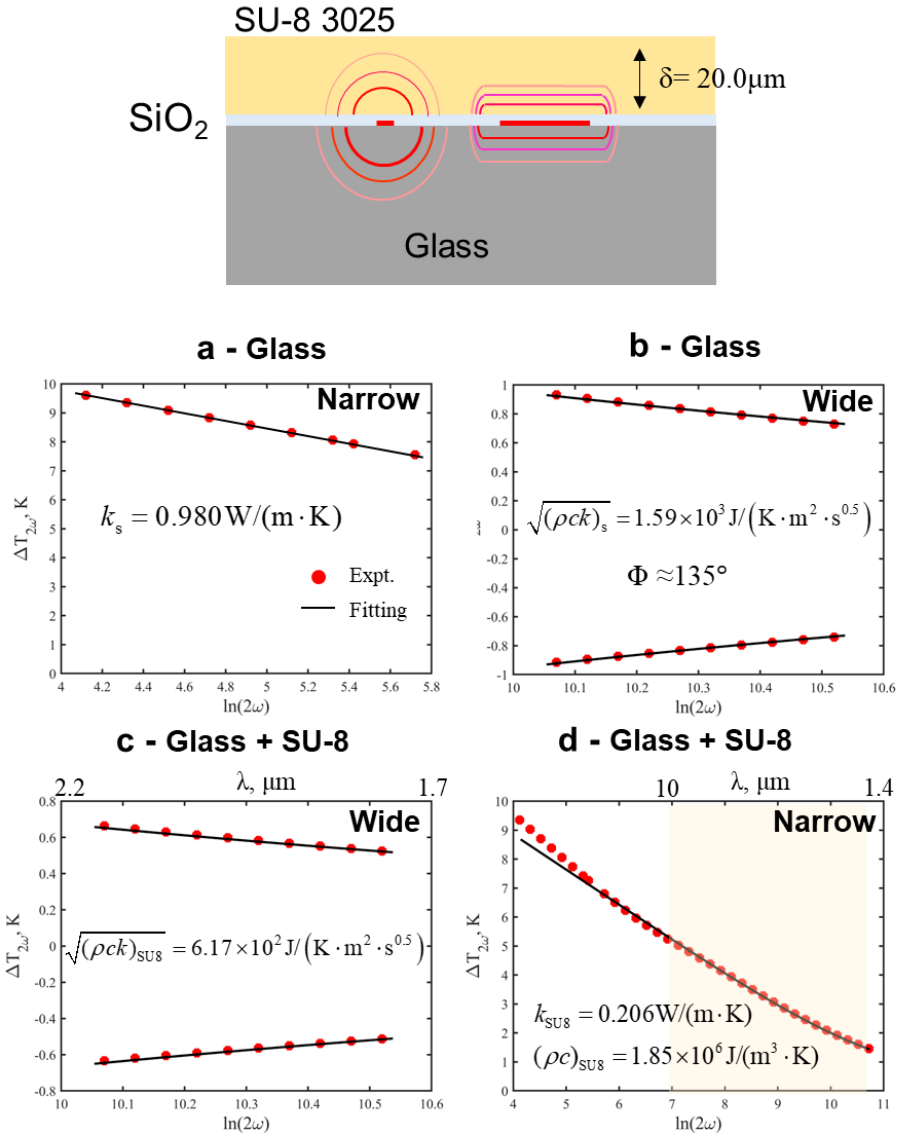

Fig. 4.6 (a - d) the thermal conductivity of the SU-8 coated film measurement procedure using the new approach of the bi-directional 3-omega method. (The value at the top coordinate axis is the thermal penetration depth inside SU-8 coated film at the corresponding modulated angular frequency.)

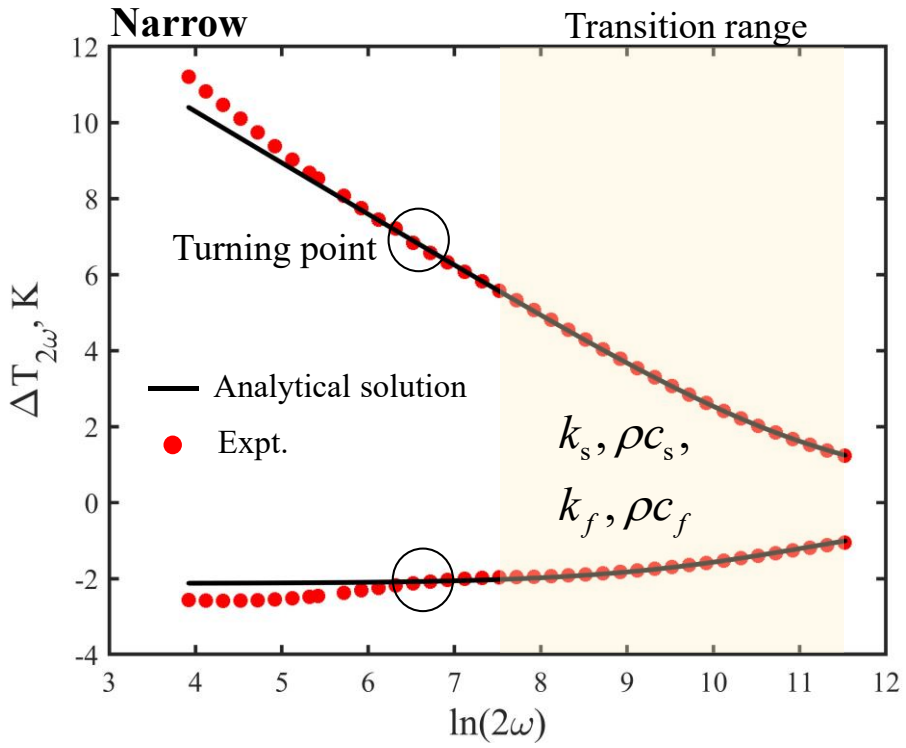

Fig. 4.7 The temperature oscillation measurement of the thin film sample with a turning point.

4.4.4 Measurement of the thermoelectric composite film: $Bi_{0.4}Sb_{1.6}Te_3$/polyimide

We measured the thermophysical properties of a composite of a Bi_2Te_3-based thermoelectric material and polyimide deposited on the surface by a printing process (Fig. 4.8(a)). Bi_2Te_3-based materials are one of the most promising thermoelectric materials due to their excellent thermoelectric properties, and polyimide as a binder is a polymer material with excellent mechanical, chemical, and thermal stability. In this study, p-type $Bi_{0.4}Sb_{1.6}Te_3$ (BST), which is an antimony-doped Bi_2Te_3, was used as a thermoelectric material. First, the ink with $Bi_{0.4}Sb_{1.6}Te_3$ particles dispersed in a precursor to polyimide is applied to a substrate using an applicator. To ensure good contact between the printed

film and the substrate, the wettability of the substrate surface is improved by plasma treatment before printing. Before measurement, it is confirmed from the backside of the substrate that there are no voids between the coated film and the substrate. The coated material was heat-treated in a furnace in a reducing environment at 400°C for 3 hours in order to imidize polyamic acid to obtain polyimide (PI) and to sinter $Bi_{0.4}Sb_{1.6}Te_3$ particles (Fig. 4.8(b)). The thermal conductivities of samples with four volume fractions, 74:26, 65:35, 55:45, and 35:65 (the former is $Bi_{0.4}Sb_{1.6}Te_3$), were measured.

Figure 4.9 shows the measured thermal conductivity and volumetric heat capacity of the $Bi_{0.4}Sb_{1.6}Te_3$/polyimide composite film utilizing the new approach with different volume fractions. The 0.1 mm thick $Bi_{0.4}Sb_{1.6}Te_3$/polyimide composite film was coated on the sensor above the dual-heater using a film applicator, as shown in Fig. 4.8. Before measurement, the sensor with the $Bi_{0.4}Sb_{1.6}Te_3$/polyimide composite film was annealed for 3 hours at 400°C in the vacuum furnace. The measured thermal conductivities are 0.742 W/(m·K) (74:26 vol%), 0.624 W/(m·K) (65:35 vol%), 0.593 W/(m·K) (55:45 vol%), and 0.424 W/(m·K) (35:65 vol%), respectively.

Here, we compared the measurement of thermal conductivities with the effective thermal conductivity of printed $Bi_{0.4}Sb_{1.6}Te_3$/polyimide composite film based on the volume fraction. During the film printing process, due to the presence of the $Bi_{0.4}Sb_{1.6}Te_3$ particle, even mixing with the liquid polyimide, there are air voids existing within the film leading to the thermal conductivity of the film decrease. As a result, when we calculated the effective thermal conductivity of the printed $Bi_{0.4}Sb_{1.6}Te_3$/polyimide composite film, the three components ($Bi_{0.4}Sb_{1.6}Te_3$, polyimide, air) had to be considered. The fraction of the $Bi_{0.4}Sb_{1.6}Te_3$ and polyimide was known, and the fraction of air voids was unknown. But from Fig. 4.10, we found the fraction of air voids should be smaller

because there is no visible void appearing. So, we assumed the fraction of air voids was below 30%, and got the effective thermal conductivities under different volume fractions of $Bi_{0.4}Sb_{1.6}Te_3$ and polyimide using the calculating model presented by G. N. Dulfnev [25, 26] for three components (Eq. 4.6) as shown in Fig. 4.11. The measurement results are within the predicted range from 0 vol% to 30 vol% of air voids.

$$k_{eff} = k_{\mathrm{BST}} \left\{ \begin{array}{l} \dfrac{V_{\mathrm{PI}}}{1-V_{\mathrm{BST}}} \left[1 - \dfrac{1-V_{\mathrm{BST}}}{1/(1-k_{\mathrm{PI}}/k_{\mathrm{BST}}) - V_{\mathrm{BST}}/3} \right] \\ + \dfrac{V_{\mathrm{air}}}{1-V_{\mathrm{BST}}} \left[1 - \dfrac{1-V_{\mathrm{BST}}}{1/(1-k_{\mathrm{air}}/k_{\mathrm{BST}}) - V_{\mathrm{BST}}/3} \right] \end{array} \right\} \tag{4.6}$$

where V is the volume fraction of component.

We also calculated the limitation of the effective thermal conductivity for the printed $Bi_{0.4}Sb_{1.6}Te_3$/polyimide composite film under different volume fractions using the limiting model. Two limiting cases are provided by the series distribution (minimum), and the parallel distribution (maximum) [27]. The prediction range covered the calculation for the thermal conductivity of the bulk $Bi_{0.4}Sb_{1.6}Te_3$ material [28]. All experimental results were within the range predicted for the thermal conductivity of composite materials, as shown in Fig. 4.11. The problem is that there is no precise reference thermal conductivity of the bulk $Bi_{0.4}Sb_{1.6}Te_3$ material. Now, for the effective thermal conductivity calculation, the highest value we selected and the measurement results are close to the series model. But, if we selected other smaller reference values of the thermal conductivity of the bulk $Bi_{0.4}Sb_{1.6}Te_3$ material [29-31], our measurement results are still within the predicted range.

To summarize the above, our measurements are relatively within the calculation range of the individual effective thermal conductivity prediction models. Moreover, it is important that our measurement results best fit the analytical solution of the bi-directional

3-omega method, which justifies our measurement results.

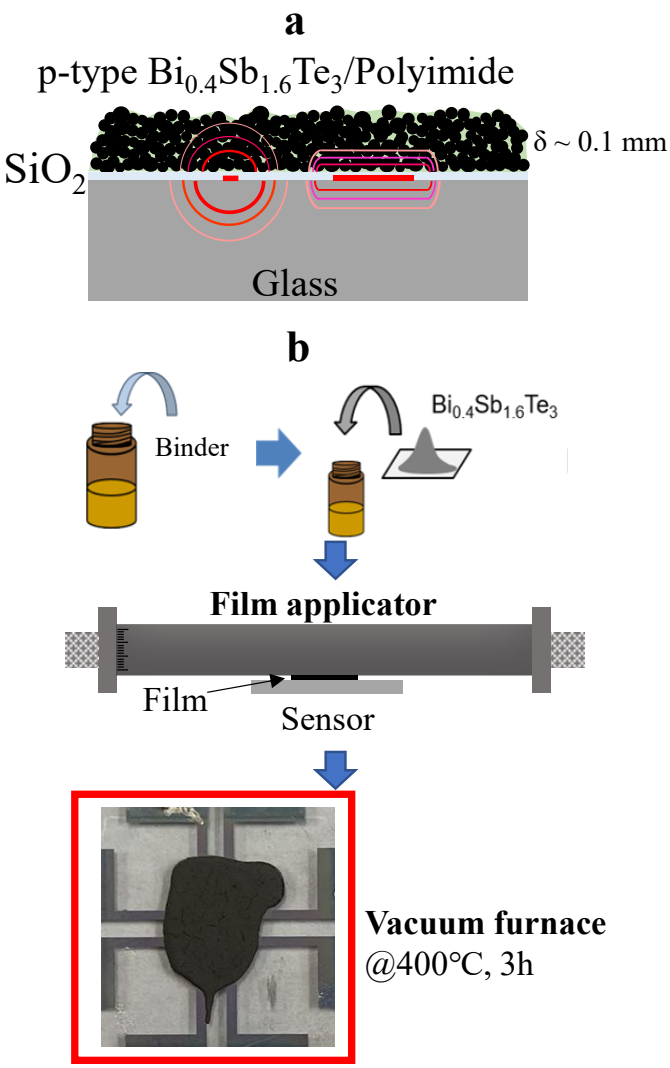

Fig. 4.8 The printed 0.1 mm thick $Bi_{0.4}Sb_{1.6}Te_3$/polyimide composite film on the sensor.

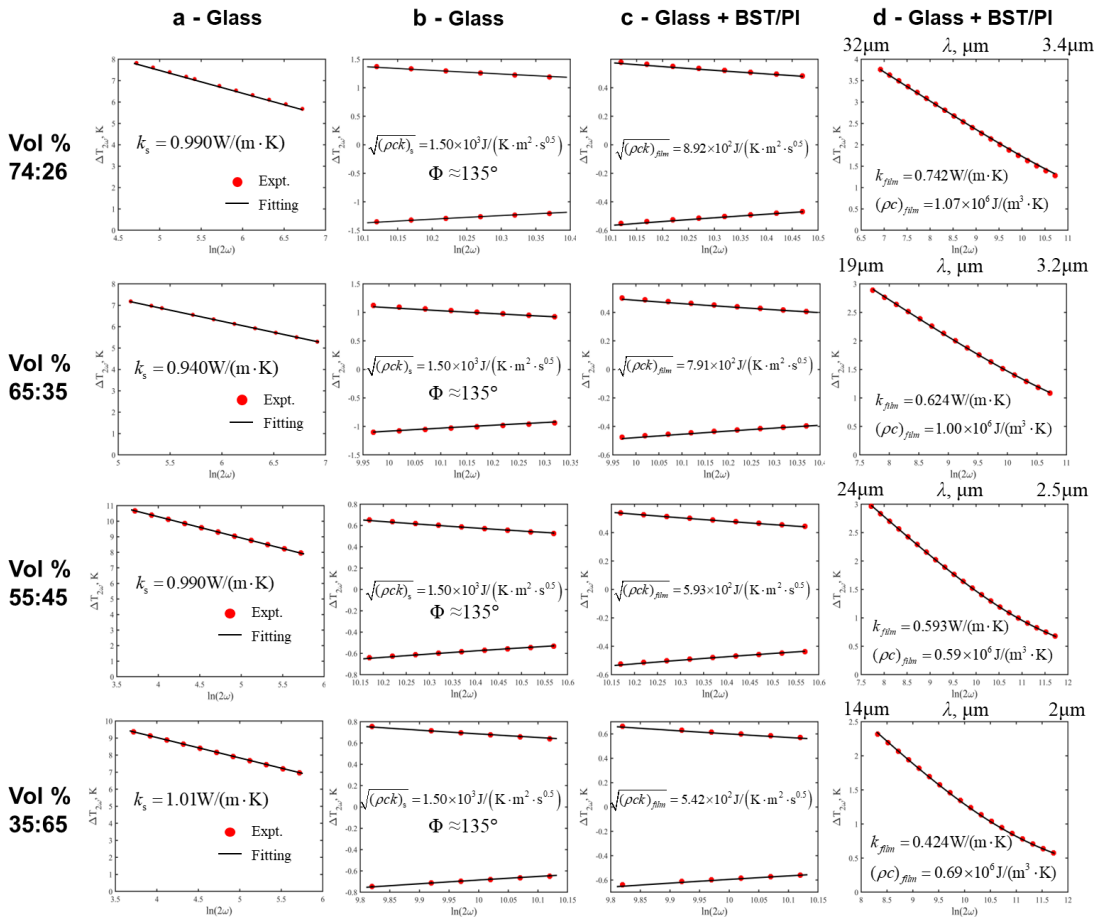

Fig. 4.9 The measured thermal conductivity of the printed $Bi_{0.4}Sb_{1.6}Te_3$/polyimide composite film with different volume fractions.

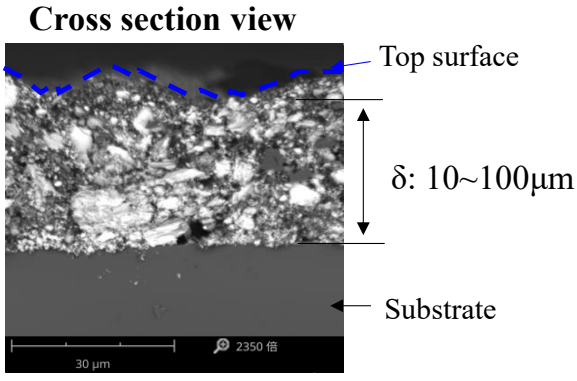

Fig. 4.10 The cross section view of printed $Bi_{0.4}Sb_{1.6}Te_3$/polyimide composite film using SEM (74:26 vol%).

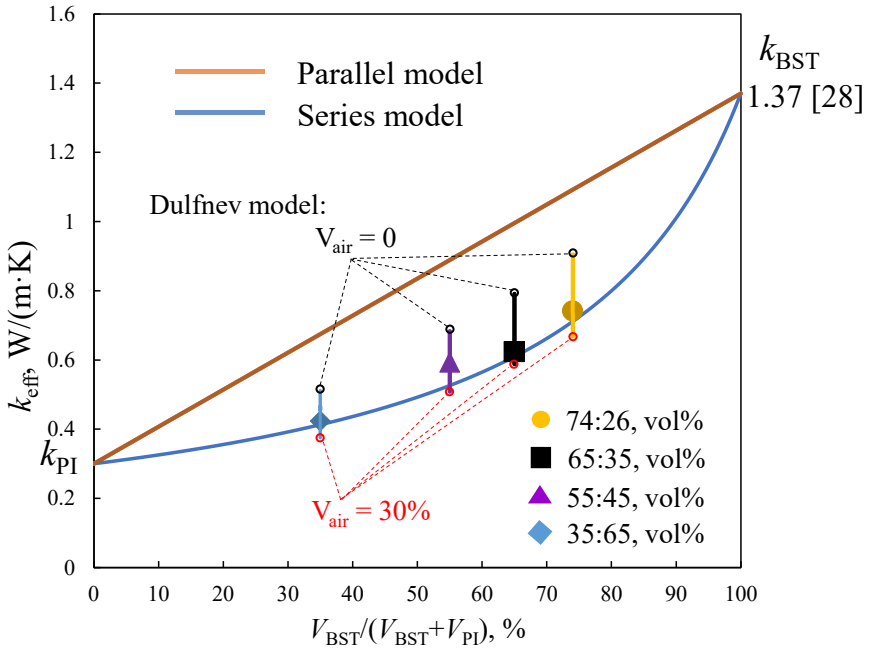

Fig. 4.11 The effective thermal conductivity of $Bi_{0.4}Sb_{1.6}Te_3$/polyimide composite film. (The thermal conductivity of the used polyimide in this study was measured using the differential 3-omega method.)

4.5 Conclusions

Table. 4.1 shows all the experiment results in this paper, and all the measurement results agree well with the reference value. For glycerin and SU-8, we also checked the thermal conductivity of the measurement samples using the traditional methods, and the results are close to the measurement using the new method.

Table. 4.1 Experimental temperature and thermal conductivity of the samples.

Sample	R.T.*, °	*k*, W/(m·K)	
		Expt.	Lit.
Glycerin	25	0.298	0.29 [22]
Glycerin	25	0.30	
SU-8	25	0.206	0.2~0.3 [23, 24]
$Bi_{0.4}Sb_{1.6}Te_3$/Polyimide	25	0.742	74:26, vol%
		0.624	65:35, vol%
		0.593	55:45, vol%
		0.424	35:65, vol%

R. T.*: the room temperature during the experiment.

In this paper, the thermal conductivity of the liquid and solid thin film samples, 10.0 ~ 100.0 μm thick, were measured by the novel strategy of the bi-directional 3-omega method. The conclusions of this study are summarized as follows,

1. We developed the dual-heater 3-omega method for measuring the thermal conductivity and thermal effusivity of the printed films.
2. We validated this method through the measurement of glycerin and SU-8 polymer resin.
3. We succeeded in obtaining reasonable thermal conductivity for thermoelectric composite printed films with a rough surface.
4. This method, which enables high-throughput measurement, should accelerate the development of thermoelectric printed films and other coatings for thermal applications.
5. In this paper, the thermal conductivity of the substrate is larger than the measurement samples, which increases the difficulty of measurement because the heat flow towards the upper side sample is only a small part of the total heat flow, and the temperature oscillation inside the sample is small.

References

[1] S. Khan, L. Lorenzelli, R.S. Dahiya, Technologies for printing sensors and electronics over large flexible substrates: A review, IEEE Sens. J. 15 (2015) 3164–3185.

[2] S.T. Han, H. Peng, Q. Sun, S. Venkatesh, K.S. Chung, S.C. Lau, Y. Zhou, V.A.L. Roy, An Overview of the Development of Flexible Sensors, Adv. Mater. 29 (2017) 1–22.

[3] M. Burton, G. Howells, J. Atoyo, M. Carnie, Printed Thermoelectrics, Adv. Mater. 34 (2022).

[4] K. Kato, K. Kuriyama, T. Yabuki, K. Miyazaki, Organic-Inorganic Thermoelectric Material for a Printed Generator, J. Phys. Conf. Ser. 1052 (2018).

[5] K. Kato, H. Hagino, K. Miyazaki, Fabrication of bismuth telluride thermoelectric films containing conductive polymers using a printing method, J. Electron. Mater. 42 (2013) 1313–1318.

[6] C. Ou, A.L. Sangle, A. Datta, Q. Jing, T. Busolo, T. Chalklen, V. Narayan, S. Kar-Narayan, Fully Printed Organic-Inorganic Nanocomposites for Flexible Thermoelectric Applications, ACS Appl. Mater. Interfaces. 10 (2018) 19580–19587.

[7] C. Liu, F. Jiang, M. Huang, B. Lu, R. Yue, J. Xu, Free-standing PEDOT-PSS/Ca3Co4O9 composite films as novel thermoelectric materials, J. Electron. Mater. 40 (2011) 948–952.

[8] S. Roy-Panzer, T. Kodama, S. Lingamneni, M.A. Panzer, M. Asheghi, K.E. Goodson, Thermal characterization and analysis of microliter liquid volumes using

the three-omega method, Rev. Sci. Instrum. 86 (2015) 1–11.

[9] C. Dames, Measuring the Thermal Conductivity of Thin Films: 3 Omega and Related Electrothermal Methods, Annu. Rev. Heat Transf. 16 (2013) 7–49.

[10] T. Borca-Tasciuc, A.R. Kumar, G. Chen, Data reduction in 3ω method for thin-film thermal conductivity determination, Rev. Sci. Instrum. 72 (2001) 2139–2147.

[11] D.G. Cahill, Analysis of heat flow in layered structures for time-domain thermoreflectance, Rev. Sci. Instrum. 75 (2004) 5119–5122.

[12] Sun J, Lv G, Cahill D G. Frequency-domain probe beam deflection method for measurement of thermal conductivity of materials on micron length scale. arXiv preprint arXiv:2209.08239, 2022.

[13] J. Zhu, D. Tang, W. Wang, J. Liu, K.W. Holub, R. Yang, Ultrafast thermoreflectance techniques for measuring thermal conductivity and interface thermal conductance of thin films, J. Appl. Phys. 108 (2010).

[14] I.K. Moon, Y.H. Jeong, S.I. Kwun, The 3ω technique for measuring dynamic specific heat and thermal conductivity of a liquid or solid, Rev. Sci. Instrum. 67 (1996) 29–35.

[15] B.K. Park, J. Park, D. Kim, Note: Three-omega method to measure thermal properties of subnanoliter liquid samples, Rev. Sci. Instrum. 81 (2010) 1–4.

[16] B.K. Park, N. Yi, J. Park, D. Kim, Note: Development of a microfabricated sensor to measure thermal conductivity of picoliter scale liquid samples, Rev. Sci. Instrum. 83 (2012) 2012–2015.

[17] B. Kyoo Park, N. Yi, J. Park, D. Kim, Thermal conductivity of single biological cells and relation with cell viability, Appl. Phys. Lett. 102 (2013) 1–6.

[18] B.K. Park, N. Yi, J. Park, Y. Kim, D. Kim, Development of a thermal sensor to

probe cell viability and concentration in cell suspensions, AIP Adv. 4 (2014).

[19] S.D. Lubner, J. Choi, G. Wehmeyer, B. Waag, V. Mishra, H. Natesan, J.C. Bischof, C. Dames, Reusable bi-directional 3 ω sensor to measure thermal conductivity of 100-μ m thick biological tissues, Rev. Sci. Instrum. 86 (2015) 1–13.

[20] B.K. Park, Y. Woo, D. Jeong, J. Park, T.Y. Choi, D.P. Simmons, J. Ha, D. Kim, Thermal conductivity of biological cells at cellular level and correlation with disease state, J. Appl. Phys. 119 (2016).

[21] Y.S. Ju, K.E. Goodson, Process-dependent thermal transport properties of silicon-dioxide films deposited using low-pressure chemical vapor deposition, J. Appl. Phys. 85 (1999) 7130–7134.

[22] Bergman, Theodore L., et al. Fundamentals of heat and mass transfer. John Wiley & Sons, 2011.

[23] SU-8-3000-Data-Sheet.

[24] S. Erfantalab, G. Parish, A. Keating, Determination of thermal conductivity, thermal diffusivity and specific heat capacity of porous silicon thin films using the 3ω method, Int. J. Heat Mass Transf. 184 (2022) 122346.

[25] Dul'Nev G N, Zarichnyak Y P. Thermal conductivity of multicomponent mixtures. Journal of engineering physics, 1967, 12(4): 215-219.

[26] Maxwell J C. A treatise on electricity and magnetism. Oxford: Clarendon Press, 1873.

[27] Meredith R E, Tobias C W. Resistance to potential flow through a cubical array of spheres. Journal of applied Physics, 1960, 31(7): 1270-1273.

[28] Li Y Y, Qin X Y, Li D, et al., Enhanced thermoelectric performance of $Cu_2Se/Bi_{0.4}Sb_{1.6}Te_3$ nanocomposites at elevated temperatures, Appl. Phys. Lett.,

108 (2016) 062104.

[29] Lee K H, Hwang S, Ryu B, et al., Enhancement of the thermoelectric performance of $Bi_{0.4}Sb_{1.6}Te_3$ alloys by In and Ga doping, J. Electron. Mater., 42 (2013) 1617-1621.

[30] Wang Y S, Huang L L, Li D, et al., Enhanced thermoelectric performance of $Bi_{0.4}Sb_{1.6}Te_3$ based composites with $CuInTe_2$ inclusions, J. Alloys Compd., 758 (2018) 72-77.

[31] Lemine A S, El-Makaty F M, Al-Ghanim H A, et al., Experimental and modeling analysis of p-type $Bi_{0.4}Sb_{1.6}Te_3$ and graphene nanocomposites, J. Mater. Res. Technol., 16 (2022) 1702-1712.

5. Conclusions and outlook

5.1 Conclusions

In this thesis, the thermophysical properties of the coatings, which are difficult to form the thin and smooth film, were measured using the new methods based on the bi-directional 3-omega method.

Before experiments, first, we developed the measurement system for the 3-omega measurement of thermophysical properties, including home-built high-speed differential amplifiers with a cutoff frequency of over 1 MHz, AC current source, and lock-in amplifier. The measurement system is with a high measurement resolution, large cut-off frequency, and ultralow temperature fluctuation.

Using this measurement system, the thermal boundary resistance due to a thin air layer formed on a superhydrophobic surface underwater was measured, and the effective thickness of the air layer was calculated from the measured value. The obtained thermal boundary resistance was 7.5×10^{-6} [$(K\cdot m^2)/W$], and its equivalent air layer thickness was 0.2 μm and was consistent with the surface topology observed using an atomic force microscope. The decrease in air layer thickness due to degassing of the water was also successfully observed. The measurement method used in this study also can be employed to measure the thermal conductivity of a coating sandwiched between a thin film heater deposited on a substrate and a liquid with known thermal properties.

Printing technology enables the fabrication of large-area flexible sensors and electronic

circuits at low cost and low environmental impact, so in the second study, we developed the dual-heater bi-directional 3-omega method, which can measure thermophysical properties of printed films by using two different line width heaters with different sensitivities to thermal conductivity and volumetric specific heat. First, the thermal conductivity and thermal effusivity of glycerin droplet and SU-8 resin film were measured, and the results were in good agreement with the literature values, demonstrating the validity of the developed method and measurement system. Finally, the thermal conductivity of printed composite thermoelectric films composed of Bi_2Te_3-based thermoelectric material particles and polyimide was measured. This method is expected to be useful for high-throughput measurement of thermophysical properties of various printed materials, not only thermoelectric printed films.

5.2 Outlook

Two methods developed in this study should facilitate the measurement of the thermal conductivity of printed materials and accelerate the material development.

Acknowledgments

First and foremost, I would like to express my sincere gratitude to my supervisor, Professor Tomohide Yabuki, for the continuous support of my Ph.D. study and research and for his patience, motivation, enthusiasm, and immense knowledge. His guidance helped me in all the time of research and completing this thesis. I could not imagine having a better advisor and mentor for my Ph.D. study. I also would like to thank Professor Koji Miyazaki, Professor Asuka Miura, and Professor Kosuke Watanabe for their help and kind encouragement about my research.

Additionally, I would like to thank the rest of my thesis committee: Professor Gyoko Nagayama, and Professor Masato Yamamura, for their insightful comments and encouragement, as well as for the questions which motivated me to broaden my research from multiple perspectives.

Thanks to Professor Feng Guo of the Qingdao University of Technology, China, for his constant support and encouragement.

I want to thank the colleagues of the Micro/Nano-Thermal Engineering Laboratory group. Thanks to Mr. Tomotaka Ueki and Mr. Takanori Tanaka for their help in living in Japan. Thanks to Mr. Kenta Hatanaka, Mr. Shota Minami, Mr. Yuta Yamazaki, Mr. Ryoma Nishio, and Mr. Takuya Matsunaga for their help in my experiments. Thanks to Mr. Shuhei Tominaga, Mr. Ren Umeno, Mr. Kyohei Asano, Mr. Kaito Fukuda, and Mr. Yamato Nishio for their continuous cooperation.

Many thanks go to the Kyushu Institute of Technology and the Ministry of Education, Culture, Sports, Science and Technology, Japan for providing the Monbusho Scholarship

during October 2018–March 2023.

Last but not least, wholeheartedly, I would like to express my thanks to my family, especially my wife, Yankun Yu, who accompanied me on this unforgettable trip to study abroad. Without their love and support, it would have been impossible to finish my Ph.D. study.

JIAO Yihang

Kyushu Institute of Technology

December 2022

Appendix

Journals

1. Jiao Yihang, Miyazaki Koji, Yabuki Tomohide. Measurement of thermal boundary resistance between water and superhydrophobic surfaces by the bi-directional differential 3ω method. International Communications in Heat and Mass Transfer, 2021, 126: 105404.

Proceedings

1. Jiao Yihang, Miyazaki Koji, Yabuki Tomohide. Thickness measurement of an air layer on a nanostructured superhydrophobic surface by the 3-omega method, Mini-Workshop on Thermal and Charge Transport across Flexible Nano-Interfaces, 2020.12.01.
2. Jiao Yihang, Miyazaki Koji, Yabuki Tomohide. Measurement of thermal boundary resistance on superhydrophobic surfaces underwater by the bi-directional differential 3-omega method, 2nd Asian Conference on Thermal Science, 2021.10.06.
3. Yihang Jiao, Yamato Nishio, Koji Miyazaki and Tomohide Yabuki. MEASUREMENT OF BOILING NUCLEATION TEMPERATURE ON SMOOTH MICRO-HEATER, The 32nd International Symposium on Transport Phenomena, 2022.3.20.
4. Jiao Yihang, Miyazaki Koji, Yabuki Tomohide. Thermal conductivity measurement

of coated films by the bi-directional 3-omega method, JST 未来社会森 PJ 第 13 回コロキウム, 2022.6.29.

5. Jiao Yihang, Miyazaki Koji, Yabuki Tomohide. Thermal conductivity measurement of thermoelectric composite films by the bi-directional 3-omega method, JSPS 研究拠点形成事業国内ワークショップ, 2022.7.25.